Adsorption and adhesion energies of metal films and nanoparticles studied by adsorption calorimetry: understanding catalytic systems

Trevor E. James

A dissertation
submitted in partial fulfillment of the
requirements for the degree of

Doctor of Philosophy

University of Washington
2016

Reading Committee:
Charles T. Campbell, Chair
Xiaosong Li
Bo Zhang

Program Authorized to Offer Degree:
Chemistry

Abstract

Adsorption and adhesion of thin metal films studied by adsorption calorimetry: toward understanding chemical reactivity at stability of catalytic systems

Trevor E. James

Chair of Supervisory Committee:

Professor Charles T. Campbell

Chemistry

Metal nanoparticles dispersed across solid surfaces form the basis of many important technologies such as heterogeneous catalysts, electrocatalysts, chemical sensors, microelectronics, and fuel cells. Understanding energetics of chemical bonding between the metal and oxide in these systems is important for the development of more efficient devices. First, in Chapter 2, this dissertations discusses a new, ultrahigh vacuum single crystal adsorption calorimeter which is used to directly measure metal adsorption and adhesion energies to model catalytic surfaces from 77-350 K. Some of the key instrumental improvements over previous designs include the capability of real-time metal atom flux monitoring and a decreased thermal radiation contribution to the heat signal. Next, in chapter 3, an improved data analysis method to determine average particle size and number density from low energy ion scattering spectroscopy (LEIS) measurements of nanoparticles that grow with the shape of hemispherical caps is discussed and validated. A correction is applied for the case when nanoparticles cause substrate shadowing due to source ion incident and detection angles being non-normal to the surface. The model was demonstrated for Cu growth on slightly reduced $CeO_2(111)$ where it improved the fit ~3-fold.

In Chapters 4 and 5, the adsorption energy and growth morphology of vapor deposited copper atoms onto slightly reduced $CeO_2(111)$ was measured at 100 and 300 K. Copper was determined to grow as three-dimensional particles with preferential adsorption to stoichiometric ceria sites, opposite of what has been observed for other metals such as Ag, Au and Pt on ceria. An important result was the measurement of copper atom chemical potentials starting from single copper atoms up to large nanoparticles which provides unique insight into the increased reactivity of the small aggregates and their propensity to sinter. In Chapter 6, gold adsorption energies onto slightly reduced ceria was also measured. Like copper, gold grows as hemispherical caps on ceria, but with a smaller number density for a given temperature and extent of ceria reduction. Gold also adsorbs more strongly to reduced ceria sites than to stoichiometric sites. The adhesion energy between copper, silver, and gold nanoparticles and slightly reduced ceria was compared to previous adhesion energy trends discovered by our group. Adhesion energy of metals onto well-defined oxides adhere more strongly to ceria than MgO, and scales with the adsorbed metal's heat of sublimation minus the heat of formation of the its most stable oxide, providing a method to predict adhesion energies of metals to oxides. Lastly, in Chapter 7, the adsorption and adhesion energy of 2D copper overlayers on Pt(111) was measured by calorimetry. The adsorption energy of copper atoms in each layer was used to explain the thermodynamic driving force of copper to form the quasi-pseudomorphic layer-by-layer structure.

These studies provide new insights into interfacial chemical bonding and provide important benchmarks to test new density functional theory calculations. The results will aid in the rational design of more efficient catalysts. Future aims and conclusions of this work are presented in Chapter 8.

Table of Contents

List of Tables

List of Figures

Acknowledgements

Funding for this work was provided by the Department of Energy, Office of Basic Energy Sciences, Chemical Sciences Division Grant No. DE-FG02-96ER14630 for support of this work. Funding for the work in Chapter 4 was also provided by Hitachi Ltd., for support of this work.

Most importantly, I would like to thank Professor Charles T. Campbell for tireless support and guidance throughout my time at the UW whose effort made all these projects possible. All of the work done on “CAL 3” would not have been possible without the help of our accomplished team Dr. Jason Sellers, Gabe Feeley, and most importantly Stephanie Hemmingson. I would also like to thank the rest of the Campbell group and visiting scientist who helped make these projects possible; Dr. Jason Farmer, Dr. Eric Karp, Dr. Trent Silbaugh, Dr. James Sharp, James Lownsbury, Dr. Chris Wolcott, Spencer Carey, Dr. Daniel Mazur, Dr. Tsuyoshi Ito, and all others who have worked here. The University of Washington electronic and machine shops who helped keep the instrumentation running; Lon Buck, Roy Ulund, Bill Beaty, Brian Holm, John Heutnik, and Ed McArthur. The Gonzaga University staff who inspired me to pursue graduate level chemistry especially Dr. Eric Ross, Dr. David Cleary, and Dr. Joanne Smieja. I would lastly like to thank my friends and family who have offered a tremendous support group through my journey who are far too numerous to name.

Chapter 1

Introduction

Many advanced technologies are comprised of late transition metals anchored to oxide supports, including heterogeneous catalysts, electrocatalysts, photocatalysts, and fuel cells. These technologies play an important role in the production of fuels and chemicals, the generation of clean energy from alternative fuel sources (i.e. solar) and cleanup of environmentally dangerous chemicals. For example, heterogeneous catalysts are used in over 90% of the production of bulk chemicals, yet most industrial catalysts of this type are designed using guess and check methods.[4] The production of bulk chemicals, which often uses petroleum and natural gas as feedstocks, is the most energy intensive division of the industrial sector, consuming 5.6 quadrillion Btu in 2013 and is forecast to grow 2.3% per year over the next ten years. Bulk chemicals are also responsible for the release of 247 million metric tons of CO_2 a year and is expected to grow 0.6% a year over the next ten years.[5] Therefore, there is great need to develop new catalysts to combat rising energy costs and reduce pollution. New catalysts need to have higher selectivity for target chemical reactions in order to reduce chemical waste, have higher efficiencies (i.e. higher turnover frequency and operated at lower temperatures) to reduce the energy input into these processes, and longer lifetimes to decrease the cost and energy input into catalyst regeneration. In order to develop more efficient industrial catalysts, a fundamental understanding of oxide supported metals is required. One such approach for catalyst development is to study the physical and chemical properties of model catalytic systems, which has been done successfully in the past.[6-9] Model catalyst studies, which are often performed in ultrahigh vacuum (UHV), allow the structure of the support, the size and number density of nanoparticles, and cleanliness to be precisely controlled, simplifying the complexity of real catalysts that often consist of a variety of crystallographic faces and are operated in complex environments.

The nature and strength of interfacial chemical bonding between metals and their oxide support has been shown to influence the chemical potential of metal atoms in supported metal nanoparticles which is related to reactivity and selectivity, and the metal's adhesion energy to an oxide which is related to the long term stability of catalysts,[10,11] and it is likely these energetics also play an important role in a variety of catalytic properties. Despite this, the bond energies of only a few metal/oxide systems is known to date.[12-14] This is partially due to the difficulty measuring these energies. Indirect measurements of metal adsorption energies using temperature programmed desorption (TPD), which have been used elegantly to measure adsorption energies of metals to single crystal metal supports,[15] cannot be used for metal adsorption energies onto oxides because metals sinter during TPD temperature ramps, making the exact surface structure unknown. Therefore, single crystal adsorption calorimetry (SCAC) was introduced by the Sir David King's group at Cambridge University to directly measure heats of adsorption of gas molecules like CO, O_2 and ethyne.[16] Its sensitivity and temperature range was greatly improved by Campbell's lab by changing the heat detection method.[17,18] Campbell's lab also modified it to directly measure heats of adsorption of metal atoms, and applied it to measure adsorption energies of metal atoms and adhesion energies of metal films to single crystal supports.[17] In SCAC, metal atoms are vapor deposited onto the front face of a single crystalline support, often in the form of a single crystal oxide thin film grown on a thin metal single crystal, by a pulsed atomic beam. The resulting transient exothermic heat of adsorption is measured by a pyroelectric ribbon that is pressed into contact with the back of the sample. The calibrated heat response of the detector, plus knowledge of the number of metal atoms in each pulse, allow the molar heat of adsorption to be directly measured as a detailed function of metal coverage or average film thickness.[18] In Chapter 2, an improved SCAC apparatus for metal atom adsorption studies is described along with the experimental details required for measuring adsorption and adhesion energies of metals onto oxides. The new calorimeter improves on previous models and is capable of making higher precision heat of adsorption measurements for metals with high enthalpies of sublimation, such as copper, gold, platinum, palladium, etc. This is done by utilizing an electron beam evaporator, which is capable of making a steady flux of metal atoms with lower thermal radiation of the metal atom source contributing to the overall heat signal.

When studying model catalysts, metals are often vapor deposited onto a single crystal surface and the knowledge of the resulting film is important to understand the catalytic properties. One possible mechanism for thin film growth is the Volmer-Weber mode, where first nucleation of the metal occurs followed by growth as 3D nanoparticles.[6,7,9,19,20] The average size and number density of supported metal nanoparticles is important for determining the adhesion energy of the metals to oxides studied calorimetrically and for knowing the chemical potential of metal atoms in supported nanoparticles[10] which have a profound effect on activity, selectivity, and long term stability of these particles as discussed previously.[11] Chapter 3, introduces a new mathematical growth model used to determine the average size and number density of nanoparticles on a surface based on low energy ion scattering spectroscopy (LEIS) data when it is collected from incident and detection angles are non-normal to the surface. This model is an extension of a previous hemispherical cap model used to describe the change in LEIS signal as a function of total metal deposited. However, the original model was limited to 45 degree incident angle and normal detection angle.[21] The model in Chapter 3 maintains the assumptions that the particles grow with a fixed number density whose shape is a hemispherical caps and an average radius that grows with metal coverage. The methods developed in Chapters 2 and 3 are essential for the energetic measurements make through the remainder of this dissertation.

Cerium oxide, or ceria for short, is one of the most promising support materials for heterogeneous catalysts and has been used successfully in a wide variety of catalytic reactions.[22] As such, catalysts involving ceria as a support have received a lot of attention in the last decade.[23-25] The high catalytic efficiency of ceria based materials is partially due to its high oxygen storage capacity which is due to the low thermodynamic barrier toward the addition and removal of oxygen from the ceria lattice.[26] Copper/ceria catalysts have been used for a variety of reactions including CO oxidation,[27,28] the water gas shift reaction,[29,30] and methanol synthesis.[31,32] It was determined that the high catalytic activity for methanol surface came from copper/ceria interfacial sites which go through a different reaction pathway, which has lower energy barriers, than industrial Cu/ZnO catalysts. It was also determined that catalytic activity was only observed when Cu was neutral.[32] Interestingly, the charge state of Cu nanoparticles can be tuned by adjusting the oxidation state of ceria.[2] In Chapter 4, the adsorption and adhesion energies of copper onto slightly reduced $CeO_2(111)$ are measured by SCAC at 300 K. The resulting morphology of Cu nanoparticles and the oxidation state of the ceria substrate as a function of total copper coverage are measured using LEIS and X-ray photoelectron spectroscopy (XPS). In Chapter 5, the morphology and interfacial energetics of Cu on $CeO_{1.95}(111)$ at 100 K are studies using LEIS and SCAC where Cu adsorbs as isolated atoms in the first two calorimetry pulses which is the first ever measurement of its type. The Cu metal atom chemical potential can be estimated from this data from single atoms to the bulk particle-size limit.

Quantum mechanical energy based calculations using density functional theory (DFT) can be used as a high throughput screening method to test possible metal/oxide combinations for activity in catalytic reactions,[33] or for stability against deactivation (e.g., via sintering). In order to use DFT as a screening method, the absolute accuracy of the theoretical methods must be tested against experimental benchmarks. In the case of oxide supported metal catalysts, no adsorption energies of isolated atoms on stoichiometric terraces has ever been recorded, which is the simplest system that can be modelled by DFT. In the case of Cu atom adsorption to CeO_2(111), there is little agreement amongst different versions of DFT with respect to the value of the adsorption energy.[34-38] Part of the difficultly in modelling this system is describing the localized Ce 4f electrons. To properly localize the electrons, a Hubbard parameter is added to the functional, but using this correction has been shown to lead to inaccuracies in adsorption energies of molecules on ceria.[39] The adsorption energies of Cu atoms on stoichiometric ceria terraces described in Chapter 5 provide a much needed benchmark for validating future theoretical calculations that use new and improved DFT methods.

In Chapter 6, the interfacial energetics and structure of gold nanoparticles on reduced CeO_2(111) at 300 and 100 K are measured by SCAC and LEIS. Ever since gold, when in the form of nanoparticles, was discovered to have high catalytic activity or selectivity for a variety of chemical reactions, it has been extensively studied.[40,41] Despite high turnover frequencies and low operating temperatures used in catalysis by gold nanoparticles, deactivation due to sintering is still a major problem for these materials.[42] Ceria as a support for Au nanoparticles has been shown to inhibit their deactivation due to sintering because of high nanoparticle adhesion to ceria, potentially making it an ideal support for gold catalysts and an ideal candidate for improving catalysts.[10] In fact, Au supported ceria catalysts have been used effectively for a variety of reactions such as the water gas shift reaction[43] and CO oxidation in the presence of H_2.[44] Interestingly, the study presented here allowed us to recognize a trend in metal nanoparticle adhesion energy to ceria and how it varies from metal to metal: it increases with increasing heat of formation of the most stable oxide of the metal (from metal vapor plus O_2). This trend is compared to a previous trend of adhesion to MgO(100)[11] and give new fundamental insight into understanding which properties of the metal and of the oxide influence chemical bonding at metal/oxide interfaces.

One way to tune physical, chemical, and catalytic properties of a catalyst to be more active, selective, and sinter resistant, is to use bimetallic catalysts.[45] These systems exhibit properties unique from their parent metals, resulting from electronic interactions of dissimilar metal-metal bonds.[46] Bimetallic catalysts can exist in a variety of architectures such as metal overlayers, core shell nanoparticles, and various types of alloys, and the type of structure often depends on the reaction and synthesis conditions of these nanoparticles.[47] Copper overlayers on Pt(111) greatly affect the adsorption properties of small molecules such as CO,[48] CO_2,[49] formate,[50] and oxygen[51] compared to these molecules adsorption on clean Pt(111). In Chapter 7, the adsorption and adhesion energy of Cu overlayers on Pt(111) are measured by SCAC and interpreted with respect to well established growth morphologies.[52] While the adsorption energy is known for many metal-on-metal systems which involving immiscible metals based on TPD measurements,[45] this is the first measurement of the adsorption energy of any metal onto the surface of another metal with which it makes an exothermic alloy (since TPD fails in these cases). Copper adsorption energies onto Pt(111) give important insight into the thermodynamic driving force to form layer-by-layer structures compared to hemispherical cap nanoparticles often observed in the rest of this dissertation (for metals on oxides). Adsorption energies of this type can also be used as benchmarks to validate the energy accuracy of methods like DFT which are used to predict the energetics, structure and electronic properties of future bimetallic systems for applications in catalysis and beyond.

Chapter 2

Adsorption Calorimetry during Metal Vapor Deposition on Single Crystal Surfaces: Increased Flux, Reduced Optical Radiation, and Real-Time Flux and Reflectivity Measurements

This Chapter has been published as:
J.R.V. Sellers, T.E. James, S.L. Hemmingson, J.A. Farmer, C.T. Campbell,
Rev. Sci. Instrum., 2013, 84, 123901

Thin films of metals and other materials are often grown by physical vapor deposition. To understand such processes, it is desirable to measure the adsorption energy of the deposited species as the film grows, especially when grown on single crystal substrates where the structure of the adsorbed species, evolving interface, and thin film are more homogeneous and well-defined in structure. Our group previously described in this journal an adsorption calorimeter capable of such measurements on single-crystal surfaces under the clean conditions of ultrahigh vacuum (UHV).[17] Here we describe several improvements to that original design that allow for heat measurements with ~18-fold smaller standard deviation, greater absolute accuracy in energy calibration, and, most importantly, measurements of the adsorption of lower-vapor-pressure materials which would have previously been impossible. These improvements are accomplished by: (1) using an electron beam evaporator instead of a Knudsen cell to generate the metal vapor at the source of the pulsed atomic beam, (2) changing the atomic beam design to decrease the relative amount of optical radiation that accompanies evaporation, (3) adding an off-axis quartz crystal microbalance (QCM) for real-time measurement of the flux of the atomic beam during calorimetry experiments, and (4) adding capabilities for *in-situ* relative diffuse optical reflectivity determinations (necessary for heat signal calibration). These improvements are not limited to adsorption calorimetry during metal deposition, but also could be applied to better study film growth of other elements and even molecular adsorbates.

2.1 Introduction

Thin films of metals and other materials are grown by physical vapor deposition for a wide variety of technological applications, for example in the fabrication of microelectronics and computer parts, solar cells, light-emitting diodes, reflective and protective coatings, chemical sensors, and electrodes of various types. Thin films and nanoparticles are also grown by physical vapor deposition for a wide variety of fundamental research applications aimed at studying the properties of surfaces, interfaces, nanoparticles, and nanomaterials. A great deal of basic understanding of the film growth process, the thermodynamic stability of the resulting films or nanoparticles, and the strength of chemical bonding at the resulting interface(s) is provided by measuring the adsorption energy versus coverage during such deposition processes.[10,17,53-55] The strengths of chemical bonding at interfaces between materials have a remarkable impact on almost all areas of science, technology, and industrial manufacturing.[56] The adhesion energy between two solids can also be determined by measuring the adsorption energy versus coverage during vapor deposition,[53] even in cases where the deposited material grows as nanoparticles rather than a continuous film.[57] Adhesion energies define the relative stability of the interface, control the mechanical properties of composite materials, and define the shape of supported nanoparticles such as, for example, those used in catalytic or fuel-cell materials consisting of metal nanoparticles supported on high-area oxide or carbon supports.[9] In this latter example alone, the adhesion energy also dictates how the chemical potential of the metal atoms depends on the particle size and support material, which in turn controls catalytic reactivity and its deactivation by coarsening or sintering.[11]

Thus, there is great motivation to measure adsorption energies during physical vapor deposition of one material onto another. Such measurements are particularly enlightening when performed on the clean surface of a single crystal of the substrate material, since this enables better structural homogeneity and structural characterization of the adsorbed precursors, nanoparticles, and thin films whose energies are being measured.[6,58,59] We previously described in this journal the first adsorption calorimeter capable of such measurements of metal adsorption energies on single-crystal surfaces in a ultrahigh vacuum (UHV) chamber where the substrate surface cleanliness and the structure of the resulting thin film or nanoparticles could also be measured with surface analysis techniques.[17] Here we describe a new apparatus that incorporates several major improvements to the capabilities of that original design. These decrease the pulse-to-pulse standard deviation of the metal adsorption energy measurements by ~18-fold, while also improving the absolute accuracy of the energy calibration. Most importantly, these improvements allow for measurements of the adsorption energies of metals which would have been impossible to study with our earlier design, namely metals with very low vapor pressures or high heats of sublimation (e.g., Pt, Pd, Rh, Ni, Au, etc.).

The ability to determine heats of adsorption on clean surfaces of single crystals in UHV is not new. Techniques such as temperature programmed desorption (TPD) and equilibrium adsorption isotherm (EAI) analysis have often been used to measure adsorption properties of atoms and molecules on single crystalline supports. However, with these techniques, heats of adsorption are measured indirectly in a way that requires completely reversible adsorption. In cases where adsorption is not reversible, a technique for directly measuring heats of adsorption is necessary. Single crystal adsorption calorimetry (SCAC) was developed for such cases.[16] This approach is particularly important for studying metal adsorption and metal thin-film growth, since metal adatoms frequently sinter into very large particles or diffuse into the substrate upon heating at temperatures well below those necessary for desorption.[54,60] This was the motivation for designing the instrument mentioned above for SCAC of metal vapors.[17,53] Subsequently, it has been employed to measure the adsorption energies of several metals on a variety of different single crystal surfaces as a thin metal film is grown and the metal / substrate interface is formed.[10,12,14,53,57,61-69]

We describe here a new calorimeter for SCAC of metal adsorption energies which offers several important advantages over that previous design. It uses an electron beam evaporator as the metal atom source instead of the Knudsen cell metal evaporator previously used. This localizes the heat input to the surface of the metal melt and produces much less optical radiation than the Knudsen cell type metal vapor source, thereby increasing the signal/noise of the calorimetry measurements. The atomic beam design was also modified to further decrease the relative amount of optical radiation that accompanies evaporation. In addition, an off-axis quartz crystal microbalance (QCM) was added for real-time measurement of the flux of the atomic beam during calorimetry experiments, and optics were added that allow for *in-situ* relative diffuse optical reflectivity determinations (necessary for heat signal calibration).

These improvements allow more sensitive and accurate measurements of metal adsorption energies and the interfacial bonding strengths of a wider variety of metal / support systems. The methods described here are not limited to adsorption calorimetry during metal deposition, but also could be applied to study film growth of other elements and even molecular adsorbates that are relevant not only to heterogeneous catalysis, but also to technologies such as coatings, microelectronics, computers, optoelectronics and solar cells.

2.2 Experimental Details

The principles behind the design of this calorimeter have their basis in the ground-breaking designs from the group of Sir David King.[70-72] Their original single crystal adsorption calorimeter

(SCAC) design used optical pyrometry to measure the transient temperature rise that occurs upon adsorption of a pulse of gas from a molecular beam onto a ~0.2 μm thick single crystal. In a later experiment, the single crystal was fused directly onto a $LiTaO_3$ crystal, whose pyroelectric properties were used to measure the heat, allowing for improved sensitivity to heat released upon adsorption at low temperature,[72] although this technique was limited since the detector could not tolerate the high temperature annealing that is necessary for creating well-ordered surfaces for many materials. This new calorimeter described here instead uses a pyroelectric ribbon as the heat detector, which we introduced and improved previously.[17,73-75] and which has several important advantages over the heat detectors used by King's group.

A general schematic of the new calorimeter can be seen in Fig. 2.1. A thin polyvinylidene fluoride (PVDF) ribbon serves as the heat detecting element of our calorimeters, as described in detail elsewhere.[17,74] Briefly, the 9 μm thick ribbon consists of amorphous PVDF in which poled β-PVDF crystals, which are both piezoelectric and pyroelectric, are embedded. When brought into gentle mechanical contact with the back of a sample, the pyroelectric properties of β-PVDF respond to a slight increase in temperature with a measurable change in the face-to-face voltage of the ribbon. This method of heat detection increases the sensitivity by a factor of ~100 over detection via optical pyrometry at 300 K. This improvement factor is also estimated to increase as ($1/T^3$) with decreasing temperature of the single crystal (T),[16] thus allowing for routine cryogenic measurement that would have been impossible using optical pyrometry.

The samples are typically 1 μm thick single crystals,[17] although a new method for mounting the ribbons has been developed to allow the use of much thicker crystals.[74] When heat is transiently deposited on the face of a 1 μm crystal, as in the experiments described here, ~10% of the energy is transferred to the ribbon. The intimate thermal contact between the sample and the ribbon allows for the heat released from adsorption of a 100 ms pulse of gas to be detected almost instantaneously (i.e., with an instrument response time capable of detecting kinetic delays in heat deposition as short as 10 ms[76]). The measured calorimetric heat response in these instruments corresponds to the change in internal energy for the adsorption of the hot metal atoms in the beam onto the single crystal at its chosen temperature. The difference in temperature between the gas and the support is accounted for as described previously to give the adsorption energy for the system, with both gas and surface at the crystal's temperature, which is the negative of the internal energy change for adsorption (ΔU_{ad}).[17] Since the ideal gas law holds up to 1 bar, the standard enthalpy of adsorption (ΔH_{ad}) is just RT less than this change in internal energy: $\Delta H_{ad} = \Delta U_{ad} - RT$, where R is the gas constant and T is the temperature of the single crystal.[17] The heat of adsorption is defined here as the negative of this standard adsorption enthalpy. With this setup, we have been able to determine heats of adsorption to within 3% accuracy in most cases and with a point-to-point standard deviation of only 0.6 kJ/mol when depositing 2% of a monolayer per pulse, and a temperature range of 100 to 350 K.[74]

The basic design of this new calorimeter is similar to two other calorimeters that have been constructed previously by our group for measuring the heats of adsorption for various systems.[17,73,74] The metal atom adsorption calorimetry, sample preparation, and surface characterization are all performed in a single UHV system, with a four-axis translator used to manipulate the sample in vacuum.

Surface characterization spectroscopies are performed using a PHI 10-360 precision energy analyzer equipped with a PHI 72-250 position sensitive detector, which is used to measure the kinetic energy distribution of electrons or ions originating from the sample surface after irradiation by an electron beam for Auger electron spectroscopy (AES), an x-ray beam for x-ray photoelectron spectroscopy (XPS), or an ion beam for low energy ion scattering spectroscopy (LEIS). This combination of techniques provides detailed information on the surface structure, with XPS or AES analysis providing information on the elemental composition of a surface down to ~3 nm from the surface, and LEIS providing the elemental composition of the top-most atomic layer. The chamber is also equipped with a low-energy electron diffraction (LEED) screen, which allows for verification of the crystallinity of the sample and any thin film grown on its surface. The instrument also includes a sample preparation chamber that can be closed off with a gate valve during preparation of the single crystal's surface in order to protect the UHV conditions in the calorimeter and surface analysis region.

The most significant improvement in this calorimeter involves the method for generating the pulsed atomic beam of metal atoms. The SCAC measurements require a very high flux from a source located far from the sample in order to reduce optical radiation from the oven. Typical fluxes are 4×10^{14} atoms/cm^2/s at the sample, which corresponds to $>4 \times 10^{17}$ atoms/cm^2/s at the source located 353 mm away (if we approximate the source as a 15 mm diameter sphere). The original metal atom adsorption microcalorimeter design uses a Knudsen cell type thermal evaporator as the metal adatom source.[17] In the Knudsen cell, the entire metal crucible is heated to the temperature required to evaporate or sublimate the metal of interest. This system has been used successfully to study the heats of adsorption of Li,[68] Ca,[67] Pb,[61,64] Ag,[57] and Cu.[62] However, heating this large element to the high temperatures (upwards of 1660 K for Cu) required for the very high fluxes necessary in our calorimetry experiments produced too much background radiation that also contributes to the measured heat signal, and it therefore proved unsuitable for studying metals with larger enthalpies of vaporization than that of Cu. The excessive heat load from the Knudsen cell also causes problems with background pressure increase for such metals, which can give rise to surface impurities.

To overcome this issue, we have instead used a Thermionics 150-0010 crucible-fed electron beam evaporator as the source for the metal atom beam. Its 4 kV electrons are focused directly onto the surface of the metal to be evaporated, thereby localizing the heating to the metal itself. The metal to be evaporated is electrically grounded so that there is no difference in potential between the metal source and the single crystal, thus preventing acceleration of any charged species from the source to the sample. We found that electron beam evaporation allows for a significant flux of evaporated metals with a significant reduction in the heat and source radiation output when compared to a traditional Knudsen cell, and therefore will allow us to use this new calorimeter with metals such as Pt, Pd, Rh, Ni, and Au. This also results in lower background pressures at higher evaporation temperatures for any metal, thus decreasing surface contamination.

The evaporated metal atoms are used to create a temporally- and spatially-resolved pulsed atomic beam by passing them through a chopper and a series of collimating apertures. The metal atom beam is typically chopped into 100 ms pulses at a rate of 0.5 Hz, although both the duration of each pulse and the time between pulses can be varied. The spatial distribution of the metal atom beam is defined by two apertures. The first 4.00 mm diameter beam-defining aperture is located 33.4 mm from the lip of the crucible, with the metal melt estimated as being an additional 3 mm further from the aperture. A second beam-defining 4.00 mm aperture is located 295.9 mm further downstream from the first aperture, and is positioned 19.2 mm from the sample surface. This geometry results in a circular deposition area with ~89% of the metal atoms deposited within an umbra of 4.00 mm in diameter. Line of sight calculations were used to determine that the resulting spot has an outer penumbra with a diameter of 4.52 mm. Images of white light projected down the beam path accurately reproduce the ratio between the umbra and the outer penumbra. Assuming a linear gradient in the deposition thickness versus radius beyond the umbra gives an effective beam diameter of 4.26 mm and an effective deposition area of 14.3 mm^2 for a square beam profile of the same intensity as in the umbra and with the same area-integrated intensity as the entire real beam spot.

The flux of the metal atom beam is measured using a quartz crystal microbalance (QCM) that is positioned in front of the sample. A UTI 100C quadrupole mass spectrometer (QMS) in line-of-sight to the sample provides a signal that is proportional to the number of metal atoms reflected from the surface and can be used to determine the fraction of atoms in each pulse that stick to the surface using a modified King and Well's method.[77] The QMS ion source is located at the "magic angle" of θ = 35° from the surface normal in order to minimize deviations in signal due to changes in the angular distribution of the atoms leaving the surface.[17] The sticking probability of each pulse is measured simultaneously with its heat. A heated Ta flag is placed in the sample position before or after these measurements to record the QMS signal associated with zero sticking probability (100% reflected), and with this information we can determine the fractional sticking probability of the gaseous atoms in each pulse. Multiplying this sticking probability by the metal atom flux gives the incremental increase in surface coverage associated with that pulse. The details of this analysis have been presented previously.[73]

The voltage response of the PVDF ribbon to the applied energy is usually calibrated using a stabilized HeNe laser that is first diffused with a lens and then directed along the atomic beam path using a translatable mirror. By passing the laser through the same apertures and choppers as the atomic beam, the calibration pulse reaches the sample with the same spatial and temporal distribution as that of the atomic beam pulse. The laser power at the sample position is determined by positioning a mirror in front of the sample that reflects the beam through a quartz window equipped with a power meter. This measured value is scaled using a previously determined linear relationship between the laser power at the window and the laser power at the sample position. Using this method, the voltage response of the ribbon to transient energy changes can be calibrated directly before each experiment. The heat detector's response intensity is proportional to laser pulse energy over the range of deposited energies used in our experiments.[17] However, the optical reflectivity of ceria-coated Pt samples was not known due to changes from run to run due to differences in ceria film thickness. Therefore we scaled the absolute calibration factor slightly so that the multilayer heat of adsorption in the high-coverage limit equals the literature value for the heat of sublimation of bulk Metal(solid) from Ref.[78].

The evaporation sources used in our metal atom beams heat the metal to a temperature at which sublimation or evaporation occurs rapidly. The optical radiation from these hot sources is included with each pulse, and its contribution to the heat signal must be measured and subtracted. This is accomplished using a BaF_2 window, which can be translated into the atomic beam path. The window blocks all metal flux, but is >90% transparent to photons between 300 nm and 9.5 μm in wavelength.[79] The heat signal from the HeNe laser passing through this window is periodically measured in order to determine its exact transparency, which decreases with use over its lifetime. Thus, the heat signal due to optical radiation from the source is measured using this BaF_2 window, corrected for transparency, and subtracted from the total heat signal, to determine the portion of the signal that corresponds to the actual heat of metal atom adsorption, as described previously.[17]

Both the thermal reservoir of the calorimeter and the sample manipulator fork are plumbed with internal tubes for carrying gaseous or liquid nitrogen at controlled temperature, which are used to either cool or warm these parts during experiments, as described previously.[74] In brief, two streams of heated or cooled gases are mixed in various ratios and flowed through these lines, allowing us to perform calorimetry experiments over a wide range of temperatures. Similar setups on our other calorimeters have enabled effective measurements of heats of adsorption on surfaces at any temperature between 100 and 300 K.[74] In principle, hot water could also be used to heat our thermal reservoirs, allowing for stable sample temperatures between 77 and 350 K.[74] Since surface mobility of adsorbed metal atoms decreases with temperature, metal atoms deposited at lower temperatures will grow as smaller, more dispersed nanoparticles. Performing these calorimetry experiments over a large range of temperatures will allow us to determine the effect that particle size has on heats of adsorption. The relationship of surface dispersion and particle size to energetic stability and reactivity are extremely important for understanding heterogeneous catalytic applications of nanoparticulate metals.

2.3 Real-time Flux Determination in the Metal Atom Beam

In order to analyze the calorimetry data, the flux of the metal atoms colliding with the sample surface must be known at all times. In previous calorimeter designs for SCAC, this was accomplished by measuring the flux before and after the experiment to prove that it had been stable during the calorimetry measurements.[16,17,73] However, this requires a stable beam flux, which is more difficult to accomplish with metals with high vaporization enthalpies, as desired here. In other groups, stabilization of the metal flux of an e-beam evaporator has been accomplished by controlling the e-beam emission current with feedback loops which monitor either the ion current associated with the ~1% of metal atoms that are ionized in by the e-beam evaporator of the atomic beam[80,81] or the atomic adsorption spectrum of the metal atoms in the beam.[82] This new system was originally set up with a rod-fed e-beam evaporation source. Attempts were made to stabilize this source using the ion current, but it was found that, with the high fluxes required, sudden changes in the shape of the tip of the rod caused large instabilities in the flux which could not be overcome. To minimize the effects of the changing shape of the metal source on the flux, we switched to the crucible-fed evaporator described above.

An off-axis QCM was installed so that the flux of the source can be monitored at all times during the calorimetry experiments. This monitor QCM was installed 225 mm from the metal source (compared to 353 mm to the sample) at a 70° angle from the atomic beam path to the sample. This QCM head was mounted directly onto a cooled 4.5” conflat flange to reduce its temperature drift and fluctuation. Using a QCM to stabilize the flux of an e-beam evaporator is a well-established practice [83], but in our system the ratio between the flux at the sample position and the flux at the monitor QCM was found to increase as the flux decreases over time when the evaporator is run at constant emission current, as can be seen in Fig. 2.2. For this reason, simple feedback regulation of the flux failed in this instrument.

Instead, we developed a scheme to determine the real-time flux at the sample position based on the flux at the monitor QCM (seen in Fig. 2.1), which can be recorded simultaneously with the calorimetry data. An example run using Cu is illustrated in Fig. 2.2(a), where the physically measured values are plotted along with the calculated fits. The ratio between the fluxes of the two QCMs is measured before and after the calorimetry experiments. As shown in Fig. 2.2(b), this ratio was found to increase linearly with time while the source is being operated at constant emission current (provided the source has not used up almost all of its metal load). A linear fit to the ratio of the experimentally measured fluxes at the beginning and end of the calorimetry experiment (seen as a solid black line in Fig. 2.2(a)) was used to scale the flux at the monitor QCM so that it represents the actual flux at the sample position in real time over the entire duration of the calorimetry experiment. The end result is plotted in Fig. 2.2(a) as a solid red line. Monitoring flux in real time in this way not only allows for more accurate calculations of heats of adsorption vs. coverage, but also allows us to use data sets in which there is a sudden shift in the flux of the metal atom beam, which can occur due to flow effects in the metal melt in the crucible and are especially problematic at high evaporation rates.[84]

2.4 Optical Radiation from the Metal Atom Beam

When any metal evaporation source is used as a directed doser, as is the case in our calorimetry experiments, the atomic flux is also accompanied by optical radiation from the hot source. This contribution to the heat signal must be measured and subtracted from the signal in order to correctly determine the heat of adsorption.[17] In our instrument, the source is located 353 mm from the sample and is collimated to a 4 mm diameter beam. This distance is necessary to minimize the effect of the radiated heat from the oven, which decreases as the square of the distance. However, the flux per unit area from an effusion oven also decreases as the square of the distance. Because of this, very high temperatures in the source are required to reach the fluxes necessary for the signal/noise of our experiments (~0.5 Å/s at 353 mm). Fortunately, the flux increases with temperature as an Arrhenius equation (proportional to $e^{-\Delta H_{vap}/RT}$, where ΔH_{vap} is the enthalpy of vaporization for molten metals) while the optical radiation increases only as ($\sim T^4$). For the enthalpies of vaporization of typical metals, the increase in flux is much faster than the increase in radiation, so that higher temperatures give larger fluxes and have a smaller contribution from optical radiation in this design.

In our original metal atom source for SCAC of metal vapors, the source-to-sample distance is ~330 mm, with the first beam-defining aperture 108 mm from the source (which was necessary due to the dimensions of the commercial thermal evaporation oven) and only 87 mm between the first and last beam-defining apertures.[17] Geometric constraints resulted in a situation in which the sample has direct line-of-sight to not only the metal melt in the thermal evaporator, but also to a portion of the heated crucible. In this new calorimeter, we have increased the source-to-sample distance by 13% while drastically reducing the distance between the source and the first beam-defining aperture to 33.4 mm and increasing the distance between the first and last beam-defining apertures to 295.9 mm. With this new geometry, the sample can now see only a 4.90 mm diameter portion of the metal source, which is substantially less than the ~15 mm diameter e-beam evaporator crucible.

The overall combined effect of the changes in geometry along with the new type of metal atom source on the thermal radiation from the evaporative oven can be seen in Fig. 2.3, where the voltage responses of the pyroelectric detectors to adsorption of gaseous Cu atoms on ~17 ML of Cu on ~1 μm single crystals are shown as black lines for the different experimental setups. One monolayer (ML) here is defined as the Cu(111) surface density of 1.77×10^{15} atoms/cm^2. The solid blue lines are the corresponding optical radiation component in each pulse measured through the BaF_2 window, where these values have been scaled by the inverse of the measured transmission of BaF_2 (~90%). The difference in the two solid lines is proportional to the heat response from only the adsorption of the gaseous metal atoms, and is plotted as a dashed red line to which the other data is normalized.

In Fig. 2.3(a), the signal for 0.014 ML Cu pulses (which correspond to a flux of ~0.3 Å/s at the sample in our systems with the Cu melt at 1500 to 1510 K) adsorbing onto 17 ML of Cu on a ~4 nm MgO(100) film on Mo(100) from our older calorimeter using a Knudsen cell[17] are shown. As seen, the optical radiation accounts for ~65% of the total heat signal. In Fig. 2.3(b), the signal for 0.014 ML Cu pulses adsorbing onto 17 ML of Cu on Pt(111) in this new calorimeter using an e-beam evaporator are plotted in the same manner. In this case, the optical radiation is reduced to only ~14% of the total signal, which greatly improves the signal/noise ratio in the final heat of adsorption determinations. Since the Cu source was almost the same distance from the sample in these two cases (it is 7% longer in this new design), and the Cu flux is the same, the effective temperature of the Cu source (which defines the evaporation rate) was almost the same, but the new e-beam source clearly generates much less optical radiation at the detector. The difference in the line shapes between the two instruments is merely due to the use of a different time constant for the high-pass filter.

It should be noted that some of this apparent improvement is probably due to the difference in reflectivity of the samples. However, based on the reflectivities of Mo ($R \approx 0.57$ [85]) and Pt ($R \approx 0.76$ [86]), the maximum reduction in absorbance of optical radiation for the sample used in the e-beam evaporator (compared to that in the Knudsen cell experiment) would be 44%. We instead see a reduction in the absorbed optical radiation of 92%. This proves that there is a minimum 51% reduction in optical radiation reaching the sample with our new calorimeter using an e-beam evaporator. It is likely that this improvement is even greater considering that the reflectivities of the two samples should be approaching that of bulk Cu as the metal coverage increases. However, this may not be entirely due to the difference in the metal sources, as it is impossible to rule out a contribution from decreased internal reflections in the atomic beam path due to improvements in the design of the light baffles.

Since this new metal atom beam is capable of easily generating much larger fluxes of gaseous metal atoms without any significant rise in the background pressure, and since the atomic flux increases with temperature much faster than the optical radiation flux, the ratio between the radiative and adsorption heats can be further improved as needed. Fig 2.3(c) shows heat pulses from the same instrument onto the same sample used in Fig. 2.3(b), but the flux has been increased by a factor of ~4 to 0.058 ML per pulse (a flux of ~1.2 Å/s at the sample). In order to achieve this larger flux, the temperature of the melt was increased to 1600 K by increasing the emission current of the e-beam evaporator. This results in a decrease in the optical radiation with respect to the total heat signal, so that the optical radiation now only accounts for 7% of the total heat signal. This high-temperature capability also proves that we will be able to use this atomic beam to perform adsorption calorimetry measurements with metals that have higher enthalpies of vaporization than Cu, such as Au and Pt.

Based on the T^4 temperature dependence of the optical radiation, we expected an increase in optical radiation of only 26% in Fig. 2.3(c) compared to Fig. 2.3(b), yet its signal nearly doubled. This could be due to an increase in the relative contribution to the optical radiation signal from indirect light coming from the hot crucible and filaments in the e-beam evaporator. Therefore, increasing the number of baffles for blocking indirect radiation could allow for an even greater reduction of the radiation reaching the sample, which would further increase the signal/noise ratio in our calorimetry measurements.

2.5 Real-time *In-situ* Relative Diffuse Optical Reflectivity Determination

When using the laser to calibrate the calorimeter’s heat response, the optical reflectivity of the sample must be taken into account. This is also true when correcting for the optical radiation from the hot metal source of the beam. Reflectivities of single crystalline metal samples are taken from literature, and are also compared to integrating sphere measurements performed at atmospheric pressure. However, deposition of a thin film changes the reflectivity of a single crystal even when the overlayer thickness is much less than the wavelength of light.[87-89] This effect is generally linear with coverage, though nanoparticulate films with particles in the 20-100 nm range cause more rapid changes in the reflectivity versus coverage than equivalent films of uniform thickness.[90]

Previous attempts at UHV *in-situ* direct relative optical reflectivity determination have measured the change in spectral reflectivity[91] or attempted to estimate diffuse reflectivity by measuring the total angular-integrated change in reflectivity over a larger area.[65] For our purposes, the diffuse reflectivity is more appropriate since we need to know the total amount of light absorbed by the sample. Determination of the relative diffuse reflectivity using the absorbed portion of an incident heat source measured with a pyroelectric detector, such as the one in our calorimeter, has also been proposed and applied.[65,92,93]. In previous SCAC experiments, the voltage response of the PVDF ribbon to laser pulses on the sample surface was measured as a function of coverage by interrupting the metal deposition at several points during coverage build-up.[65] This method introduces a ±3-4% error associated with repositioning the mirror to reflect the laser through the atomic beam path. Also, because of the time required, it has only ever been performed over large coverage steps and is usually not repeated in successive experiments.

In an attempt to more accurately account for the change in reflectivity with coverage, and to allow real-time measurements of the reflectivity during the course of an experiment, we have designed and built a setup for performing *in-situ* relative diffuse optical reflectivity determinations. A beam sampler, seen in Fig. 2.1, picks off 5% of the HeNe laser intensity used for calibrating the calorimeter's heat response and reflects it directly onto the sample at a 45° angle of incidence. It has been shown previously that changes in optical absorbance estimated using direct measurements of the relative total angular-integrated reflected light intensity at an incident angle of 45° agree well with changes in the absorbance of laser pulses normal to surface.[65] An external chopper and aperture are used to break the 45° beam into pulses of the same time duration and spatial distribution as that of the pulses travelling down the atomic beam, for convenience. The external chopper is synchronized with the internal chopper of the beam line, with the ability to change both the pulse window and the duration between pulses so that there is no overlap in the heat signal. This staggering is accomplished by having the chopper wheels pause in a closed position for a fixed amount of time. This setup also allows deposition of multiple pulses of metal atoms between each laser pulse, saving both time and material.

The laser-on-sample measurements can now be made without the need for any mechanical manipulation, and the change in diffuse optical reflectivity can be calculated without the noise associated with repositioning the mirror. A sample run, where the heat pulses from the calorimeter are simulated by the laser reflected down the beam path, is seen in Fig. 2.4. The black portions of the curve are the signal response due to heat from the atomic beam path, while the red portions are the response from the 45° laser pulses. All pulses still have the typical 2 s interval and 100 ms window, but with an absorbance measurement occurring after every second pulse from the beam path. In this manner it is possible to monitor the relative diffuse optical reflectivity in real time during the entire calorimetry experiment at coverage increments as low as 1% of a monolayer. As the coverage increases, the reflectivity of the sample will eventually reach the bulk reflectivity of the deposited metal. Using literature values for bulk metal reflectivities allows for determination of the absolute diffuse optical reflectivities of clean single crystalline oxide thin films.

2.6 Absolute accuracy of Heats of Adsorption for Metals on Single-Crystalline Supports from SCAC

In this section we show a simple example application of this new atomic beam source for measuring heats of adsorption on single crystals. Figure 2.5 shows typical measurements of the heat of Cu atom adsorption on Cu multilayers on Pt(111) at 300 K. The voltage response of the β-PVDF ribbon as seen in Figs. 2.3(b) and 2.3(c), along with the flux and radiation determinations described above, were used to determine the heat of adsorption per mole for each pulse of the atomic beam, as described previously.[17] The standard small corrections for the excess translational energy of the hot, gaseous metal atoms in the beam above their energy at 300 K and for the conversion from internal energy to enthalpy have also been applied, as described elsewhere,[17] so that the *y*-axis values plotted in Fig. 2.5 equal the heat of adsorption (defined as the negative of the standard enthalpy of adsorption with both the surface and gas at 300 K, $-\Delta H_{ad}$). The heat measurements shown in Fig. 2.5 were performed for Cu pulses containing 0.017 ML of Cu adsorbing onto clean Pt(111) at 300 K. Shown here is a single run of 100 Cu pulses over the multilayer coverage range from 4.5 to 6.2 ML. Copper is known to grow layer-by-layer on Pt(111) when vapor deposited in UHV at 300 K,[94-97] so the data presented in Fig. 2.5 represents the multilayer heat of adsorption, which is equal to the enthalpy of sublimation of bulk Cu (337.4 kJ/mol[1]) at these conditions. This is generally true for metals that grow in a continuous film, as they typically do at room temperature and above.

The pulse-to-pulse standard deviation in the heats of adsorption in Fig. 2.5 for the 100 data points shown, about their average value (equal to the bulk enthalpy of sublimation of Cu), is 0.83 kJ/mol, or 0.25%. This standard deviation is a factor of ~18 better than that reported using our previous Knudsen cell atom source (which gave standard deviations for multilayer Cu adsorption of 6% using 0.01 ML/pulse and almost 2% with ~0.03 ML/pulse [17], which interpolates to 4.6 % for the flux used in Fig. 5 of 0.017 ML/pulse). The pulse-to-pulse standard deviation in measuring the heat from simple laser pulses, for the 13 calibration pulses used in the same experiment as Fig. 2.5 and which deposited almost the same amount of heat per pulse as in Fig. 6.5, was also 0.25%. This implies that this standard deviation of 0.25% in Fig. 2.5 is dominated by the noise in the pyroelectric heat detection system rather than from variations in the metal atom flux or additional noise due to heat from the optical radiation. The 18-fold decrease in relative standard deviation compared to our previous measurements of the heat of Cu adsorption is mostly due to an improvement in the design of the heat detector reported previously[74] and incorporated in this new system, but approximately one-third of this improvement is due to the removal of a large amount of heat signal from optical radiation, which also contributes to the noise.

We have previously shown that the absolute accuracy of heat of adsorption measurements with this type of SCAC heat detector and laser calibration method is within 3%, after averaging several runs.[98] This was done by comparing the average multilayer heat of adsorption of four different molecules to their known bulk enthalpies of sublimation at the same temperatures. Since these same methods are used here, similar accuracy can be expected.

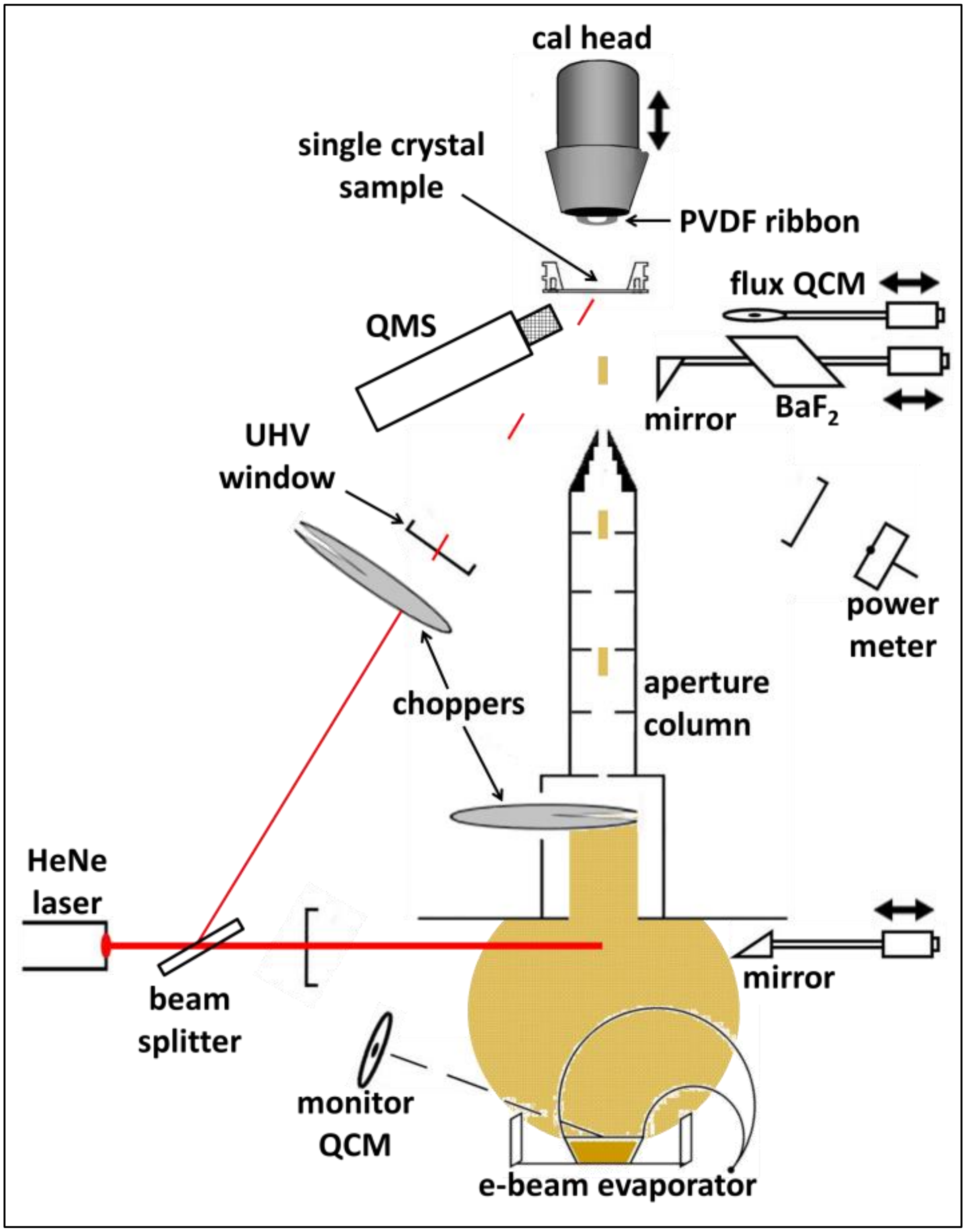

Figure 2.1: A schematic of the calorimeter, which uses an e-beam evaporator and a chopper to create a pulsed atomic beam of gaseous metal atoms (copper colored in the figure) which impinges upon the surface of a single crystalline sample. The transient heat input due to the adsorption of each gas pulse is detected by a flexible pyroelectric PVDF ribbon that is gently pressed against the back of the single crystal. As shown, this ribbon is mounted in the shape of an arch on the "cal head", which can be translated to bring the ribbon into contact with the single crystal, or removed for crystal cleaning and surface analysis. The single crystal is mounted to a platen, which sits on a fork on a thermal reservoir during calorimetry but is moved for surface analysis. Also illustrated are the components for the real-time flux and relative reflectivity measurements. Not to scale.

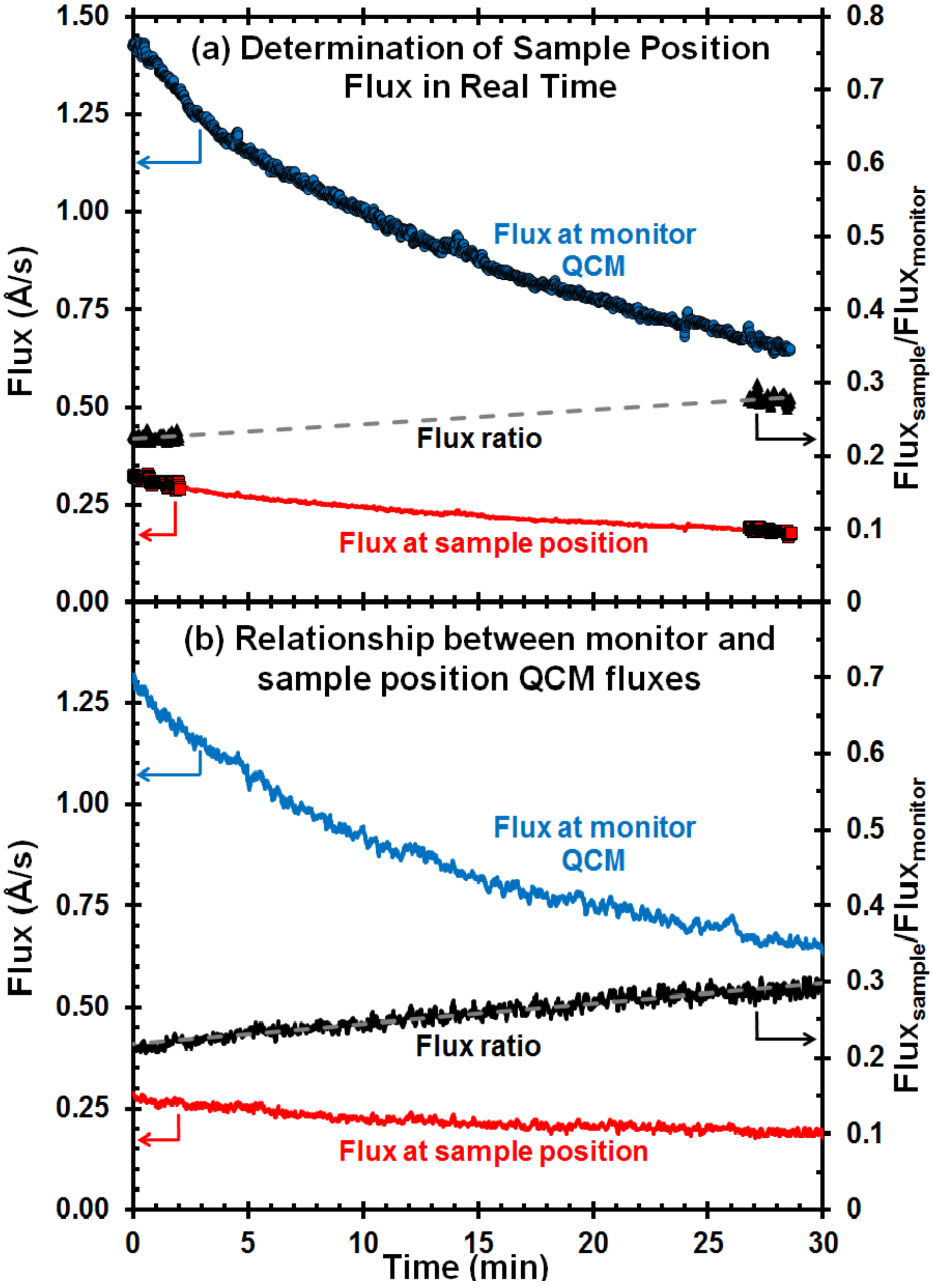

Figure 2.2: (a) Plot of the flux from the electron beam evaporator running at constant emission current vs. time at both the sample position QCM and the off-axis monitor QCM. Measured flux data are plotted as points, while the calculated flux at the sample position is plotted as a continuous red line. Also plotted is the ratio between the two fluxes, which is fit to the linear dashed line as a function of time. The flux ratio is used to calculate the flux at the sample position based on the flux at the monitor QCM. (b) Similar data for a control run where the flux was collected with a QCM located at the sample position throughout the entire experiment. This shows that the changing flux ratio is well approximated as changing linearly with time. The dashed line showing the best linear fit to the flux ratio is essentially hidden within the scatter of the data.

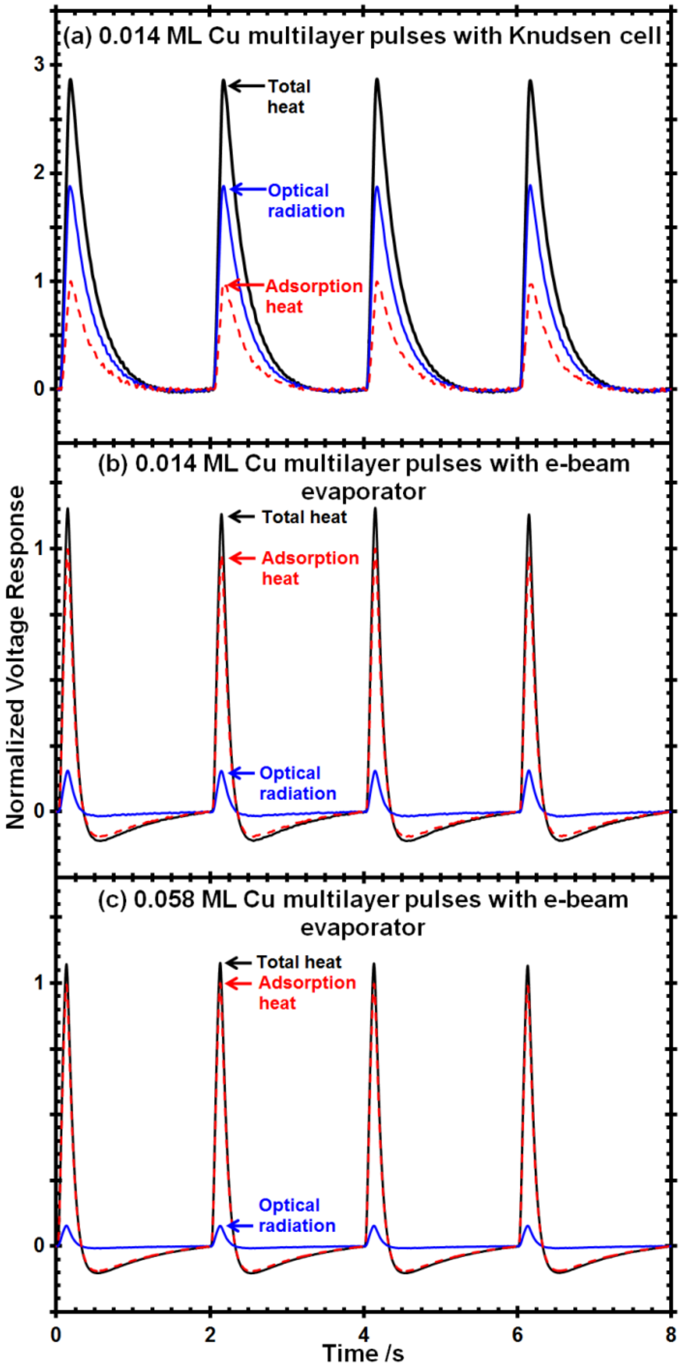

Figure. 2.3: Calorimetry heat pulses as detected via SCAC from Cu adsorbing onto ~17 ML of Cu on ~1 μm single crystals at 300 K, where the Cu vapor was generated by: (a) the Knudsen cell used in our earlier calorimeter [17], and (b) and (c) the e-beam evaporator of this new instrument. The solid black lines are calorimetry data from Cu atom pulses, the solid blue lines are the heat due to optical radiation from the hot metal source (measured through the BaF_2 window at the end of the experiment) and the dashed red lines are the heat signal due only to Cu adsorption, as determined by the difference in the two solid curves. These signals are for (a) 0.014 ML pulses of Cu from the Knudsen cell used in our earlier calorimeter [17] onto ~17 ML Cu on Mo(100) (pre-coated with 4 nm of MgO(100), which only slightly changes the reflectivity [62]), (b) 0.014 ML pulses of Cu from the e-beam evaporator onto ~17 ML of Cu on Pt(111), and (c) 0.056 ML pulses of Cu from the e-beam evaporator onto ~17 ML of Cu on Pt(111). The differences in line shapes arise from differing time constants for the high-pass filters and differences in the quality of the sample – detector thermal contact. Curves were smoothed with a low-pass filter. One ML is defined as the Cu(111) surface atom density, 1.77×10^{15} atoms/cm^2.

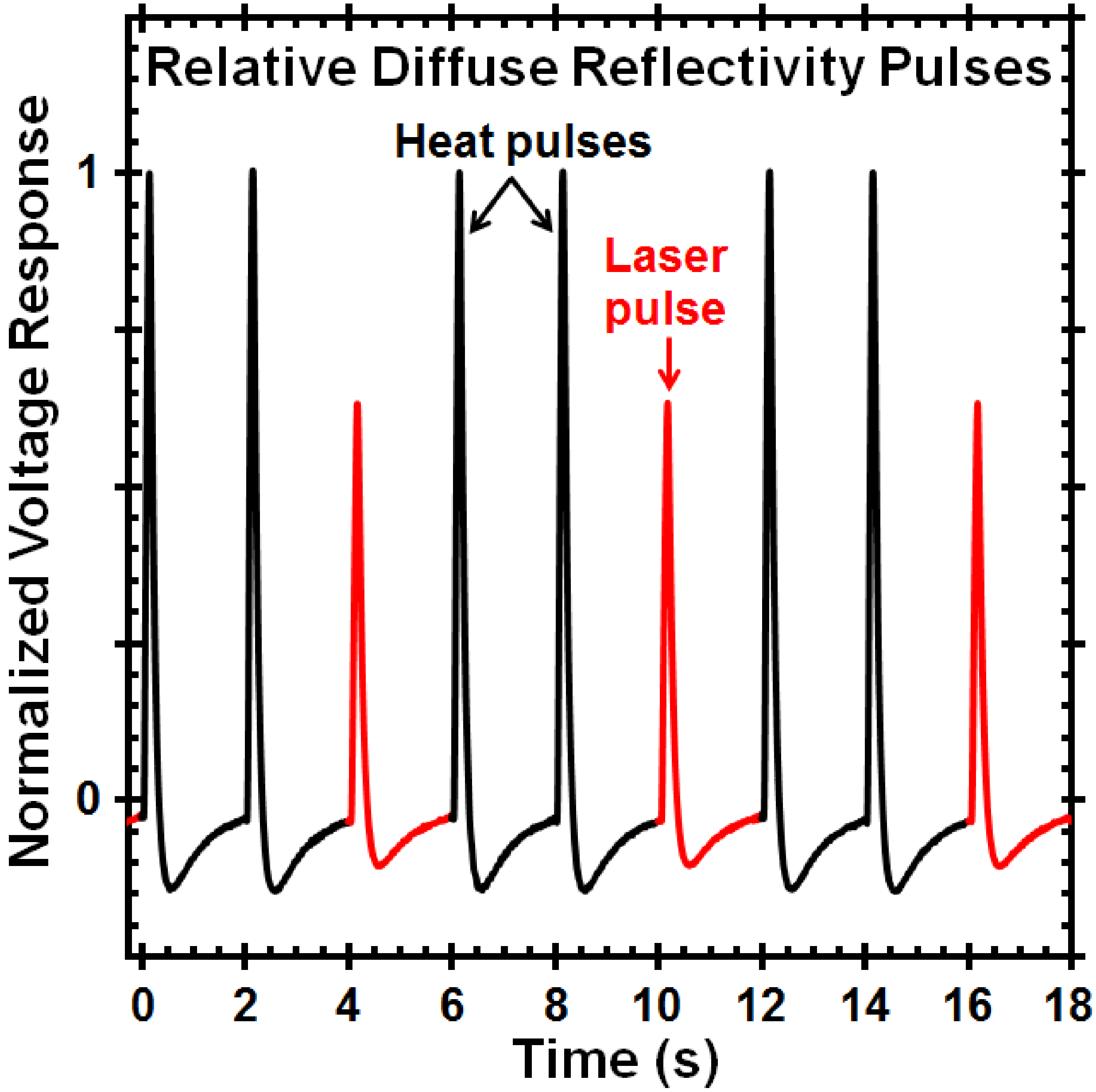

Figure 2.4: A sample run demonstrating the *in-situ* relative diffuse optical reflectivity measurement. Every third pulse from the metal atom beam line is replaced with a pulse from a HeNe laser at a 45° angle of incidence. The black portion of the curve is the response to heat deposition from the atomic beam line, while the red portions are the heat response from the laser. In this manner the absorbance of the sample at 633 nm can be monitored throughout the experiment so that the reflectivity of the sample can be accurately determined at all coverages. Heat pulses from the atomic beam were simulated with a laser directed down the atomic beam path in this example.

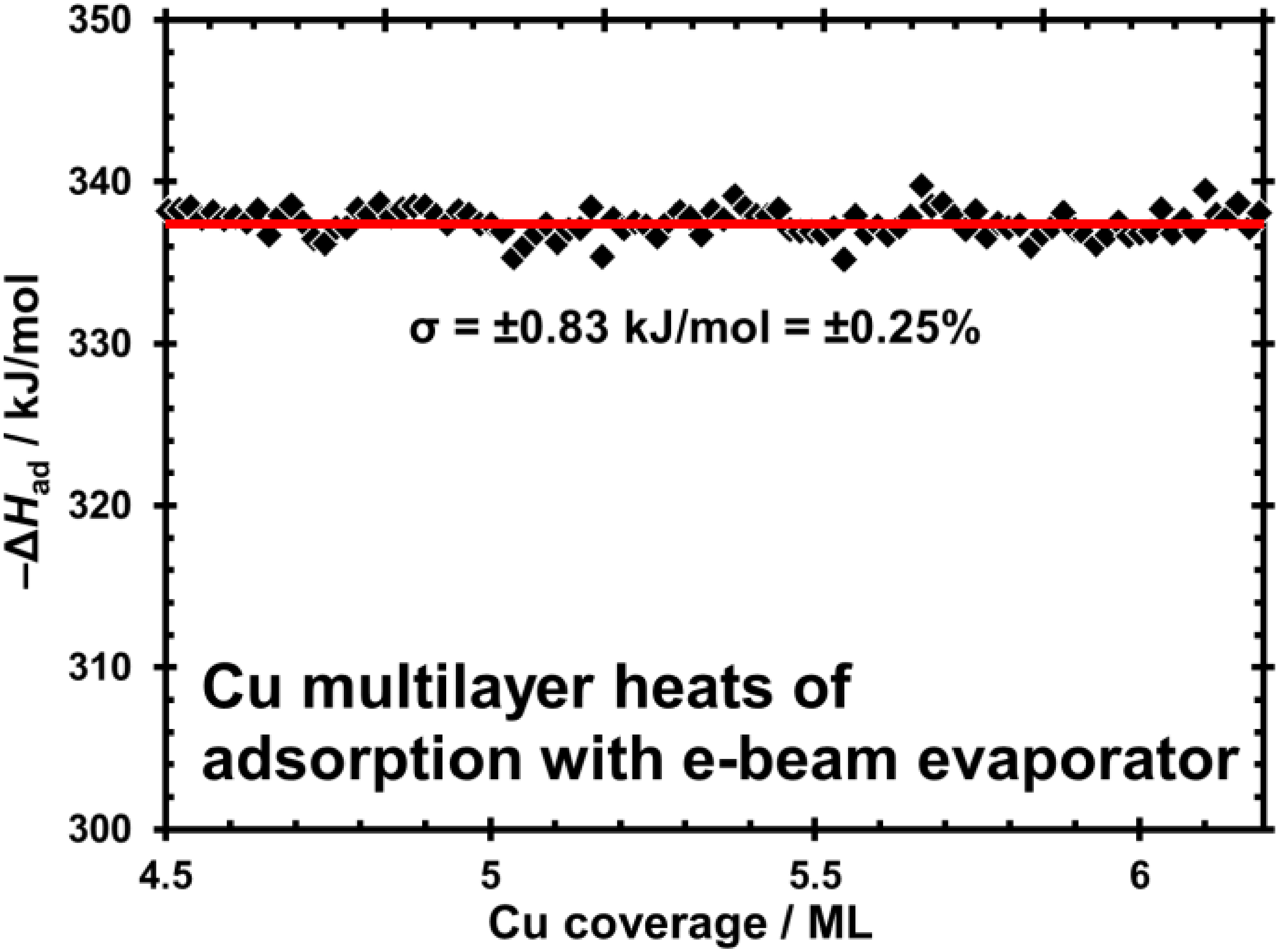

Figure 2.5: Heat of adsorption versus coverage for 100 pulses of Cu (each pulse containing 0.017 ML) onto a Cu multilayer on Pt(111) at 300 K. The data in the figure have been normalized so that their average value equals the literature value for the enthalpy of sublimation of bulk Cu solid at 300 K (337.4 kJ/mol [1], shown as the solid red line), to remove a small error in absolute calibration. The pulse-to-pulse standard deviation is 0.83 kJ/mol. One ML is defined as the Cu(111) surface atom density, 1.77×10^{15} atoms/cm^2.

Chapter 3

Ion Scattering Spectroscopy Intensities for Supported Nanoparticles: the Hemispherical Cap Model

This Chapter has been published as

C.T. Campbell, T.E. James, *Surf. Sci.,* 2015, 641, 166-169

Nanoparticles of one element or compound dispersed across the surface of another substance form the basis for many materials of great technological importance, like catalysts, fuel cells, sensors and biomaterials. Nanoparticles also often grow during thin film deposition. The size and number density of such nanoparticles are important, often estimated with electron or scanning tunneling microscopies. However, these are slow and often unavailable with sufficient resolution for particles near 1 nm. Because the probe depth of low-energy ion scattering spectroscopy (LEIS) with He^+ and Ne^+ is so shallow (less than one atom), it provides quantitative information on the fraction of the surface that is covered by such nanoparticles. Combined with the total amount per unit area, this fraction provides the average particle thickness. When the ions are incident or detected at some angle away from the surface normal, macroscopic screening effects cause interpretation of LEIS signals in terms of area fraction covered to be complicated. In this paper, we report a geometric analysis of particles with the shape of hemispherical caps so that LEIS signals obtained in any measurement geometry can also be used to quantitatively determine the area fraction, average particle thickness and diameter, or number density of particles.

3.1 Introduction

A very common structural motif in materials science involves nanoparticles of one material dispersed across the surface of another. Such structures are commonly encountered when making and/or studying catalysts, microelectronics, plasmonic and optical devices, nanoelectrode arrays, sensors, coatings and thin film growth by vapor deposition or other condensation processes. For example, metal nanoparticles dispersed across the surfaces of oxides and carbon supports are key ingredients in many heterogeneous catalysts, fuel cells, other electrocatalysts and photocatalysts, all of which are crucial for energy, fuel and environmental technologies and chemical processing. One of the three growth modes that occur during thin film growth by vapor deposition is the Volmer-Weber mode, whereby clusters of the deposited material first nucleate and then grow as 3D nanoparticles on the substrate.[9,10,14,19,20,99,100]

3.2 Theory

A method to estimate the size and number density of such nanoparticles is based upon measurements of the intensities of peaks associated with substrate and adsorbate elements using low-energy ion scattering spectroscopy, LEIS. A model that has been applied for analyzing these LEIS intensities is the hemispherical cap model introduced by Diebold et al.,[21] which assumes that the nanoparticles all have the shape of hemispheres and the same diameter. It is often applied to cases where the LEIS intensities of substrate and adsorbate peaks have been measured versus the amount of adsorbate deposited on the flat substrate surface, in which case the further assumption is made that the number of particles per unit area remains constant. This assumption is based on the well-known fact that in many such systems, the number density of particles increases in the first few percent of a monolayer (ML), but quickly reaches the so-called saturation density, after which it stays nearly constant until very high coverages.[19] This number density is estimated from a fit to these plots of intensities versus coverage (or the intensities at any one coverage) to the resulting equations of this hemispherical cap model, which also gives the average diameter of the particles at each coverage.[21] Unfortunately, those equations for the hemispherical cap model only were intended to apply to one measurement geometry (when the ions are incident 45° from normal and the scattered ion intensities have been measured for a take-off angle normal to the substrate surface). Unfortunately, there is an error in that equation. Here, we present a correction and extension of that model that allows it to be applied at any angles of incidence and detection. Other angles are often demanded by the constraints on sample mounting or manipulation imposed by the particular vacuum chamber being used.

Here we consider LEIS using noble gas ions like He^+ at energies below 2 kV. Since such ions get neutralized with essentially unit probability when they penetrate the electron density of a solid by an amount deeper than a small fraction of an atom, the ions that survive scattering from the solid and get detected as LEIS signal probe only the topmost atomic layer of the solid.[101] We consider here systems where the adsorbate A is on a flat substrate surface S in the form of islands, and assume that the ions have a constant neutralization probability when they strike area that are material S and another, perhaps different neutralization probability when they strike areas covered by A islands.

We first consider the case where the adsorbate is in the form of single atom-thick 2D islands. In this case, the signal intensity for the LEIS peak for the adsorbate, I_A, is proportional to the fraction of the surface physically covered by islands of A, f_A:

$$I_A = f_A \, I_A^0, \qquad (3.1)$$

where I_A^0 is the signal when 100% of the surface is covered by a 2D layer of A. The substrate peak's intensity, I_S, is just:

$$I_S = (1-f_A) \, I_S^0, \qquad (3.2)$$

where I_S^0 is its signal when none of the surface is covered by A (i.e., from a clean S surface). Here we assume that since the islands are only one atom thick, any shadowing of uncovered substrate by the island edges is negligible at any angles of incident ions or detection. This is certainly true for large islands, but may fail when the islands are only a few atoms across.

When the adsorbate is in the form of uniform-size 3D hemispherical nanoparticles instead of single atom-thick 2D islands, the same analysis as above applies if the ions are both incident and detected normal to the surface. Thus, Eqs. (3.1) and (3.2) still apply, except that I_A^0 now refers instead to the signal when 100% of the surface is covered by 3D islands of A. This 100% coverage is impossible to realize experimentally while maintaining the shape of hemispherical caps, so I_A^0 is usually approximated experimentally when studying film growth as the signal when 100% of the surface is covered by a 3D layer of A. This is best measured after having added just enough A to the surface such that its 3D islands have grown together to mask all of the signal from S, which most closely approximates the same surface roughness factor of hemispherical caps. It is important to have the same roughness (i.e., the same distribution of local angles of the surface of A relative to the substrate surface normal) because the number of A surface atoms per unit projected area of A onto the planar substrate varies inversely with the cosine of the local angle of the surface of A relative to the substrate surface normal. Thus, the LEIS signal for A per unit projected area of A onto the planar substrate probably also depends on that local angle. Therefore, this rough surface of pure A with a very similar distribution of surface angles as for hemispherical caps is a better reference signal for estimating I_A^0 than a flat surface of bulk A. It is also often easier to achieve this experimentally than a flat surface of pure A on the same day as the nanoparticle measurements, unless one has the ability to mount a separate reference sample in the same analysis position. Unless the A atoms are quite mobile, this surface roughness persists or even gets worse as film thickness increases. If A does not like to wet the substrate, it can also get rougher and can even dewet upon annealing.

When the ions are incident or detected at some angle away from the substrate surface normal, the analysis is more complex, since the 3D hemispheres mask more of the solid than their actual footprint (or interfacial contact area on S). Consider first when ions are incident still normal to the surface but detected at some polar angle θ_d from normal, as shown in Fig. 2.1 for a particle of radius r. As shown, more of the surface is masked by the particle than its footprint area πr^2. The left side masked area is now half of an ellipse with semi-minor axis of length r and semi-major axis of length $b = r/\cos\theta_d$. Since the area of the full ellipse would be $\pi rb = \pi r^2/\cos\theta_d$, the masked area by one particle is now:

$$\text{Area per particle} = \pi r^2(1 + 1/\cos\theta_d)/2. \qquad (2.3)$$

If there is a number density of n such particles per unit area and their separations are large enough that their shadows do not overlap, the fraction of the substrate's area that is masked by the whole collection of particles of A is just:

$$f_A = n \text{ x Area per particle} = n\pi r^2(1 + 1/\cos\theta_d)/2. \qquad (3.4)$$

When the angle of detection is normal to the surface (0°) but the ions are incident at some angle θ_i from normal, one gets a nearly identical equation for the fraction masked by A:

$$f_A = n\pi r^2(1 + 1/\cos\theta_i)/2. \qquad (3.5)$$

Finally, when the ions are incident at some angle θ_i from normal and the angle of detection is at some angle θ_d from normal, and these two polar angle directions are separated by 180 ° in the azimuthal angle, the fraction of substrate S masked by A is:

$$f_A = n\pi r^2(1/\cos\theta_i + 1/\cos\theta_d)/2. \qquad (3.6)$$

It also has the proper limits when either θ_i or θ_d, or both, is decreased to zero (normal). It is still a pretty good approximation even when the azimuthal separation decreases to 90°. Using Eq. (3.6) for f_A allows one to still model the intensities of the adsorbate and substrate LEIS peaks using Eqs. (3.1) and (3.2), respectively. As noted above, I_A^0 must now refer to the signal when 100% of the surface is covered by a 3D islands of A, estimated experimentally as described above.

To understand why this I_A^0 is the appropriate reference signal for use when combining Eq. (3.1) with Eq. (3.6), it is useful to imagine the situation when the A particles are packed close enough together such that the areas masked by each particle just start to overlap, as shown schematically in Fig. 3.2. One must actually imagine this in more than one dimension, with the hypothetical situation where fraction of substrate S masked by A, $f_A = n\pi r^2(1/\cos\theta_i + 1/\cos\theta_d)/2$, just reaches 1.0. If the particles were packed any closer than this, no extra signal for A would be gained, since parts of each particle would then move into regions shadowed by its neighbors. We thus assume that the signal for A would remain the same with further increases in packing density right up to the limit where the 3D islands of A have grown together to mask all of the signal from substrate S, which we defined above as giving I_A^0 as its signal for A.

As noted above, Diebold et al.[21] introduced an identical model for analyzing these LEIS intensities for adsorbates in the form of hemispherical caps. They analyzed only the special case when the angle of detection is normal to the surface ($\theta_d = 0^o$) and the ions are incident at $\theta_i = 45^o$ from normal. For the fraction masked by A, they used that $f_A = 3n\pi r^2/2 = (1.5)n\pi r^2$. However, the true value for this geometry is $f_A = (1.207)n\pi r^2$, obtained using either Eq. (3.5) or (3.6). It is possible that they stated incorrectly that $\theta_i = 45^o$ in the paper, since $\theta_i = 60^o$ would give their result.

3.3 Experimental

To demonstrate how Eq. (3.6) is used, the growth of vapor-deposited Cu onto slightly reduced $CeO_2(111)$ was investigated using He^+ LEIS at 300K, as shown in Fig. 3.3(a). The

$CeO_{1.95}$(111) thin films were grown on Pt(111) as described previously[14] in an adjacent UHV preparation chamber that is connected to the calorimetry chamber through a gate valve. The Pt(111) surface was cleaned by successive cycles of 1 kV Ar^+ sputtering in $6x10^{-6}$ background Ar followed by annealing to 1173 K in UHV and then 873 K in $1x10^{-6}$ O_2 until no C was present in XPS and a sharp Pt(111) LEED pattern were observed. The $CeO_{1.95}$(111) films were grown via reactive evaporation of Ce in a $1x10^{-6}$ torr O_2 background and a sample temperature of 873 K with an average ceria deposition rate of 0.5 nm/min as determined from the attenuation of the Pt $4p_{3/2}$ photoelectron peak and the inelastic mean free path of $Pt4p_{3/2}$ electrons escaping through CeO_2 calculated using NIST inelastic mean free path database (1.75 nm). Ceria oxidation state was measured by XPS (see below) and sample order was verified by LEED. Further reduced $CeO_{1.9}$(111) and $CeO_{1.8}$(111) samples were grown using the same procedure except by reducing the oxygen pressure to $1x10^{-7}$ torr and tuning the resulting oxidation state by post annealing in $1x10^{-7}$ torr O_2 until the desired oxidation state was achieved (usually 0.5-1 min at 873 K).

The growth morphology of Cu on CeO_{2-x}(111) was determined using LEIS with a 135 degree scattering angle, $2x10^{-7}$ torr He background, and 3 mA emission current which gives an ion current ~90 nA/cm^2 averaged over the area that is rastered. The ions are incident 45° from surface normal at an energy of 1.5 keV and detected normal to the surface here. The integrated intensity of the Ce signal was normalized to the integrated Ce area with no Cu, and the Cu signal was normalized to a thick Cu overlayer that completely masked the substrate's Ce LEIS signal. When normalized in this way, the Cu signal is a direct measure of the fraction of the ceria surface masked by Cu particles and the Ce signal measures the fraction that is not masked.

3.4 Results

The Cu LEIS signal increases with Cu coverage and the Ce signal decreases for all Cu coverages, indicating Cu does not diffuse into the substrate, but rather forms a surface layer on $CeO_{1.95}(111)$. The data in Fig. 3.3(a) are compared to the layer-by-layer model and the hemispherical cap model. The data deviate markedly from layer-by-layer growth but are well fit using the hemispherical cap model described above. This number density is the only fitting parameter, since it alone determines the value of the particle diameter (D = 2r) at any given total Cu coverage. It was determined for the data in Fig. 3a from the best fit to Eqs. (3.1) and (3.2) (with Eq. (3.6) for f_A) to the data up to a coverage of 2.2 ML (above which the masked area of neighboring particles may start to overlap significantly and the model would fail). This best fit was generated using a least squares analysis. It gave a Cu 3D particle density of 7.8×10^{12} particles/cm^2.

Up to the fit coverage of 2.2 ML, the RMS error of the data relative to this fit is 0.021 (in the same units as the y-axis here). If we used this same number density with the original equation from Ref.[21], the RMS error increases to 0.069, ~3-fold larger.

The normalized LEIS signals in Fig. 3.3(a) directly provide the fraction of the ceria surface whose signal is masked by Cu particles, and the fraction of the total maximum Cu signal (due to complete coverage by Cu) that is observed at any given Cu coverage. If we assume the actual footprint of the Cu particles is expanded due to macroscopic shadowing by the same factor as is the case for hemispherical caps at this LEIS measurement geometry ($(1 + 1/\cos\theta_i)/2 = 1.207$, see Eq. (3.5) or (3.6)), we can divide these fractions by 1.207 to estimate the area fractions actually covered by Cu particles, and not just masked by them from ion trajectories. Since we know the average Cu film thickness from the Cu coverage (assuming the Cu particles have the density of bulk Cu(solid)), and we can divide it by this covered fraction for each LEIS data point (both Cu and Ce) to get the average particle thickness. Fig. 3.3(b) shows the average Cu particle thickness versus Cu coverage for both ceria films estimated in this way from each LEIS data point. Since the average thickness of a hemispherical cap is 1/3 its diameter, we have multiplied this thickness by 3 to show the corresponding average diameter along the right-hand axis here. For comparison, we show the result expected from the same hemispherical-cap model and particle number density as used for the best fit to the top part of Fig. 3.3(a). The agreement is excellent.

The hemispherical cap model was also introduced by Diebold et al.[21] for analyzing electron spectroscopy signals, where they derived equations for the intensities of peaks associated with substrate and adsorbate elements. It has been widely applied for analyzing signals in Xray photoelectron spectroscopy or Auger electron spectroscopy during film growth where 3D particles are formed. However, those equations only apply when the electron intensities have been measured for a take-off angle normal to the substrate surface. We recently presented an extension of that model that allows it to be applied at other angles of electron detection.[102] We have found that when electron spectroscopy is used together with LEIS to analyze film growth, it provides very powerful information on film morphology.[3,13,14,67]

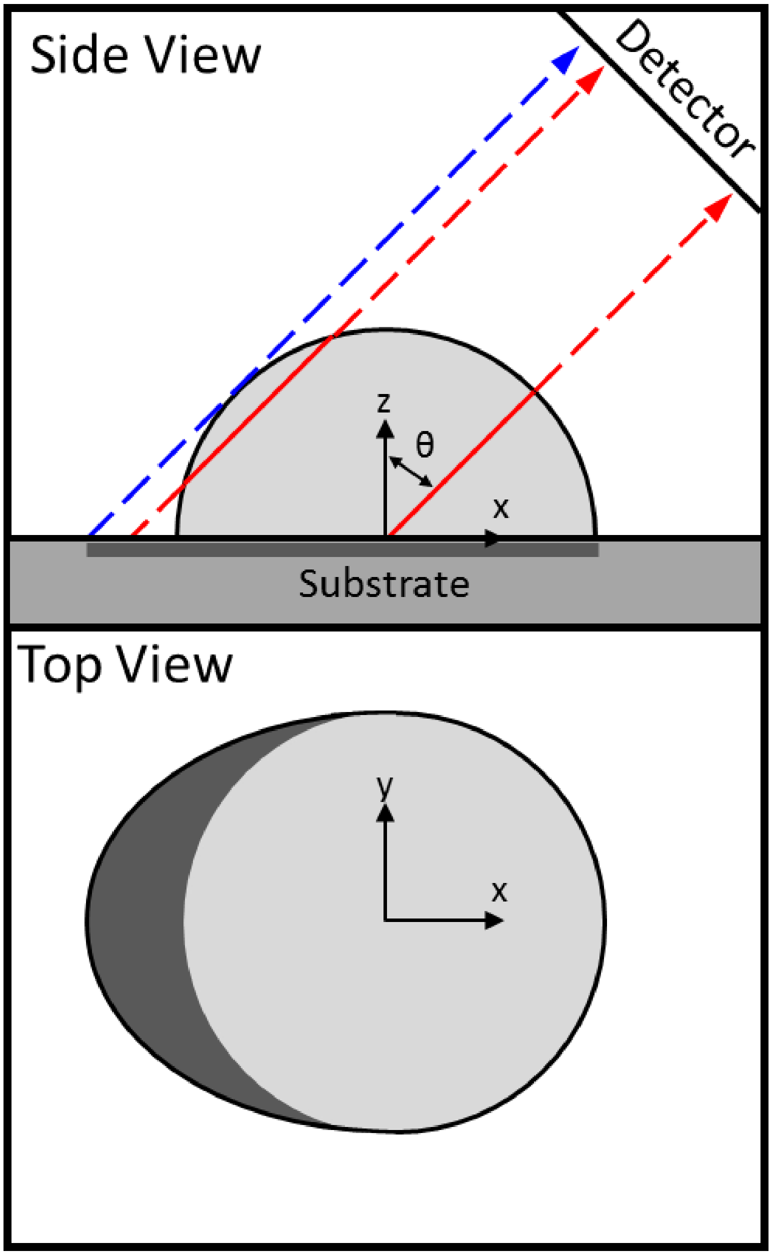

Figure 3.2: Schematic diagram of a hemispherical cap of adsorbate and the underlying substrate from both side and top views. The detector is at the angle shown but infinitely far away compared to the particle size. The y axis (not shown) is out of plane. Ions scattered from the substrate will be completely blocked from reaching the detector by the hemispherical cap if they originate from the shadow created by the cap (darker shaded area). The hashed area of the substrate therefore represents the effective spectroscopic footprint of the particle at this particular angle of detection (θ_d from normal to the substrate surface).

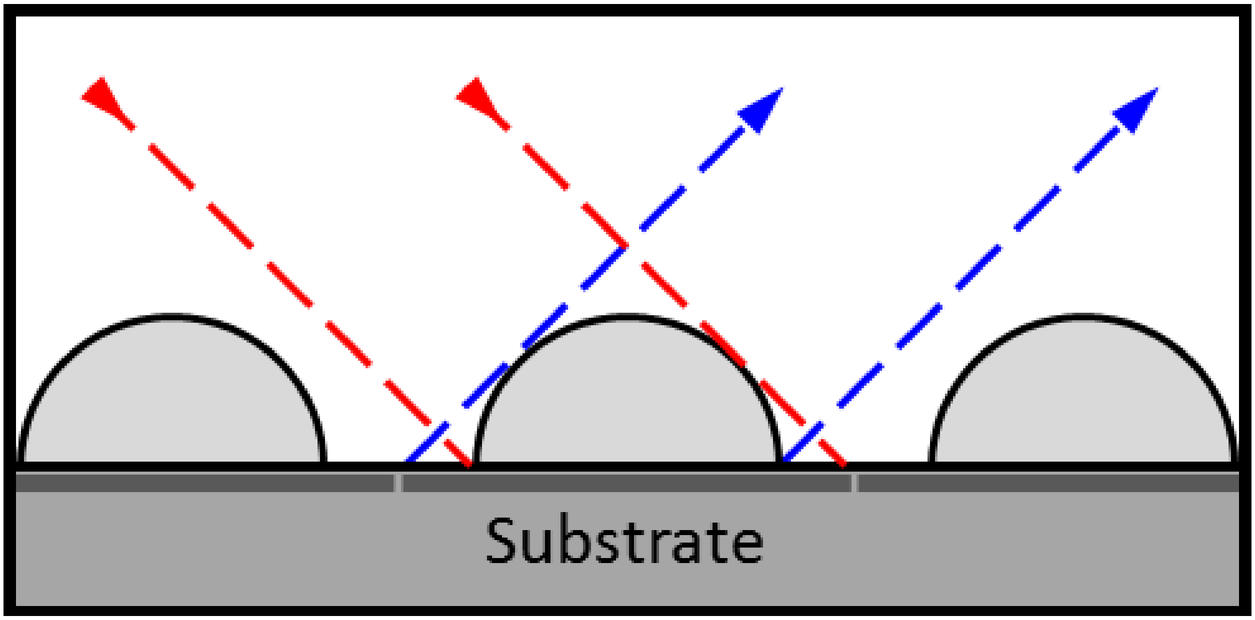

Figure 3.2: Schematic representation in one dimension of the hypothetical situation wherein hemispherical caps are packed together so closely (in both dimensions) that the fraction of substrate signal masked by A just reaches 1.0. The signal for A gets no larger at higher packing densities, even when A particles touch and cover 100% of the substrate.

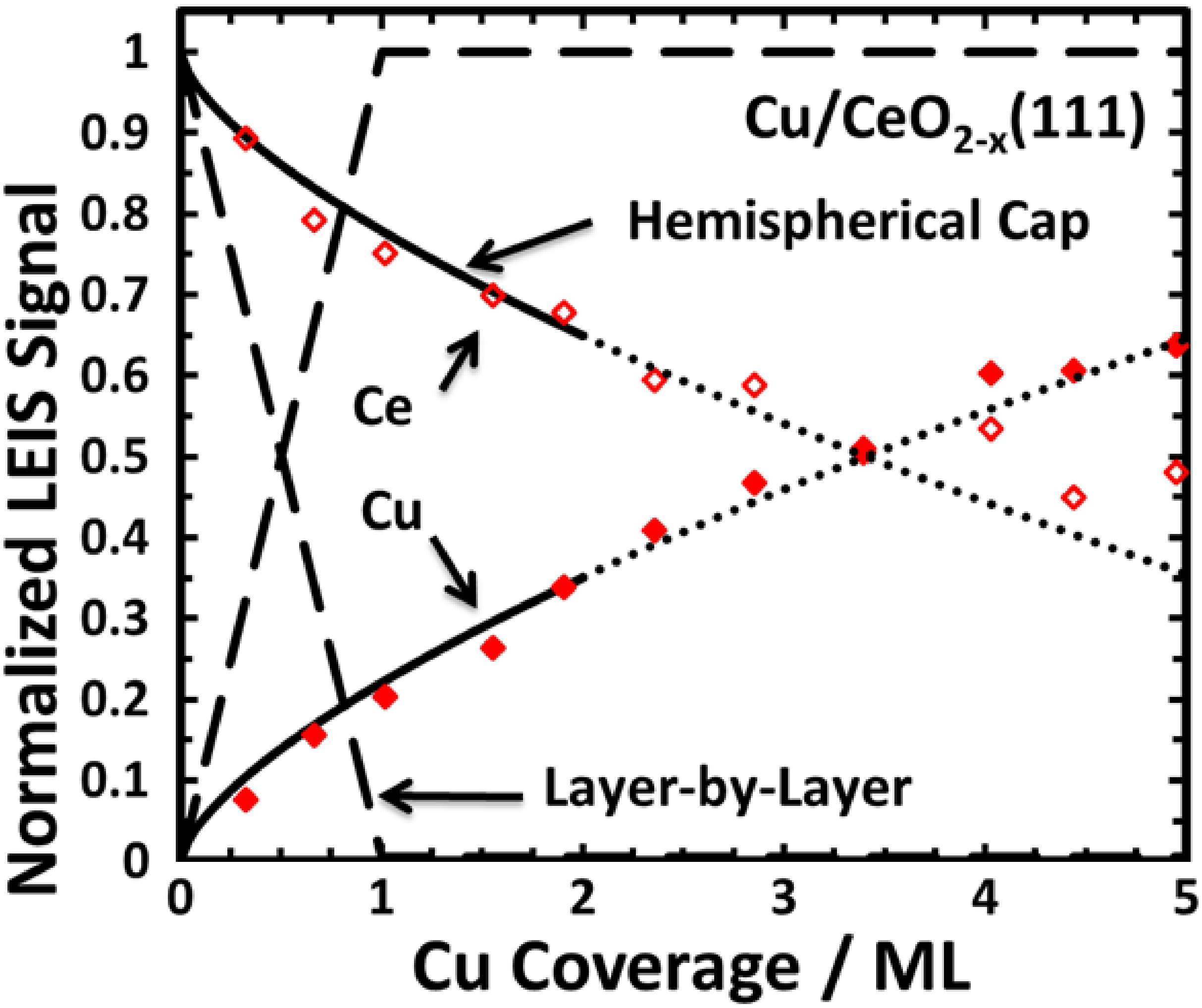

Figure 3.3(a): Integrated Cu (closed diamonds) and Ce (open diamonds) LEIS signal intensities (normalized to that from a thick Cu film and clean CeO$_{2-x}$(111), respectively) as a function of Cu coverage after deposition onto CeO$_{1.95}$(111) (diamonds) at 300 K. The He$^+$ ions are incident 45° from surface normal at an energy of 1.5 keV and detected normal to the surface. The dashed lines corresponds to the normalized LEIS signals that would be observed if Cu grew in a layer-by-layer fashion, while the solid lines corresponds to the best fit to the hemispherical cap model (Eq. (6)), whereby Cu grows as hemispherical caps with a fixed radius (at any given coverage) and a fixed particle density at all coverage of 7.8x10^{12} particles/cm^2. This model is only reasonable up to ~35% of the surface being covered by particles, since they may start to overlap with each other at higher coverage, so the dotted lines after that are only a guide to the eye.

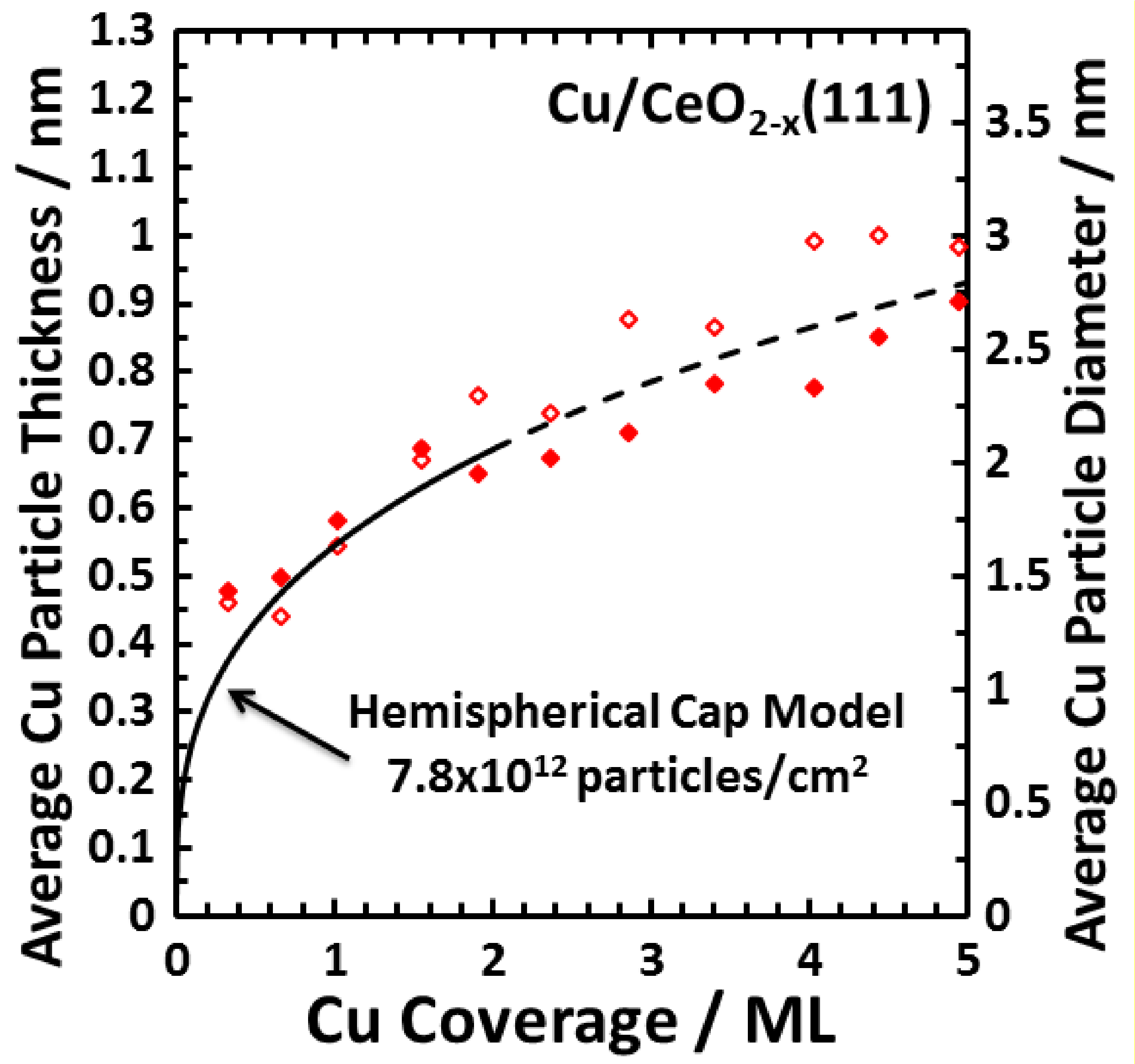

Figure 3.3(b): The average Cu particle thickness versus Cu coverage calculated from the Cu (closed) and Ce (open) LEIS data points of Fig. 3(a), and on the right axis, the average diameter of hemispherical caps that corresponds to this thickness. Also shown is the result expected for the same hemispherical-cap model and particle number density as used for the best fit to the data in part (a).

Chapter 4

Energetics of Cu Adsorption and Adhesion onto Reduced CeO_2(111) Surfaces by Calorimetry

This Chapter has been published as:

T.E. James, S.L. Hemmingson, T. Ito, C.T. Campbell,

J. Phys. Chem. C, 2015, 119, 17209-17217

The morphology and interfacial energetics of vapor-deposited Cu on slightly-reduced CeO_2(111) surfaces at 300 K have been studied using single crystal adsorption calorimetry (SCAC), He^+ low-energy ion scattering spectroscopy (LEIS), X-ray photoelectron spectroscopy (XPS), and low energy electron diffraction (LEED). Copper grows as 3-dimensional nanoparticles with a density of ~10^{13} particles/cm^2 on CeO_{2-x}(111) (x = 0.05, 0.1 and 0.2). The initial heat of adsorption of Cu decreased with the extent of reduction, showing that stoichiometric ceria adsorbs Cu more strongly than oxygen vacancies. On $CeO_{1.95}$(111), the heat dropped quickly with coverage in the first 0.1 ML, attributed to nucleation of Cu clusters on stoichiometric steps, followed by the Cu particles spreading onto less favorable sites (step vacancies and terraces)r. Above ~0.1 ML (>0.8 nm in diameter), the Cu adsorption energies showed no variation with extent of ceria reduction: the heat of adsorption increased slowly with coverage (particle size) due to the formation of more Cu-Cu bonds per adatom as the size grows, finally approaching the heat of sublimation of bulk Cu by 3.5 ML (2.5 nm). The adhesion energy of Cu(solid) to $CeO_{1.95}$(111) was found to be 3.52 J/m^2 for 2.2 nm diameter particles, decreasing slightly with extent of reduction. The Ce 3d XPS lineshape showed an increase in Ce^{3+}/Ce^{4+} ratio with Cu coverage, corresponding to donation of at most ~0.17 and 0.06 electrons per Cu atom to $CeO_{1.95}$(111) and $CeO_{1.8}$(111), respectively.

4.1 Introduction

Heterogeneous catalysts are generally composed of late transition metal nanoparticles dispersed over high surface area oxide supports. The interaction of the supported metal and underlying oxide can greatly influence catalytic properties such as long term sinter resistance, activity, and selectivity. To improve our understanding of how the choice of metal and support can influence catalytic properties, detailed studies of model systems, where metal atoms are vapor deposited onto single crystal oxide supports, are often employed. With these model systems, the structure of the support surface, the size of the metal particles, and surface cleanliness can be better controlled[6,7,20,22,103] Studies of this type provide the basic understanding necessary for the intelligent design of new, more efficient, and greener catalysts. Here we apply that approach to study model Cu/CeO_2 catalysts consisting of Cu nanoparticles grown by vapor deposition on CeO_2(111) surfaces with controlled extents of reduction.

We study the energies of the Cu atoms in this system using single crystal adsorption calorimetry (SCAC). This method directly measures the adsorption energy of the incoming metal atoms as they bind to the oxide surface, and to metal nanoparticles on that surface as they grow in size.[10,12-14,104,105] The Cu nanoparticle morphology is characterized using ion scattering spectroscopy (LEIS), and X-ray photoelectron spectroscopy (XPS). Adsorption energies measured using SCAC along with detailed adsorbate structural studies have also been used to determine metal adhesion energies to various single crystal oxide surfaces,[10,12,13,105] which we also do here. This is important since differences in the metal's adhesion energy affect the sintering rates of these metal/support systems: the larger a metal's adhesion energy is to the support, the more resistant the metal is to sintering.[10] We also use XPS to determine the electronic properties of both supported Cu nanoparticles and the reduced CeO_2(111) surfaces.

The results presented here help clarify the nature and strength of binding at the Cu nanoparticle / ceria interface, how it depends on the extent of ceria reduction, and how interfacial bond strengths in general are influenced by the choice of metal and support. The results are compared to similar measurements of Cu adsorption on MgO(100)[12] and Ag adsorption on the same reduced $CeO_2(111)$ surfaces.[10,14]

Copper supported on ceria has shown promise as a catalysts for a variety of reactions such as CO oxidation,[27,28] water gas shift reaction,[29,30] and methanol synthesis.[31,32] For methanol synthesis, the perimeter of copper nanoparticles at the interface with ceria were found to be the most catalytically active sites,[32] and Cu was only catalytically active when it is in the neutral form rather than oxidized.[31] However, few detailed structural studies exist for copper/ceria catalysts. One study by Matolin et al.[2] of vapor-deposited Cu on $CeO_2(111)$ showed that the oxidation state of Ce before Cu adsorption influenced the electronic structure of Cu nanoparticles, with oxygen vacancies donating electron density to Cu and stoichiometric sites withdrawing electron density from Cu.[2] However, little was known about the strength of interfacial bonding and the structure of the adsorbed Cu in this system until this present report. To our knowledge, the only other detailed structure/energetic study of metal adsorption onto $CeO_2(111)$ is our earlier report of Ag adsorption.[10,14]

4.2 Results

4.2.1 $CeO_{2-x}(111)$ thin film characterization.

$CeO_{2-x}(111)$ thin films were grown in a separate preparation chamber on a 1 micron thick Pt(111) substrate to a thickness of 4 nm as described in Chapter 2. Our previous results for Ag adsorption on $CeO_{2-x}(111)$ thin films showed that thicknesses of 2, 3 and 4 nm gave the same results in terms of heats of Ag adsorption versus coverage, while 1 nm thick films showed a different behavior.[14] Thus, the 4 nm thickness used here is certainly expected to give bulk-like ceria surface properties. Ceria film thickness was determined by measuring the attenuation of the Pt $4p_{3/2}$ XPS peak from the clean Pt(111) substrate using the inelastic mean free path of Pt photoelectrons escaping through ceria, 1.75 nm. LEED images of the as grown CeO_{2-x}(111) thin films gave sharp (1.4x1.4) patterns (not shown) as reported previously,[14] indicating the surface was well ordered. No Pt(111) LEED spots were visible for the 4 nm ceria films, but the (1.4x1.4) pattern and epitaxial relationship were confirmed by performing LEED on thinner ceria films (0.5-1 nm) indicating an epitaxial relationship to the underlying substrate.

Figure 4.1 shows representative Ce 3d XPS for the three CeO_{2-x}(111) oxidation states studied here (where x = 0.05, 0.1 and 0.2). For $CeO_{1.8}$(111), a sample Shirley background and 10-peak decomposition (4 for Ce^{3+} and 6 for Ce^{4+}) are shown. The peak positions and relative sizes of Ce^{3+} and Ce^{4+} peaks were taken from reference spectra reported for bulk Ce_2O_3 and CeO_2.[106] The CeO_{2-x} (111) film stoichiometry was determined by measuring the Ce^{3+} concentration in the Ce 3d XPS feature compared to the total integrated Ce 3d area ($Ce^{3+}/[Ce^{3+}+Ce^{4+}]$). Reduced $CeO_{1.8}$(111) films grown on Pt(111) have usually been prepared by high temperature annealing in UHV.[14,107] However, no change in oxidation state was observed when our as prepared films were annealed, but instead an increase in the Pt $4p_{3/2}$ XPS peak was observed when heated hot enough to see a significant change in the spectra beyond a reduction to $CeO_{1.92}$. Thus, either the as-grown ceria film dewetted from the Pt(111) surface to make thicker 3D particles upon annealing in UHV, or any Ce that was reduced subsequently disappeared into the Pt(111) bulk. We therefore prepared our reduced ceria films ($CeO_{1.9}$(111) and $CeO_{1.8}$(111)) instead by growth in a lower oxygen pressure than usual ($1x10^{-7}$ torr), which gives an approximate initial oxidation state of $CeO_{1.6}$. Annealing for 0.5 to 1 minutes at 873 K and $1x10^{-7}$

torr O_2 oxidized the ceria film to $CeO_{1.8}$(111) and $CeO_{1.9}$(111) respectively. The calculated oxidation state is the same when measuring at emission angles of 45 and 90 degrees indicating the oxidation state on the surface is the same within the probe depth of XPS. Unfortunately STM was not available to verify the defect density of the as-prepared CeO_{2-x}(111) films, however, Valeri et al.[107] have shown that similar annealing of reduced CeO_2(111) films grown on Pt(111) in oxygen for short periods does not create additional step or kink sites compared to the original film. It is likely no additional steps or kinks were introduced in the ceria films studies here by annealing in oxygen. Also, previous CeO_{2-x}(111) films grown on Pt(111) by Farmer et al.[14] using very similar preparation methods have been estimated to have a total surface defect density of 5-6% using STM. It is therefore estimated the defect density is the same on the films studied here. For a detailed analysis on the surface defect structure see Ref.[14].

4.2.2 Cu sticking probability on CeO_{2-x}(111).

The sticking probability of Cu on CeO_{2-x}(111) was measured as the number of non-sticking Cu atoms in each pulse determined by the magnitude of the time-integrated transient QMS signal compared to the signal of a reference pulse from a hot Ta flag where no sticking occurred. At all Cu coverages, the sticking probability was >0.99 for all three CeO_{2-x}(111) films.

4.2.3 Cu morphology on CeO_{2-x}(111).

The growth morphology of Cu on CeO_{2-x}(111) was investigated using He^+ LEIS at 300K and shown in Fig. 4.2(a). Discreet amounts of Cu were deposited using the same series of apertures and dose rates as the calorimetry experiments. The integrated intensity of the Ce signal was normalized to the integrated Ce area with no Cu, and the Cu signal was normalized to a thick, bulk like Cu overlayer (>40 ML). When normalized in this way, the Cu signal is a direct measure of the fraction of the ceria surface masked by Cu particles and the Ce signal measures the fraction that is not masked. The Cu LEIS signal increases with Cu coverage and the Ce signal decreases for all Cu coverages, indicating Cu does not diffuse into the substrate, but rather forms a surface layer on $CeO_{2-x}(111)$. The data in Fig. 2(a) are compared to two mathematical growth models, the layer-by-layer and hemispherical cap models. The data deviate markedly from the layer-by-layer model, indicating that Cu growth is not two-dimensional in the first layer. The data are well fit using the hemispherical cap model described by Diebold et al.,[21] but modified to better describe macroscopic shadowing of the incident ion beam by hemispherical particles.[108] It assumes that the film grows as 3D particles with the shape of hemispherical caps, with a fixed number density of particles, n, at all metal coverages, and that all particles have the same average diameter, D, at any one coverage. When the angle of detection is normal to the surface but the ions are incident at angle $\theta_i = 45°$ from normal as here, that model gives that the fraction of the ceria substrate signal masked by Cu particles equals $n\theta D^2(1 + 1/\cos\theta_i)/8$.[108] The number density is the only fitting parameter since it alone determines the value of D at any given total Cu coverage. It was determined for the data in Fig. 4.2 from the best fit line, which was generated using a least squares analysis and gave a Cu 3D particle density of $7.8\mathrm{x}10^{12}$ particles/cm^2 on both $CeO_{1.95}(111)$ and $CeO_{1.8}(111)$. The data were fit only up to 35% total surface coverage by Cu (2.2 ML Cu), since particles start to have too high a probability to overlap and even coalescence at higher coverages, which would invalidate the assumptions of the hemispherical cap model. No LEIS growth mode data were collected for $CeO_{1.9}(111)$, which we assumed to have a similar particle density as seen at the higher and lower oxidation states. The hemispherical cap model has been shown to be a good model for many late transition metals supported on oxides of the type used as catalyst supports,[9] and most late transition metals have been shown to grow as 3-dimensional particles on these oxides.[7]

To ensure there was no sample damage due to He^+ ion bombardment during the course of the experiments in Fig. 4.2(a), a control experiment was run using only two coverages (~1 and 4 ML), so that much less total ion beam exposure was used to get to each data point. The data from the two-point experiment (not shown) fell within error of the best-fit lines for each sample in Fig. 2(a), indicating that sputter damage from the low dose of He^+ ions did not significantly influence the data in Fig. 4.2(a).

The normalized LEIS signals in Fig. 4.2(a) directly provide the fraction of the ceria surface whose signal is masked by Cu particles, and the fraction of the total maximum Cu signal (due to complete coverage by Cu) that is observed at any given Cu coverage. If we assume the actual footprint of the Cu particles is expanded due to macroscopic shadowing by the same factor as is the case for hemispherical caps at this LEIS measurement geometry ($(1 + 1/\cos\theta_i)/2 = 1.207$, see above), we can divide these fractions by 1.207 to estimate the area fractions actually covered by Cu particles, and not just masked (shadowed) by them from ion trajectories. Since we know the average Cu film thickness from the Cu coverage (assuming the Cu particles have the density of bulk Cu(solid)), we can divide it by this covered fraction for each LEIS data point (both Cu and Ce) to get the average particle thickness. Fig. 4.2(b) shows the average Cu particle thickness versus Cu coverage for both ceria films estimated in this way from each LEIS data point. Since the average thickness of a hemispherical cap is 1/3 its diameter, we have multiplied this thickness by 3 to show the corresponding average diameter along the right-hand axis here. For comparison, we show the result expected from the same hemispherical-cap model and particle number density as used for the best fit to the top part of Fig. 4.2(a). The agreement is excellent.

In Fig. 4.2(a), the Cu LEIS signal is slightly lower on the more reduced surface above 2 ML. We do not interpret the data at these high coverages using the hemispherical cap model, where its assumptions break down due to particles overlapping. This difference is probably due to the fact that Cu binds more weakly to the parts of the surface containing oxygen vacancies (see below), and so it avoids areas with vacancies on terraces as more of the ceria is covered by Cu. This could result in Cu covering slightly less of the more reduced surface.

The growth morphology of Cu on $CeO_{1.95}(111)$ was also studied using XPS as shown in Fig. 4.3. The integrated signal intensities of Cu $2p_{3/2}$ and Ce 3d XPS regions, normalized using the same method as the LEIS signals above, are plotted versus Cu coverage. The Cu data were fit using the literature electron mean free path at a kinetic energy of 554 eV (1.09 nm[109]). The data were again well fit by the hemispherical cap model as derived for electron spectroscopies[102] with the same particle density as used to fit the LEIS data (7.8×10^{12} particles/cm^2). Diebold et al.[21] have shown mean free paths of electrons escaping from an ordered substrate is smaller than literature mean free paths due to forward focused electrons on the uncovered substrate that become attenuated by an overlayer due to blocking of the forward focused paths or distortion of the substrate lattice. We therefore used the calculated particle density from Cu XPS and LEIS to determine the mean free path of Ce 3d electrons. The best fit mean free path shown in Fig. 4.3 was found to be 0.9 nm for Ce electrons escaping through a Cu overlayer, which is slightly shorter than the literature value of 1.14 nm[109] for these 580 eV electrons through Cu.

4.2.4 Heat of Adsorption and Adhesion Energy of Cu on $CeO_{2-x}(111)$.

Figure 4.4 shows the heat of adsorption of Cu on $CeO_{2-x}(111)$ (where x = 0.05, 0.1, and 0.2) as a function of Cu coverage at 300 K. All heats of adsorption reported here have been corrected slightly for the hot temperature and directed nature of the Cu atomic beam, so that they correspond to Cu atoms in a Boltzmann distribution at the surface temperature, and RT has been subtracted from the measured energies, as we always do in calorimetry. (Directionally dosed gas atoms have a ½ RT higher average translational energy than a Boltzmann distribution of gas atoms at the source temperature, T).[17] This is done so that the values on plots like Fig. 4 correspond to the standard enthalpy of adsorption at the sample temperature (times -1). On $CeO_{1.95}(111)$, Cu adsorbs with an initial heat of adsorption of 300 kJ/mol and drops quickly to 283 kJ/mol by 0.1 ML. The heat then increases slowly, levelling off very near to the heat of sublimation of bulk Cu(solid), 337 kJ/mol,[78] by 3.5 ML. This indicates that, at and above this coverage, incoming Cu atoms bond with the same average strength as they would to a bulk Cu surface. Increasing the degree of reduction to $CeO_{1.9}(111)$ and $CeO_{1.8}(111)$, decreases the initial heat of adsorption to 272 and 257 kJ/mol, respectively. There was no drop in the initial heat of adsorption with coverage for $CeO_{1.9}(111)$ or $CeO_{1.8}(111)$ as was observed for a small coverage range on $CeO_{1.95}(111)$. Instead, the heats on both rose slowly to the Cu heat of sublimation by 3.5 ML. The heat of adsorption versus coverage for all three oxidation states is identical (within the scatter of the data) above 0.1 ML.

Using the Cu particle number density from the hemispherical cap model fit to Fig. 4.2(a), which also gives the average Cu particle diameter at each coverage, the data in Fig. 4.4 can be replotted as Cu heat of adsorption vs average Cu particle diameter, as shown in Fig. 4.5. The $CeO_{2-x}(111)$ oxidation state only has an influence on the heat of adsorption for Cu nanoparticles below 0.8 nm in diameter. Above 0.8 nm, there is no influence from the cerium oxidation state on the heat of adsorption of Cu at any coverage. Instead, the heat increases slowly with particle size to asymptotically reach the heat of bulk Cu sublimation (within error) by 2.2 nm diameter.

The adhesion energy of nanoparticles to the surface upon which they are grown, E_{adhesion}, can be calculated from the integral heat of adsorption and growth mode data using a simple thermodynamic cycle described in Ref.[9], which gives the following energy balance:

$$n\cdot\sum_n \Delta H_{\mathrm{adsorption}} = -n\cdot\Delta H_{\mathrm{sublimation}} + A\cdot[(1+f)\gamma_{\mathrm{v/m}} - E_{\mathrm{adhesion}}],$$

where $\gamma_{\mathrm{v/m}}$ is the surface free energy of the nanoparticle material, f is the surface roughness factor (for a hemispherical cap, f =2), $\sum_n \Delta H_{\mathrm{adsorption}}$ is the integral (average) molar heat of adsorption up to the coverage (particle size) of interest, n is the number of moles of the adsorbate on the surface at that coverage, A is the total area covered by the metal nanoparticles and $\Delta H_{\mathrm{sublimation}}$ is the molar heat of sublimation of the adsorbate. The adhesion energy is calculated when only <35% of the ceria surface is covered by Cu particles (according to LEIS), to ensure no significant particle agglomeration is occurring. This corresponds to a Cu coverage of 2.2 ML, or an average particle diameter of 2.2 nm. The adhesion energy for 2.2 nm diameter Cu nanoparticles supported on $CeO_{2-x}(111)$, where x = 1.95, was found by this equation and the data in Fig. 4 to be 3.52 J/m^2. This value decreased slightly for x = 1.9 and 1.8 to 3.45 and 3.43 J/m^2, respectively, due to the lower adsorption energies in the first 0.1 ML on these more reduced surfaces (Fig. 4). This adhesion energy of Cu to $CeO_{2-x}(111)$ is higher than the adhesion of 3.6 nm diameter Ag particles to the same surfaces, which was determined to be 2.3 J/m^2. This is as expected from Ref.[38], which shows that Cu bonds more strongly to cerium oxide surfaces than Ag. Cu adhesion to $CeO_{2-x}(111)$ is also stronger than Cu's adhesion to MgO(100), which was determined to be 1.9 J/m^2,[12] consistent with the trend previously reported of ceria bonding Ag more strongly than MgO(100).[10]

4.2.5 Oxidation state of Cu and Ce during Cu deposition onto $CeO_{2-x}(111)$.

The change in oxidation state of $CeO_{1.95}(111)$ and $CeO_{1.8}(111)$ films as a function of Cu coverage was monitored using XPS of the Ce 3d XPS regions. The corresponding changes in the Cu 2p XPS and Cu X-ray-excited AES peaks at a detection angle of 45º were also monitored to determine the charge state of Cu. For the Ce 3d region the same ten-peak fit described in Fig. 1 was used to calculate the Ce^{3+} concentration at various Cu coverages, as displayed in Fig. 4.6. The 4 nm thick films that were initially $CeO_{1.95}(111)$ and $CeO_{1.8}(111)$ become more reduced upon Cu deposition, with $CeO_{1.95}(111)$ having a greater extent of reduction per unit of Cu coverage than $CeO_{1.8}(111)$. The surfaces continue to reduce until 4 ML of Cu has been deposited. No further reduction was observed as thicker Cu overlayers were deposited, but no data points were taken between 4 ML and a very thick overlayer (~20 ML of Cu). Matolin et al.[2] similarly observed using XPS and resonant photoelectron spectroscopy (RPES) that fully oxidized $CeO_2(111)$ was reduced with increasing Cu coverage, and found that partially reduced ceria was initially oxidized for tiny Cu coverages but then get slightly more reduced as more Cu is added. We have added their results, which cover very low coverages in much more detail, to Fig. 4.6.

In the Cu 2p XPS region, no Cu^{2+}-like shoulders or satellite peaks at higher binding energies on either of the 2p doublets were observed at any Cu coverage, indicating that no Cu^{2+} was present within the detection limits of the analyzer at all Cu coverages, consistent with the results of Matolin et al.[2] The Cu $2p_{3/2}$ BE decreased slightly with Cu coverage up to 4 ML Cu, and stayed pretty constant after that, with a high-coverage (large-particle) saturation value of 932.67 eV. This agrees with literature values for bulk Cu(solid).[110] At only ~1.2 ML coverage, where the Cu particles are 1.8 nm in diameter, the Cu $2p_{3/2}$ BE was higher than this bulk value by only 0.25 eV on $CeO_{1.95}(111)$ and 0.15 eV on $CeO_{1.8}(111)$. Since the Cu and Cu^+ spectra have a similar lineshape and binding energy in the 2p region, the Auger parameter is often used instead to differentiate neutral Cu from Cu^+.[111] The Auger parameter for Cu is defined as the sum of the binding energy of the Cu $2p_{3/2}$ peak and the kinetic energy of the Cu (LMM) AES peak. Literature values for Cu^+ from Ref.[110] and Cu^0 (as bulk Cu(solid)) are 1849.4 and 1851.3 eV, respectively. The Auger parameter for Cu increases from 1850.6 eV for 1.2 ML Cu (1.8 nm diameter) to 1851.3 eV for 4.0 ML Cu (2.7 nm diameter) on $CeO_{1.95}(111)$ and from 1850.2 for 1.2 ML Cu (1.8 nm diameter) to 1851.3 eV for 3.7 ML Cu (2.6 nm diameter) on $CeO_{1.8}(111)$. After ~4 ML, the Auger parameter stays constant at 1851.3 eV up to 20 ML Cu coverage for both initial ceria oxidation states.

4.3 Discussion

Late transition metals usually nucleate particles at step edges when vapor deposited on oxides that are used for catalyst supports.[7] To our knowledge there are no microscopy images available for Cu on $CeO_{2-x}(111)$. However, Cu particles were observed to nucleate at steps on $TiO_2(110)$,[112] and $Al_2O_3(110)$.[113] Both Ag and Au have been observed to nucleate particles mainly on step edges during vapor deposition onto $CeO_{2-x}(111)$, for x in the range from 1.91 to 2 for Ag,[114] and from "partially reduced" to x = 2 for Au.[115] We therefore propose that the Cu particles here nucleate mainly at step edges for all three extents of reduction. Since the $CeO_{1.8}$ surface is missing about 10% of its oxygens and these oxygen vacancies preferentially populate step edges, and since our surfaces have ~5 % step sites,[14] the step edges on the $CeO_{1.8}$ surface are probably missing almost all of their oxygen atoms. On the other hand, the $CeO_{1.95}$ surface is missing only 2.5% of its oxygens, so the steps on $CeO_{1.95}$ must have about half their oxygens still present (i.e., half stoichiometric step sites). We show below that stoichiometric sites bind Cu more strongly than vacancy sites. Nevertheless, we proposed that this preference for step edges over terraces is probably true even on the fully reduced step edges of $CeO_{1.8}$, since the saturation particle density is the same as for $CeO_{1.95}$. It originates as usual from the strong binding of metal adatoms to the coordinatively less saturated substrate atoms at the step edges, both O and Ce (but more strongly to O than Ce, see below).

The 42 kJ/mol decrease in the initial Cu heat of adsorption with the extent of reduction of $CeO_{2-x}(111)$ (Fig. 4.4) is opposite to the previous observation for Ag adsorption on $CeO_{2-x}(111)$, where Ag initially binds 25 kJ/mol more strongly to $CeO_{1.8}(111)$ than to $CeO_{1.9}(111)$.[14] This suggests that Cu binds more strongly to stoichiometric ceria sites than to oxygen vacancies, whereas Ag binds to oxygen vacancies more strongly than to stoichiometric sites. This marked contrast between Cu and Ag is qualitatively consistent with DFT results. Fabris et al.[116] and Hermansson et al.[35] predicted with DFT that Cu binds more strongly to stoichiometric sites than to oxygen vacancies on $CeO_2(111)$ terraces, by 1.4 eV and 1.2 eV (135 kJ/mol and 116 kJ/mol), respectively; whereas Pacchioni et al.[117] predicted with DFT that Ag binds more weakly to stoichiometric sites than to oxygen vacancies on $CeO_2(111)$ terraces. Similarly, DFT indicates that Au,[118-120] Pt,[121] and Pd[122] bind more weakly to stoichiometric sites than to oxygen vacancies on $CeO_2(111)$ terraces.

Our measured initial heats of Cu adsorption onto $CeO_{2-x}(111)$ have a much smaller decrease between $CeO_{1.95}(111)$ and $CeO_{1.8}(111)$ (42 kJ/mol) than the ~1.3 eV (~125 kJ/mol) difference between vacancy sites and stoichiometric sites on terraces predicted by DFT highlighted above. However, one does not expect the full difference in adsorption energy for monomers to be seen in those measurements, since the 0.44 nm diameter Cu particles that are made in the first data point will prefer to avoid oxygen vacancy sites to the extent possible.

However, we propose that these Cu particles are located at step edges, which is also where the oxygen vacancies mainly reside, so it is not entirely possible to avoid oxygen vacancies on the two more reduced surfaces. Differences compared to the DFT adsorption energies are also expected due to the strong role of steps here, which were not considered in those DFT calculations.

We propose the following to explain the initial decrease in heat of Cu adsorption with coverage on the least reduced surface. The Cu clusters initially nucleate on the most stable sites for Cu, stoichiometric step sites. As more Cu atoms add to the Cu particles and their diameter grows, their footprint on the surface also grows, and the Cu atoms at the interface must occupy less favorable ceria sites (terrace sites and step vacancies). The resulting strong decrease in bonding energy of Cu atoms to the support apparently exceeds the expected increase in adsorption energy with coverage due to the formation of more Cu-Cu bonds per adatom as particle size grows, which is usually observed for late transition metal adsorption on oxides.[12-14] By ~0.1 ML (0.8 nm diameter), the latter effect starts to dominate, and so the heat increases with further Cu adsorption. These very stable stoichiometric step sites are not available in high enough concentration on the two more reduced surfaces to see the highest initial heat of adsorption due to nuclei mainly on such stable sites, and so the minimum in heat versus coverage is also not seen. Isolated oxygen vacancies on terraces are also potential nucleation sites for metal nucleation. However, since DFT predicts that the heat of adsorption of Cu atoms is much weaker on oxygen vacancies on $CeO_2(111)$ terraces compared to stoichiometric terrace sites,[35,116] nucleation at vacancies is certainly not expected.

The saturation Cu particle density remained constant when the degree of $CeO_{2-x}(111)$ reduction was increased from x = 1.95 to x = 1.8. This is consistent with the step density being the same on these surfaces (as expected[107]), with particle nucleation only occurring at step edges (including their kink sites). It is somewhat surprising that the density of particles per unit step length remains the same. This may be due to particle-particle repulsion along step edges. We propose that such repulsion is apparent in STM images of Ag and Au particles on $CeO_2(111)$, where the particle-particle separations along step edges are far more uniform than expected for randomly-located particles.[114,115] Such repulsion could result from the adsorbed particles inducing strain in the ceria lattice or having dipole moments perpendicular to the surface.

According to DFT, Cu adsorption to oxygen vacancies on $CeO_2(111)$ terraces causes transfer of electron density from Ce^{3+} to Cu, forming a partial negative charge on Cu and the oxidation of Ce^{3+} toward Ce^{4+}, whereas Cu on stoichiometric terrace sites does the opposite, transferring electron density from Cu to Ce^{4+}, reducing it toward Ce^{3+}.[35,116] At 1.2 ML in Fig. 4.6, the Cu particles cover ~20% of the surface (Fig. 4.2(a)). At this fractional coverage by Cu particles, they must bind both to step edges (which cover ~5% of the surface and are dominated by oxygen vacancies) and to stoichiometric terrace sites, with possibly some binding to terrace vacancies as well. Thus, according to DFT, the ceria oxidation state shift in Fig. 4.6 should be a competition between two opposing effects, ceria oxidation by Cu at oxygen vacancies and Ce reduction by Cu at stoichiometric sites. The competing interactions explain the smaller overall reduction of ceria observed for $CeO_{1.8}$ compared to $CeO_{1.95}$ where fewer oxygen vacancies are available initially (Fig. 4.6).

To quantify the extent of charge transfer per Cu atom in Fig. 4.6, we assume that the Ce XPS signal probes a depth of ~1.0 nm (see above), which corresponds to 2.5×10^{15} Ce atoms per cm^2 being probed at the bulk density of CeO_2 (2.52×10^{22} Ce atoms cm^{-3}). The slope of the lines here corresponds to the number of electrons gained per Ce atom in this probe depth per Cu ML, where 1 ML is $7.9x10^{14}$ Cu atoms per cm^2. These slopes thus correspond to 0.17 and 0.13 electrons donated per Cu atom for 1.2 ML and 4 ML Cu, respectively, on $CeO_{1.95}(111)$, and 0.060 and 0.053 electrons donated per Cu atom for 1.2 ML and 3.7 ML Cu, respectively, on $CeO_{1.8}(111)$. This apparent extent of charge transfer per Cu atom is less than half as much on $CeO_{1.8}$ compared to $CeO_{1.95}$, due to this competition between Ce reduction by Cu at stoichiometric sites and ceria oxidation by Cu at oxygen vacancies. The charge transfer measured here is averaged over the whole surface. It is probable that different sites (step edges, oxygen vacancies, and terraces) exhibit different extents of charge transfer, but those differences could not be measured here.

The apparent reduction of $CeO_{2-x}(111)$ in Fig. 4.6 may be partly because Cu adsorbs primarily to the stronger-binding stoichiometric sites compared to vacancy sites, which would preferentially attenuate the Ce^{4+} XPS signal, causing an apparent decrease in Ce oxidation state. The mobility of surface oxygens in the top layer may even be sufficient to allow them to move under the Cu particles and displace vacancies toward the uncovered parts of the surface. This selective Ce^{4+} signal blocking offers an additional contribution to understanding Fig. 4.6, but means that its quantitative interpretation in terms of electrons transferred per Cu atom is an overestimate. It is also consistent with the lower apparent extent of reduction of ceria on the more reduced surface, since that surface has fewer stoichiometric sites whose Ce^{4+} signal can preferentially be blocked by Cu.

The different shifts of Cu $2p_{3/2}$ BEs and Cu Auger parameters for Cu on $CeO_{1.8}$ compared to $CeO_{1.95}$ are also consistent with a competition between Ce reduction by Cu at stoichiometric sites and ceria oxidation by Cu at oxygen vacancies, with more of the latter occurring on $CeO_{1.8}$. To better understand these shifts, we must analyze them in some detail. Qualitatively similar shifts in the Cu $2p_{3/2}$ BE and Auger parameter to those observed here were seen by Madey et al.[111] for Cu nanoparticles on a thin film of $Al_2O_3(0001)$ on Re(0001), and analyzed in quantitative detail to determine the initial- and final-state contributions to the Cu BE shift. That same method was used to analyze Ag nanoparticles on slightly reduced $CeO_2(111)$.[123] We now apply that same method to analyze the present data at 1.2 ML Cu, where the average particle diameter is 1.8 nm. Compared to the high-coverage (bulk Cu) limit, the Cu $2p_{3/2}$ BE at this coverage on $CeO_{1.95}(111)$ was 0.25 eV higher ($\Delta BE = +0.25$ eV) and the Cu Auger parameter was 0.7 eV smaller ($\Delta\alpha= -0.7$ eV). Dividing $\Delta\alpha$ by -2 gives an estimate of the BE shift due to final-state relaxation effects, which here is $-\Delta\alpha/2= +0.35$ eV. Subtracting this from the observed BE shift of +0.25 eV gives an estimate of the initial-state BE shift alone, which is (0.25 – 0.35) eV = -0.1 eV. At this coverage on $CeO_{1.8}(111)$, $\Delta BE = +0.15$ eV and $\Delta\alpha = -1.1$ eV. Dividing $\Delta\alpha$ by -2 gives an estimate of the BE shift due to final-state relaxation effects, which here is $\Delta\alpha/2 = +0.55$ eV. Subtracting this from the observed BE shift of +0.15 eV gives an estimate of the initial-state BE shift alone, which is (0.15 – 0.55) eV = -0.4 eV. This decrease in Cu $2p_{3/2}$ BE (after correction for final-state effects) for 1.8 nm particles on both surfaces (relative to bulk Cu) suggests some transfer of electron density from the ceria to the Cu, which is perhaps insignificantly small on $CeO_{1.95}(111)$, but quite significant on $CeO_{1.8}(111)$. The transfer of a slight amount of electron density from Cu to ceria, apparent from Fig. 6, is not detected through this analysis of Cu peak positions. This may be associated with a failure of the assumption, implicit in this analysis that the change in Auger parameter is only due to final state effects, when initial state effects could also contribute to $\Delta\alpha$.

These results are consistent with DFT calculations which predict that Cu adsorption to oxygen vacancies on $CeO_2(111)$ causes transfer of electron density from Ce^{3+} to Cu, forming a partial negative charge on Cu.[35,116] There are more vacancies where this can occur on the more reduced $CeO_{1.8}(111)$ surface. On the $CeO_{1.95}(111)$, this still occurs at step edges only, but the opposite effect occurs to a greater extent at the stoichiometric sites on both steps and terraces. We observed no broadening in the Cu $2p_{3/2}$ peak compared to the highest Cu coverage, as might be expected when both effects occur, but this is not surprising since they occur at the base of the same Cu particle, whose delocalized electrons bring it to a single average potential.

This interpretation is consistent with the results of Matolin et al.[2] shown in Fig. 4.6, whereby Cu reduced stoichiometric $CeO_2(111)$, but initially oxidized the heavily reduced $CeO_{1.73}(111)$ surface. Because Cu adsorbs mainly at step edges at very low coverage on $CeO_{1.73}(111)$, Cu is mainly binding to oxygen vacancies, where DFT predicts that it will gain electron density from ceria.[35,116]

While it is energetically very unfavorable to reduce Al^{3+} with Cu to form Cu^+,[9,111] and no reduction of Al_2O_3 was observed upon Cu adsorption,[21] ceria is much easier to reduce. Nevertheless, the net reaction 2 CeO_2(solid) + 2 Cu(s) → Ce_2O_3(solid) + Cu_2O(solid) is still uphill by 212 kJ/mol (calculated from their standard heats of formation). Experimental trends in metal reduction of oxides upon adsorption at submonolayer coverages and 300 K closely follow bulk thermodynamic predictions as described by Campbell.[9] According to that trend, this +212 kJ/mol is sufficiently endothermic that one would not expect Cu to reduce ceria. This lends further support to the explanation for the apparent reduction of ceria in Fig. 4.6 as arising from selective attenuation of the Ce^{4+} XPS signal by Cu, due to its preference for stoichiometric sites. The reaction enthalpy remains almost as endothermic (less by only ~50 kJ/mol O) when one considers the analogous bulk reaction but where Ce_2O_3(solid) is replaced by $CeO_{1.99}$, i.e., representing a very slight reduction.[124] At some point near that stoichiometry, entropic effects will tip the bulk thermodynamic balance.

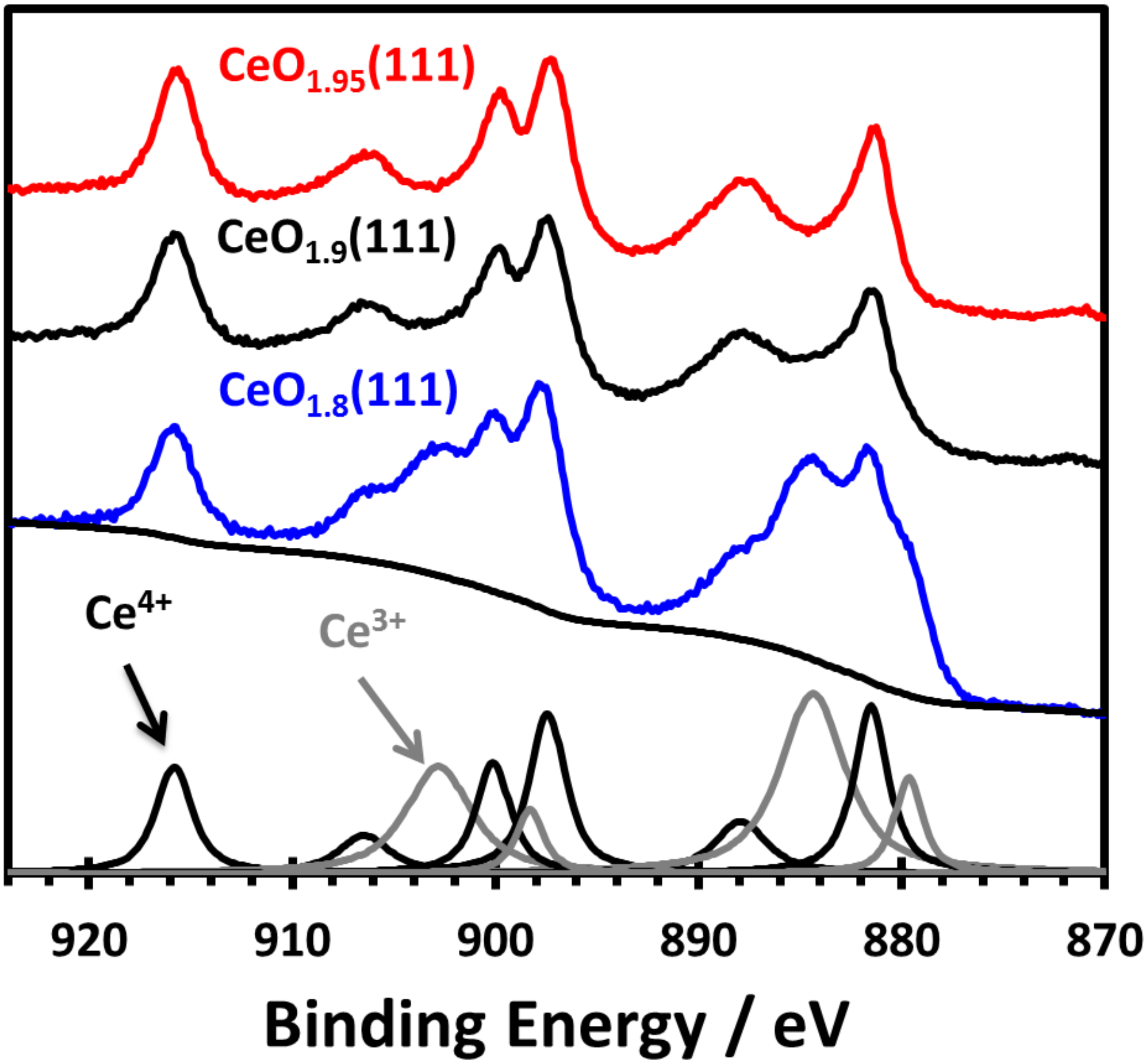

Figure 4.1: Representative Al Kα XPS spectra of Ce 3d region collected at 300 K on 4 nm thick $CeO_{2-x}(111)$ films grown on Pt(111) with stoichiometries of (a) $CeO_{1.95}(111)$, (b) $CeO_{1.9}(111)$, and (c) $CeO_{1.8}(111)$ with the Shirley background subtracted for peak fitting, and (d) an example deconstruction of the Ce 3d region for $CeO_{1.8}(111)$ in spectrum (c) used for determining the cerium oxidation state. The more reduced films were prepared by growing $CeO_{2-x}(111)$ in a lower O_2 background pressure and post annealing to the desired oxidation state.

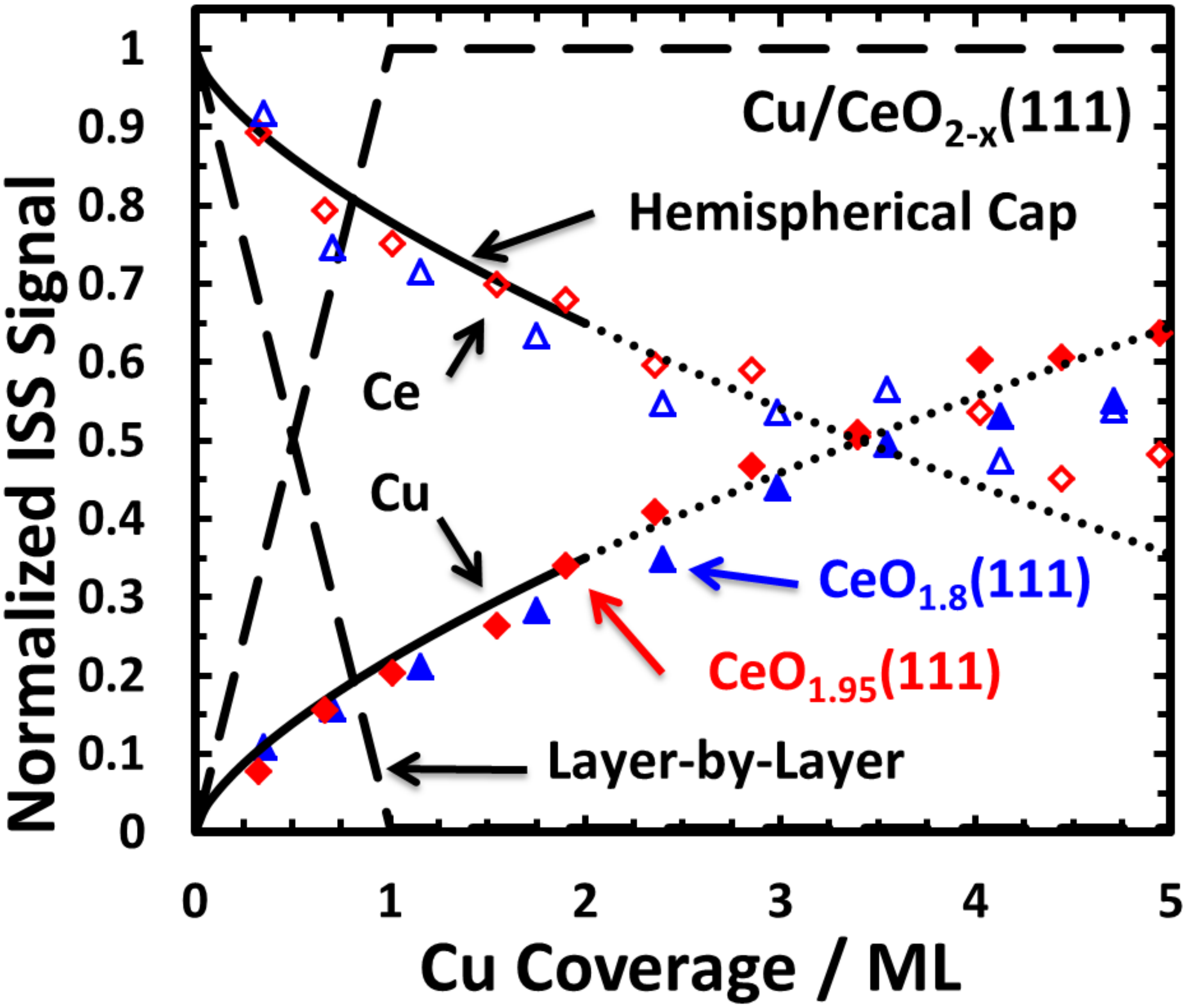

Figure 4.2(a): Integrated Cu (closed symbols) and Ce (open symbols) LEIS signal intensities (normalized to thick multilayer Cu and clean $CeO_{2-x}(111)$, respectively) as a function of Cu coverage after deposition onto $CeO_{1.95}(111)$ (diamonds) and $CeO_{1.8}(111)$ (triangles) at 300 K. The dashed line corresponds to the normalized LEIS signal that would be observed if Cu grew in a layer-by-layer fashion, while the solid line corresponds to Cu growing as hemispherical caps with a fixed radius and a fixed particle density of 7.8×10^{12} particles/cm^2. This model is only reasonable up to ~35% of the surface being covered by particles, since they may start to overlap with each other at higher coverage, so the dotted lines after that are only a guide to the eye.

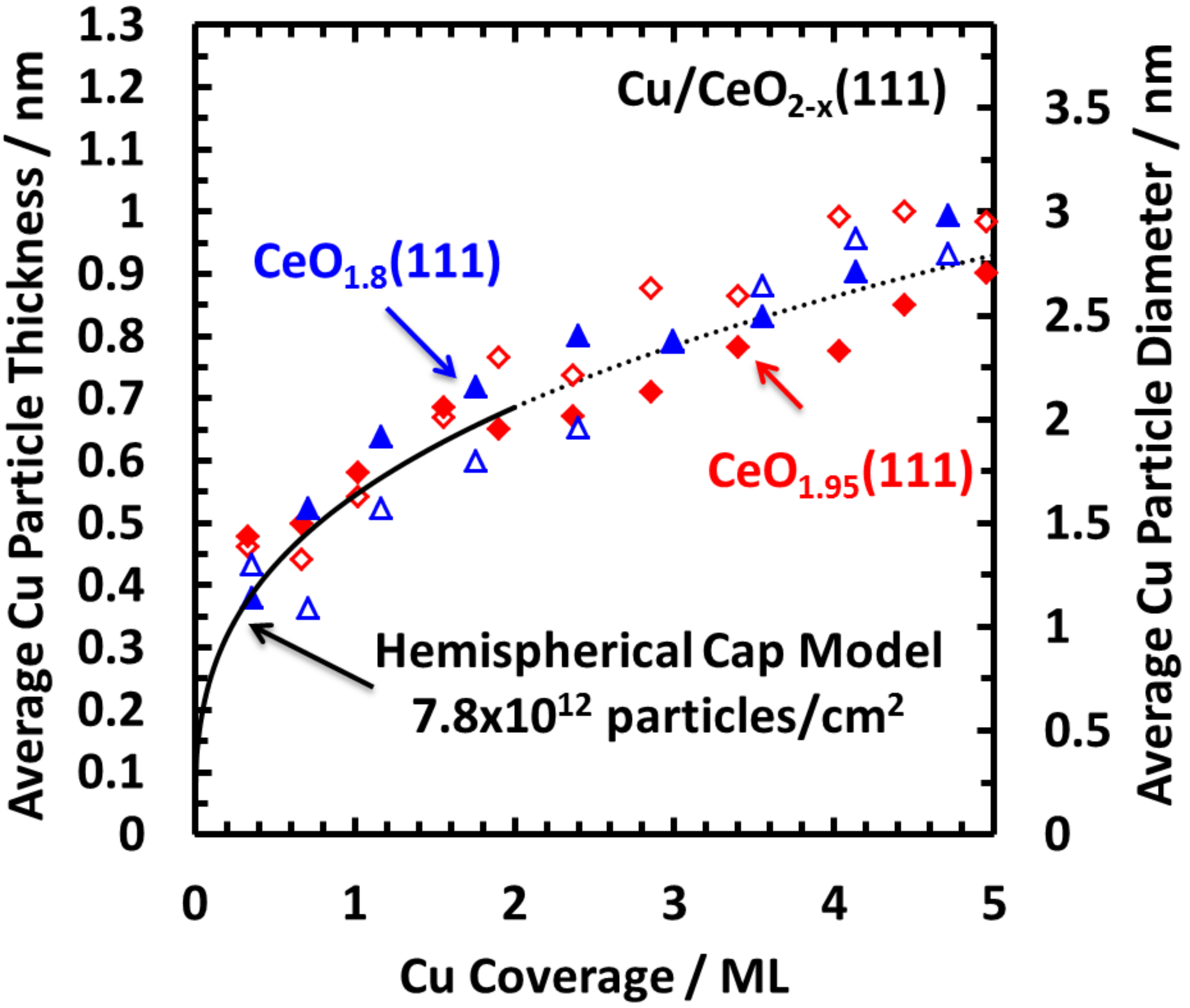

Figure 4.2(b): The average Cu particle thickness versus Cu coverage calculated from the Cu (closed) and Ce (open) LEIS data points of Fig. 2(a), and on the right axis, the average diameter of hemispherical caps that corresponds to this thickness. Also shown is the result expected for the same hemispherical-cap model and particle number density as used for the best fit to the data in part (a).

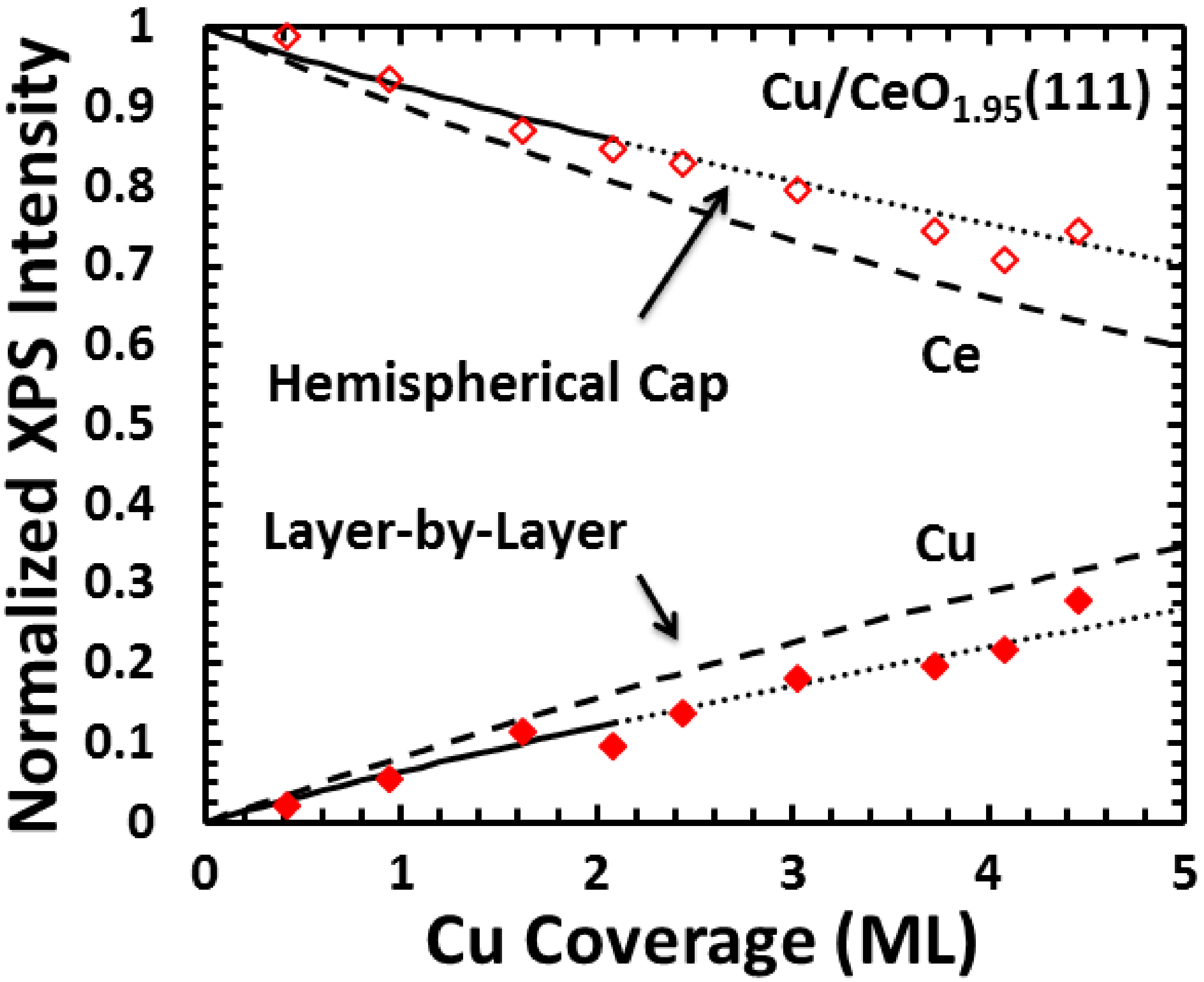

Figure 4.3: Integrated Cu $2p_{3/2}$ (closed) and Ce 3d (open) XPS signal intensities (detected normal to the surface) normalized to bulk Cu and clean $CeO_{2-x}(111)$ respectively as a function of Cu deposition at 300 K onto $CeO_{1.95}(111)$ (average of 3 experiments). The dashed line corresponds to the normalized XPS signal that would be observed if Cu grew in a layer-by-layer fashion, while the solid line corresponds to Cu growing as hemispherical caps with a fixed radius and a fixed particle density of $7.8x10^{12}$ particles/cm^2 (which is valid only up to ~2.2 ML, see above).

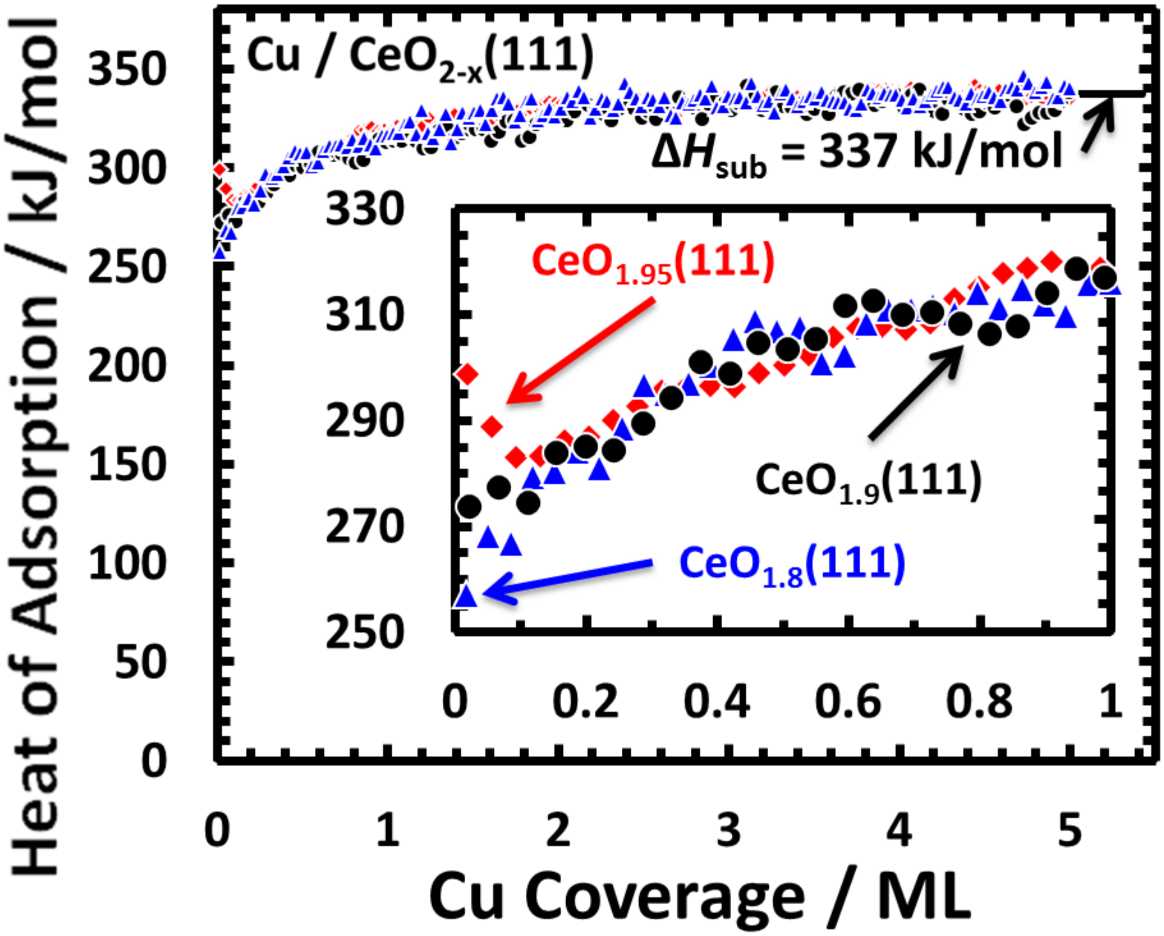

Figure 4.4: Heat of Cu atom adsorption on $CeO_{1.95}(111)$ (diamonds) [average of 5 experiments], $CeO_{1.9}(111)$ (circles) [average of 3 experiments] and $CeO_{1.8}(111)$ (triangles) [average of 3 experiments], all at 300 K, as a function of Cu coverage.

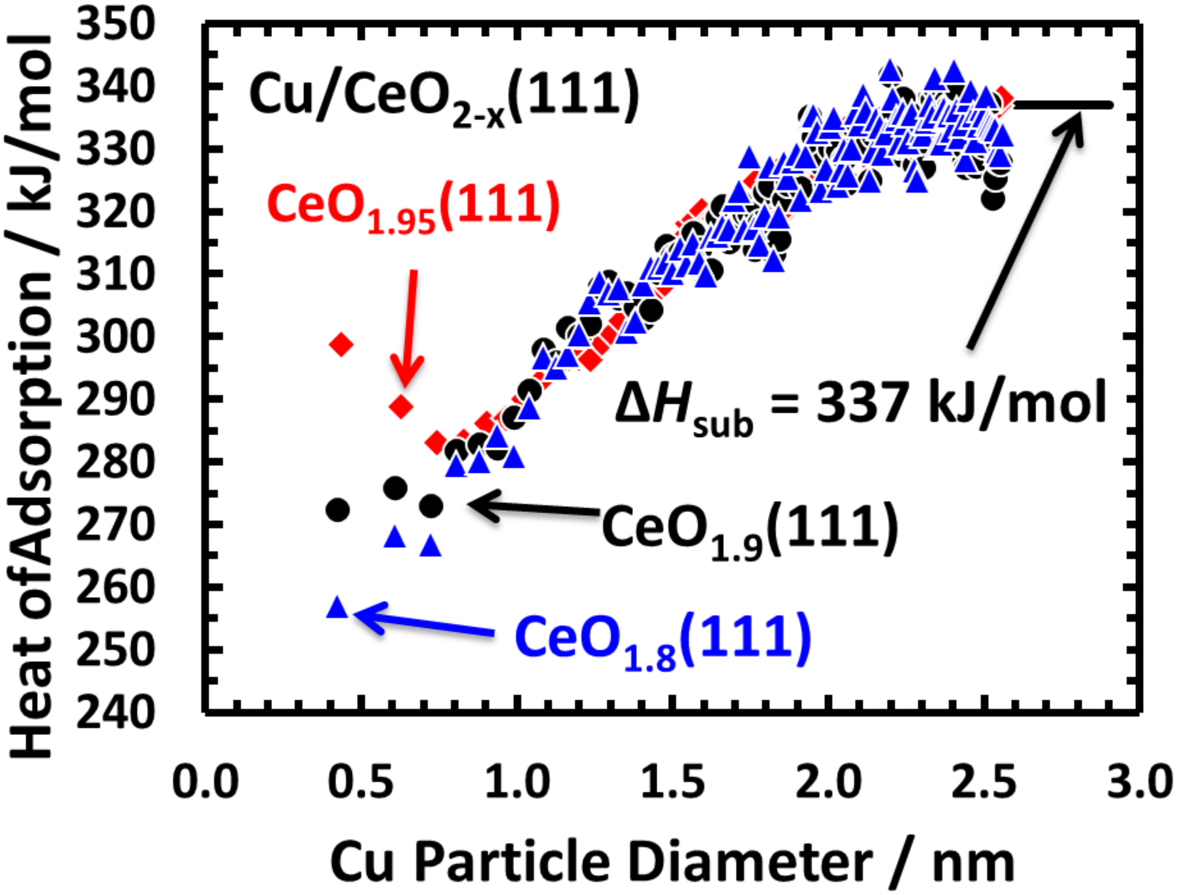

Figure 4.5: Heat of Cu atom adsorption $CeO_{1.95}(111)$ (diamonds) [average of 5 experiments], $CeO_{1.9}(111)$ (circles) [average of 3 experiments] and $CeO_{1.8}(111)$ (triangles) [average of 3 experiments], all at 300 K, as a function of the average Cu particle diameter to which Cu atoms add.

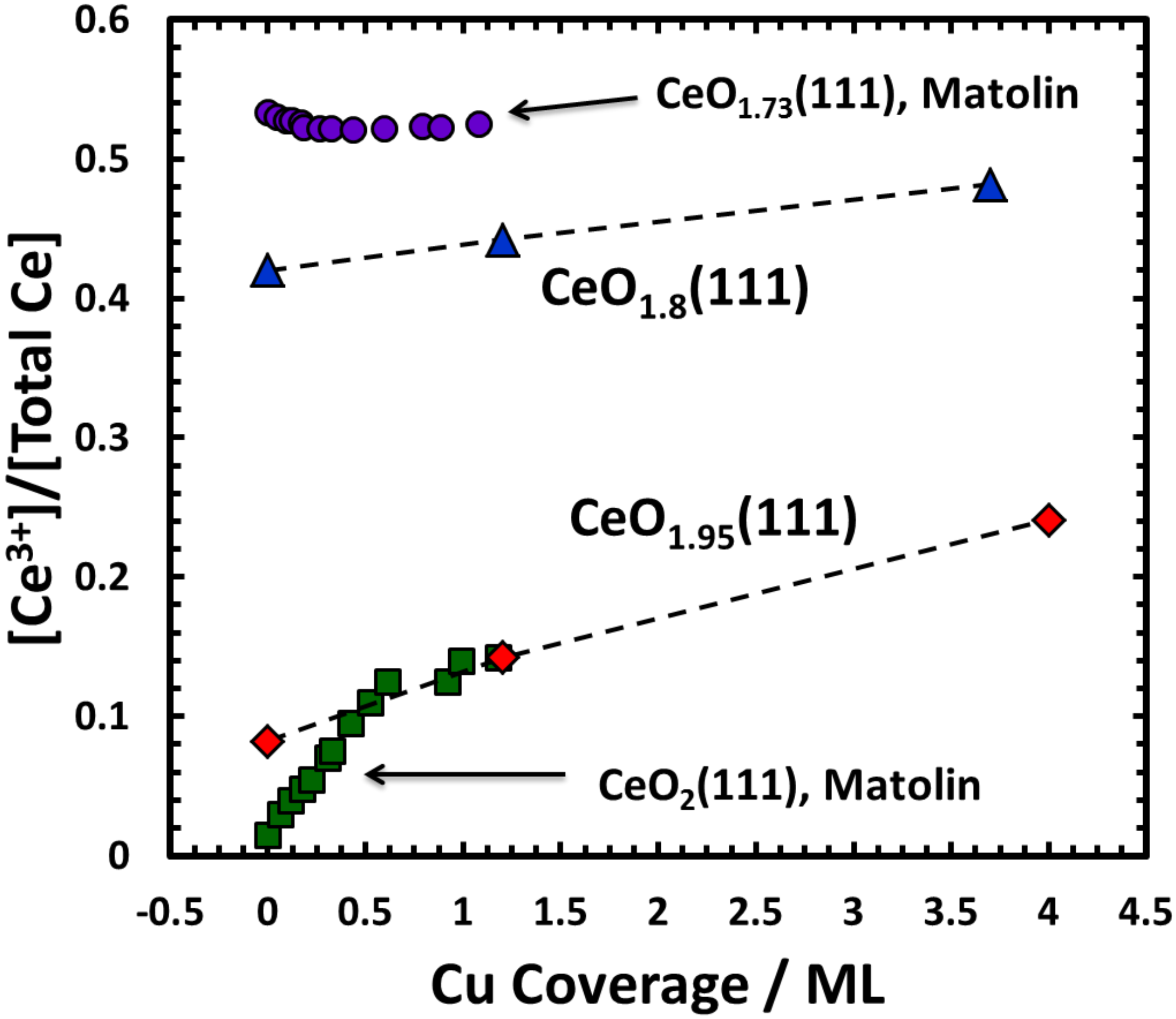

Figure 4.6: The Ce^{3+} contribution to the total Ce 3d XPS signal from $CeO_{2-x}(111)$ (determined by fitting the Ce 3d lineshape as in Fig. 1), as a function of Cu coverage deposited onto $CeO_{1.95}(111)$ (diamonds) and $CeO_{1.8}(111)$ (triangles) at 300 K. Dashed lines are to aid the eye. Also shown for comparison are data from Matolin et al.[2] for $CeO_2(111)$ that was initially fully oxidized (green squares) and heavily reduced (purple circles).

Chapter 5

The Energy of Supported Metal Catalysts: from Single Atoms to Large Metal Nanoparticles

This Chapter has been published as:

T.E. James, S.L. Hemmingson, C.T. Campbell, *ACS Catal.*, 2015, 5, 5673-5978

Many catalysts consist of late transition metal nanoparticles dispersed across oxide supports. The chemical potential of the metal atoms in these particles correlate with their catalytic activity and long-term thermal stability. This chemical potential versus particle size, across the full size range between the single isolated atom and bulk-like limits, is reported here for the first time for any metal on any oxide. The chemical potential of Cu atoms on $CeO_2(111)$ surfaces, determined by single crystal adsorption calorimetry (SCAC) of gaseous Cu atoms onto slightly-reduced $CeO_2(111)$ at 100 and 300 K, is shown to decrease dramatically with increasing Cu cluster size. The Cu chemical potential is ~110 kJ/mol higher for isolated Cu adatoms on stoichiometric terrace sites than for Cu in nanoparticles exceeding 2.5 nm diameter, where it reaches the bulk Cu(solid) limit. In Cu dimers, Cu's chemical potential is ~57 kJ/mol lower at step edges than on stoichiometric terrace sites. Since Cu avoids oxygen vacancies, these monomer and dimer results are not strongly influenced by the 2.5% oxygen vacancies present on this CeO_2 surface, and are thus considered representative of stoichiometric $CeO_2(111)$ surfaces.

5.1 Introduction

Late transition metal nanoparticles dispersed across oxide supports form the basis of industrially important heterogeneous catalysts and are the subject of intensive research.[10,31,54,104,105,125-134] The strength of bonding of the metal to the oxide support has been shown to control the chemical potential of the metal atoms in the nanoparticles and how it varies with particle size.[10,104,105,134] This chemical potential in turn influences how strongly adsorbed catalytic reaction intermediates bind to the metal particles[105] and how quickly the particles deactivate by sintering.[10,54] Thus, understanding the strength of bonding of late transition metals to oxide support and the resulting metal chemical potential is crucial for understanding structure – function relationships in catalysis. However, no one has previously reported an experimental measurement of the adsorption energy of any late transition metal adsorbed in the form of isolated atoms on any oxide surface. We report here calorimetric measurements of the adsorption energies of Cu atoms onto $CeO_2(111)$ under conditions where they remain as isolated adatoms on terraces and where they grow as Cu nanoparticles with controllable average size. We estimate from these the chemical potential versus particle size across the full range from single Cu adatoms to the bulk Cu(solid) limit. This has never been reported for any late transition metal on any oxide surface and provides a simple benchmark for validating the energy accuracy of quantum mechanical calculations of metal/oxide bonding, e.g., density functional theory (DFT). These $Cu/CeO_2(111)$ model catalysts address the crucial role of ceria as a support[2,10,34-39,54,115,135-139] and of Cu nanoparticles in industrial catalysis.[31,130,131]

In this work, Cu was dosed onto a slightly reduced $CeO_2(111)$ surface at 100K and its heat of adsorption was measured by calorimetry, while the resulting structure of the adsorbed Cu and Cu nanoparticle size were characterized using surface spectroscopies. The results are compared to our previous study of Cu adsorption onto this same surface at 300K, where Cu makes clusters at step edges even at the lowest coverage studied.[3] Cooling to 100K enables production of isolated Cu adatoms located on stoichiometric $CeO_2(111)$ terraces. We also compare these results to previous DFT+U studies of the adsorption energy of Cu atoms on stoichiometric and reduced $CeO_2(111)$ surfaces.[34-38]

5.2 Results

5.2.1 $CeO_2(111)$ Thin Film Characterization.

The $CeO_2(111)$ thin films used were grown on a Pt(111) substrate and characterized as described previously[3,14]. They were grown to a thickness of 4 nm, which is twice the thickness needed to achieve bulk-like heats of adsorption for Ag atoms.[14] The ceria oxidation state was verified by XPS of the Ce 3d region as described previously,[3] measuring the contribution of Ce^{3+} to the total integrated area of the 3d region ($[Ce^{3+}]/([Ce^{3+}]+[Ce^{4+}])$).[106] This showed the CeO_2 surface to have ~2.5% oxygen vacancies (i.e., $CeO_{1.95}$), which are known to reside mainly at step edges[136] which cover ~5% of the surface.[3]

5.2.2 Cu Film Growth Morphology on $CeO_{1.95}(111)$ at 100K.

Discreet amounts of Cu were deposited onto $CeO_{1.95}(111)$ films at 100 K using the same Cu atomic beam as in the calorimetry experiments and the Cu and Ce signals were monitored using He^+ LEIS (Figure 5.1(a)). Total Cu coverage is defined in monolayers (ML) where 1 ML = 7.89×10^{14} atoms/cm^2, the density of O atoms in the top layer of $CeO_2(111)$. The integrated LEIS intensity of the Cu was normalized to that from a thick enough Cu overlayer to block all the Ce signal (>40 ML). The Ce LEIS signal was normalized to that for clean $CeO_{1.95}(111)$ before Cu deposition. The Cu LEIS intensity increased with Cu coverage while the Ce LEIS intensity decreased. As shown, the data deviate strongly from the layer-by-layer (2D) growth model but are well fit by the hemispherical cap (3D) model, which assumes Cu grows as hemispherical particles with an fixed particle diameter, D, at any coverage, and a fixed number density of particles, n, independent of coverage.[21] The fixed density of particles is a well-known consequence of particle growth kinetics whereby a saturation density of clusters is formed at very low coverage and stays constant thereafter.[19] Since n and D are mathematically related for a given total Cu coverage, n is the only fitting parameter.[21] When the angle of detection is normal to the surface but the ions are incident at angle $\square_i$ = 45° from normal as here, that model gives that the fraction of the ceria substrate signal masked by Cu particles equals $n\pi D^2(1 + 1/\cos\theta_i)/8$,[108] $= (1.207)n\pi D^2/4$. The least squares best fit shown in Figure 5.1(a), gives n = $5.3\text{x}10^{13}$ particles/cm^2 for Cu adsorption onto $CeO_{1.95}(111)$ at 100 K. This is ~7 times greater than observed for similarly prepared $CeO_{1.95}(111)$ surfaces and similar flux but at 300 K ($7.8\text{x}10^{12}$ particles/cm^2).[3] The higher density is expected at 100 K, since kinetic growth models appropriate for these conditions predict a saturation number density that varies as the inverse cube root of the Cu monomer diffusion constant across the surface,[19] which will be much smaller at 100 K than at 300 K. Within that model, this ratio of 7 corresponds to an activation energy for Cu monomer diffusion of ~7 kJ/mol on $CeO_2(111)$.

To ensure no ion-beam damage in Figure 5.1(a), a growth experiment was performed with only two Cu coverages (1 and 2 ML), giving much less total ion beam exposure up to 2 ML. These data fell within error of Figure 5.1(a), indicating that no ion-beam damage occurred.

The normalized LEIS signals in Figure 1(a) directly provide the fraction of the ceria surface whose signal is masked by Cu particles, and the fraction of the total maximum Cu signal (due to complete coverage by Cu) that is observed at any given Cu coverage. If we assume the masked area is expanded from the actual footprint of the Cu particles due to macroscopic shadowing by the same factor as for hemispherical caps ($(1 + 1/\cos\theta_i)/2 = 1.207$, see above), dividing these fractions by 1.207 gives the area fractions actually covered by Cu particles. Since we know the average Cu film thickness from the Cu coverage (assuming the Cu particles have the density of bulk Cu(solid)), dividing it by this covered fraction for each point gives the average thickness of the Cu particles. Figure 5.1(b) shows the average Cu particle thickness versus Cu coverage estimated in this way. These thicknesses would only decrease by 21% even if we assumed no macroscopic shadowing, so this hemispherical-shape assumption has only a small effect on the thickness plotted here. Since the average thickness of a hemispherical cap is 1/3 its diameter, we multiplied this thickness by 3 to show the corresponding average effective diameter along the right-hand axis here. For comparison, the result expected from the same hemispherical-cap model and particle number density as used for the best fit to the top part of Figure 1 shows excellent agreement. The XPS signals observed were also consistent with this hemispherical cap model,[3] but much less surface sensitive than LEIS, so not presented. It is unlikely that the deposited Cu was incorporated into the ceria film as a dopant (i.e. substituting for a Ce atom) due to the high activation energy expected. (The energy cost to create a Ce vacancy is 1833 kJ/mol[35] and surface Ce vacancies are absent in these as-prepared $CeO_2(111)$ films.[14])

5.2.3 Heats of Cu Adsorption on $CeO_{1.95}(111)$ at 100K.

Figure 5.2 shows the heat of adsorption of Cu onto $CeO_{1.95}(111)$ at 100K, and at 300 K from Ref.[3] as a comparison. All heats of adsorption reported here have been corrected slightly for the hot temperature and directed nature of the Cu atomic beam, to correspond to Cu atoms in a Boltzmann distribution at the surface temperature, and RT has been subtracted from the measured energies, as we always do in calorimetry.[17,18,140] This is done so the values on plots like Figure 2 (times -1) equal the standard enthalpy of adsorption at the sample temperature. At 100K, Cu adsorbs with an initial heat of adsorption of 225 kJ/mol, remains nearly constant for the first two gas pulses, and then increases with coverage to asymptotically approach the standard heat of sublimation of bulk Cu(solid) (337 kJ/mol at 300 K[78] and 332 kJ/mol at 100 K[78]) by 5 ML. The sticking probability of Cu atoms was found to be unity at all coverages. As shown in Figure 5.2, the initial heat of adsorption of Cu on $CeO_{1.95}(111)$ at 100K is 75 kJ/mol lower than at 300K and remains lower at all coverages. The Cu heat of adsorption on $CeO_{1.95}(111)$ at 100K converges to the heat of sublimation by 5 ML, which is slower than at 300K. The difference in initial heats of adsorption is partially due to the smaller particles at 100 K (see below), but also partially due Cu nanoparticles aggregating primarily at step sites at 300K[3] but on terraces at 100K due to slower Cu adatom diffusion at 100K (see below).

Using the particle density from the hemispherical cap model in Figure 5.1(a) and the total Cu coverage in Figure 5.2, the measured heats are replotted as Cu heat of adsorption vs. average Cu particle diameter in Figure 5.3. Again the Cu heat of adsorption on $CeO_{1.95}(111)$ at 300K from Ref. [3] is shown for comparison. The plot is truncated for nanoparticles larger than 0.85 nm at 100 K (equivalent to 1 ML total coverage) because the fractional surface covered reached 35%, above which the hemispherical cap model might begin to break down due to particles possibly overlapping each other. The heat of adsorption for Cu nanoparticles with a similar particle diameter in the range 0.45 to 0.8 nm is lower at 100K than 300K due to different adsorption sites at the two temperatures (see below). The particle density determined from the fit to the hemispherical cap model is larger than the number of Cu atoms per unit area adsorbed in the first two gas pulses, indicating that these two calorimetry pulses produce only isolated Cu adatoms at 100K. The effective hemispherical Cu particle diameter is 0.22 nm and 0.32 nm for these pulses, which correspond to particle volumes of 2.9×10^{-3} and 8.6×10^{-3} nm^3, respectively, both smaller than the volume per atom in bulk Cu(solid), 1.18×10^{-2} nm^3 based on its density.[78] This is of course impossible, which we attribute to a breakdown of the assumption of fixed density of nuclei at such low coverages. The nuclei here are single, isolated Cu adatoms, and their number density increases in these first two pulses. These two pulses gave the same heat of adsorption within 3 kJ/mol, which does not increase with coverage (effective diameter) in this ultra-small size range as at larger sizes. This is again consistent with these two pulses producing the same structure: isolated Cu adatoms on $CeO_2(111)$ terraces. These heats for isolated Cu adatoms average 224kJ/mol. This value will allow for much more direct comparisons to DFT results than all our earlier calorimetry measurements of such systems, where multi-atom clusters of unknown geometry were made in the first gas pulse (see below). Figure 5.3 represents the first measurement of the heat of any metal adsorption on any oxide which covers the full size range from isolated metal adatoms to such large metal nanoparticles that they have reached the bulk limit.

Since Figure 5.3 presents *differential* heats of adsorption, these differences in heats of adsorption with size directly reflect differences with size in the chemical potential of the metal atoms, but with opposite sign. Neglecting entropic contributions to the free energy, which change very little with particles size compared to the huge enthalpic changes here, the chemical potential of a metal atom in a particle of diameter D, $\mu(D)$, is higher than that in the bulk metal, $\mu(\infty)$, by an amount equal to the heat of sublimation of bulk Cu minus the differential heat of Cu adsorption at diameter D.[105] Thus, another way to view the data from Figure 5.3 is to plot this chemical potential (relative to that for the bulk metal, $\mu(\infty)$, which we set as the reference zero here) versus average effective diameter, as shown in Figure 5.4. Here we have corrected the first two data points at 100 K to reflect the proper effective hemisphere diameter of single, isolated atoms. As seen, these Cu adatoms at terrace sites are ~110 kJ/mol higher in chemical potential than Cu atoms in particles that have reached the large-size limit (>2.5 nm). This shows why it is challenging to make so-called single-site catalysts (i.e., isolated late transition metal adatoms on supports). This drop in chemical potential with size reflects the thermodynamic driving force for catalysts to sinter into larger particles with time on stream.[10,105] It also reflects a decreasing propensity for the metal to bind strongly to small adsorbates, mainly associated with the decreasing degree of coordinative unsaturation as size grows.[105] Also clear in Figure 5.4 is the large decrease in chemical potential of ~57 kJ/mol between Cu in dimers at step edges compared to dimers on terraces. Once the particles exceed 0.85 nm in diameter, this stabilization by step edges has diminished to an undetectable level.

5.3 Discussion

In Figure 5.3, the difference in the heats of adsorption at 100 K versus 300 K for Cu on $CeO_{1.95}(111)$ for nanoparticles of the same size below 0.85 nm in diameter is attributed to differences in binding sites of the nanoparticles. Although there are no STM images available for Cu adsorption on $CeO_{1.95}(111)$, we have proposed that the majority of Cu atoms deposited at 300K are nucleated into nanoparticles at step edges (including kink sites)[3] to explain adsorption heats and other data at 300 K for Cu on $CeO_{1.95}(111)$, most importantly the initial decrease in heat of adsorption with coverage and particle size (Figs. 5.2-5.3) as these step sites get titrated (Particle-particle repulsions probably keep the steps from getting completely covered by particles.). This is consistent with STM results for similar systems (nanoparticles of Ag[114] and Au[115] on $CeO_2(111)$ and Cu on Al_2O_3[113] and $TiO_2(110)$[112] at 300K).

When grown at 100K, the particle density increases 7-fold compared to 300K (5.3×10^{13} vs. 7.8×10^{12} particles/cm^2, respectively). Similar increases in particle density were observed by Freund et al.[115,141] for Au on $CeO_2(111)$ at 100 versus 300K, with the increased density at 100 K due to Au particles nucleated on terraces as opposed to much more predominantly at steps at 300 K. The increased particle density for Cu/$CeO_{1.95}(111)$ at 100K is also attributed to nucleation of Cu nanoparticles mainly on terraces, whereas they nucleate mainly on steps at 300 K.[3] This explains the 52 kJ/mol lower heat of adsorption at 100K versus 300K in Figure 5.3 for 0.44 nm diameter Cu particles (the smallest Cu nanoparticles measured at 300 K), given the well-known lower stability metal nanoparticles on terraces compared to steps.[142] This difference in heats of adsorption slowly diminishes with size to zero by 0.85 nm, probably because the increasing footprint of the Cu particles is mainly associated with their expanding onto terraces above 0.85 nm, even when they started at step edges. The nanoparticles are probably not exclusively nucleated at steps for adsorption at 300K nor terraces at 100K, but these are their dominant nucleation sites.

Since this surface has 2.5% oxygen vacancies (mainly at step edges),[3] the Cu atoms may be located at a mixture of oxygen vacancies and stoichiometric ceria sites. However, Since DFT results from both Fabris et al.,[34] and Hermansson et al.[35] predicted that Cu binds 1.4 eV to 1.2 eV (135 kJ/mol and 116 kJ/mol) more strongly to stoichiometric ceria sites on (111) terraces than to oxygen vacancies in (111) terraces, consistent with our experimental result that Cu in 0.4 nm diameter particles is ~40 kJ/mol less stable on the more reduced $CeO_{1.8}$(111)surface than on $CeO_{1.95}$(111)[3], the isolated Cu adatoms produced here at 100 K on terraces surely adsorb only to stoichiometric sites, and avoid bonding to oxygen vacancies. At 300 K, Cu diffuses fast enough to reach step edges, where it binds more strongly than at terraces in spite of these steps missing ~half their oxygens.[3]

These results provide benchmarks to test the energy accuracy of computational estimates of metal bonding to oxide surfaces. Table 5.1 compares the measured adsorption energy for Cu adatoms on stoichiometric CeO_2(111) to published DFT+U results at its most stable adsorption geometry (using periodic boundary conditions within the generalized gradient approximation (GGA)).[143] In order to properly describe the localization of the Ce 4f electrons, a Hubbard parameter (U) was added to the functionals, as summarized in Table 5.1.[137-139] These calculated Cu adsorption energies are generally higher by 30 – 69 kJ/mol than our experimental result. Since the heat capacity of solids is generally smaller than gases at low temperature, part of this difference may be due to the fact that the calculation is at 0 K while the measurement is at 100 K. This could only account for <2.1 kJ/mol of the difference since the average heat capacity difference is surely less than the heat capacity of Cu(gas) (5/2 R). This main difference can be associated with the use of large U values. The result by Illas et al.[38] using a lower U (3 eV) is the only calculation to underestimate the adsorption energy, although the magnitude of the error is not improved. Huang et al.[39] showed that calculated adsorption energies for CO on $CeO_2(111)$ were better represented using lower U values (2-3 eV), and suggested that lower U is probably required whenever describing electron transfer reactions. Also listed in Table 5.1 are the charge transfers predicated by DFT, which are generally >+0.66. Using the PBE + 4.5 functional, the calculated charge transfer is greater than PBE +5; however, PW91 gives a similar extent of charge transfer, independent of U value. Out XPS results indicate only a small amount of electron density is transferred from Cu to $CeO_2(111)$, less than 0.17 electrons per Cu atom at 1.2 ML Cu coverage.[3] In our XPS results, Cu is adsorbing to a combination of stoichiometric Cu sites and O vacancies at step edges at 1.2 ML Cu coverage. However, when analyzed in this same way, the data of Matolin et al.[2] on $CeO_{1.99}(111)$ give 0.62 electrons per Cu atom up to 0.6 ML, after which it tracks our data. It thus seems that all these DFT functionals are overestimating the extent of charge transfer, although the change transfer per Cu atom is not known from experiments at the very low coverage and temperature required to maintain isolated Cu adatoms.

Table 5.1: Calculated heats of adsorption of isolated Cu adatoms on the most stable Cu adsorption site of CeO$_2$(111) using DFT+U compared to the experimental value, and the deviations from this experiment. To correct for the difference between enthalpies and energies, 0.8 kJ/mol (RT) was added to the calculated energies. Also listed are the U value and slab thickness used in each calculation, and the resulting charge on the Cu adatom. All calculations used a 2x2 cell. One trilayer is defined as an O-Ce-O trilayer.

ΔH_{ad} (kJ/mol)	**ΔH_{ad} error (kJ/mol)**	**Cu charge**	**DFT functional**	**U (eV)**	**Slab thickness (trilayers)**	**Source**
224±7	**-**	**-**	**(EXPERIMENT)**	**-**	**-**	**This Work**
293	**69**	**1+**	**PBE**	**4.5**	**3**	**[34]**
260	**36**	**0.66+**	**PBE**	**5**	**3**	**[35]**
254	**30**	**1+**	**PBE**	**4.5**	**4**	**[36]**
259	**35**	**0.67+**	**PBE**	**5**	**2**	**[37]**
180	**-44**	**0.70+**	**PW91***	**5 then 3***	**2**	**[38]***
270	**46**	**0.71+**	**PW91**	**5**		
336	**112**		**LDA**	**5**		

* Illas et al.[38] pointed out that GGA tends to overestimate the CeO$_2$(111) lattice parameter, and so they used the local density approximation (LDA) with the functional of Vosko et al.[143] (VWN) with U = 5 for geometry optimization but used GGA with the Pedrew-Wang (PW91)[144] functional and U = 3 for energy and electronic calculations. They also performed pure GGA and LDA calculations for comparison, listed in the last two rows here.

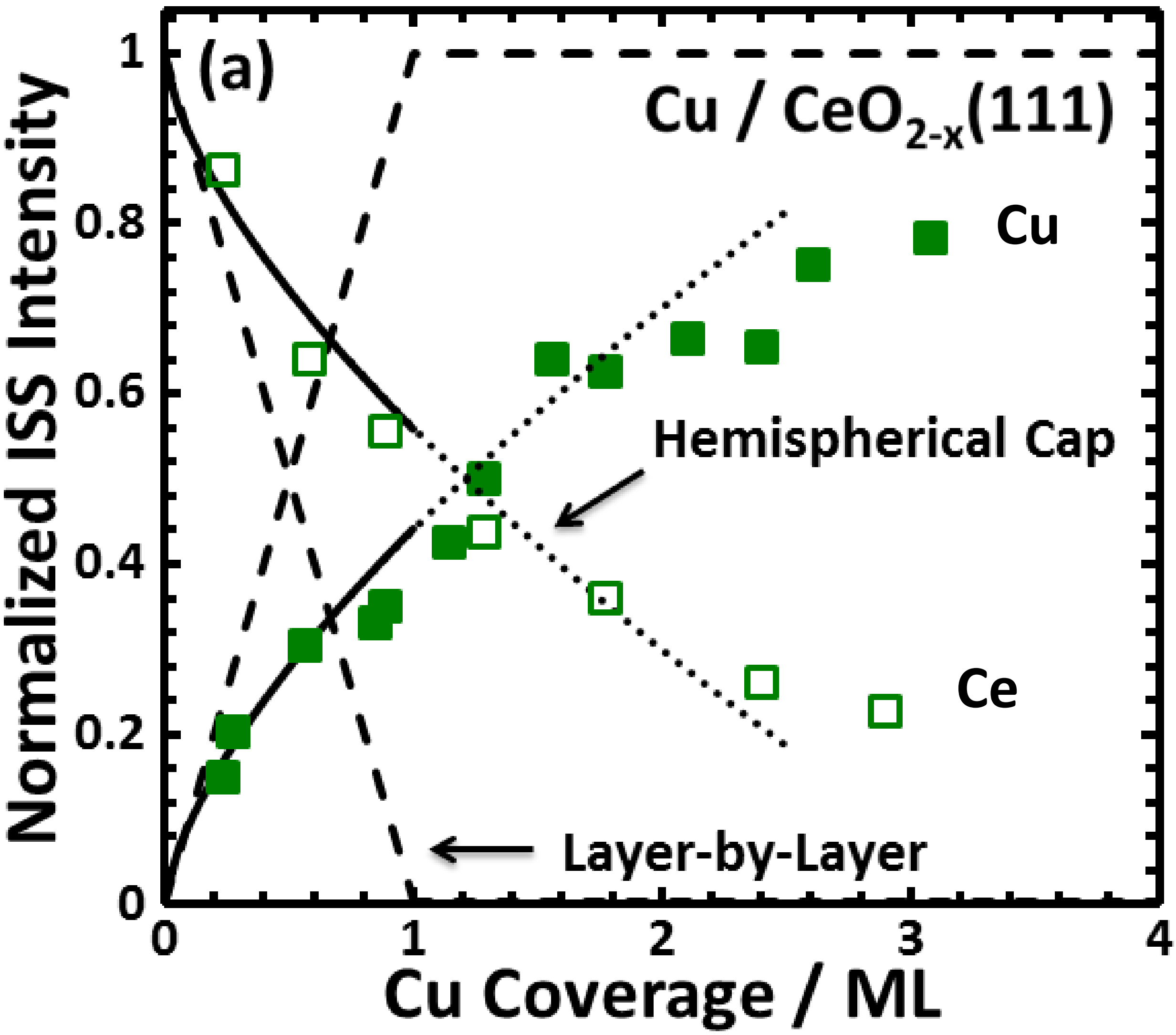

Figure 5.1(a): Integrated Cu (closed) and Ce (open) LEIS signal intensities normalized to bulk like (>40 ML) Cu and clean $CeO_{1.95}(111)$ respectively as a function of total Cu coverage at 100 K onto $CeO_{1.95}(111)$. The dashed line represents a layer-by-layer fit for 2-dimensional growth of Cu. The solid line represents a hemispherical cap fit with a fixed particle density of 5.3×10^{13} particles/cm^2.

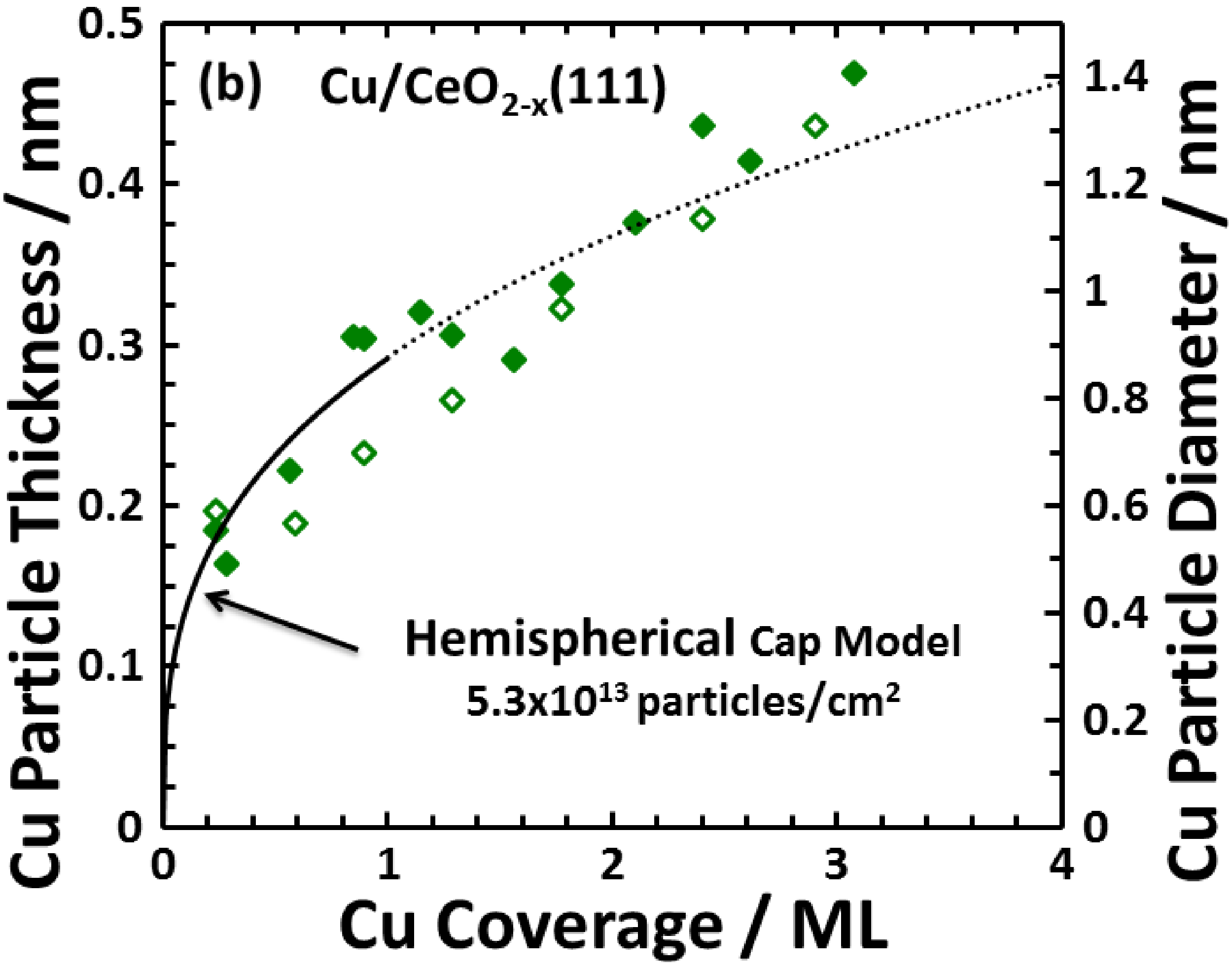

Figure 5.1(b): The average Cu particle thickness versus Cu coverage at 100 K calculated from these LEIS data points, and on the right axis, the average effective diameter of hemispherical caps that corresponds to this thickness. Also shown is the result expected for the same hemispherical-cap model and particle number density as used for the best fit to the data in part (a).

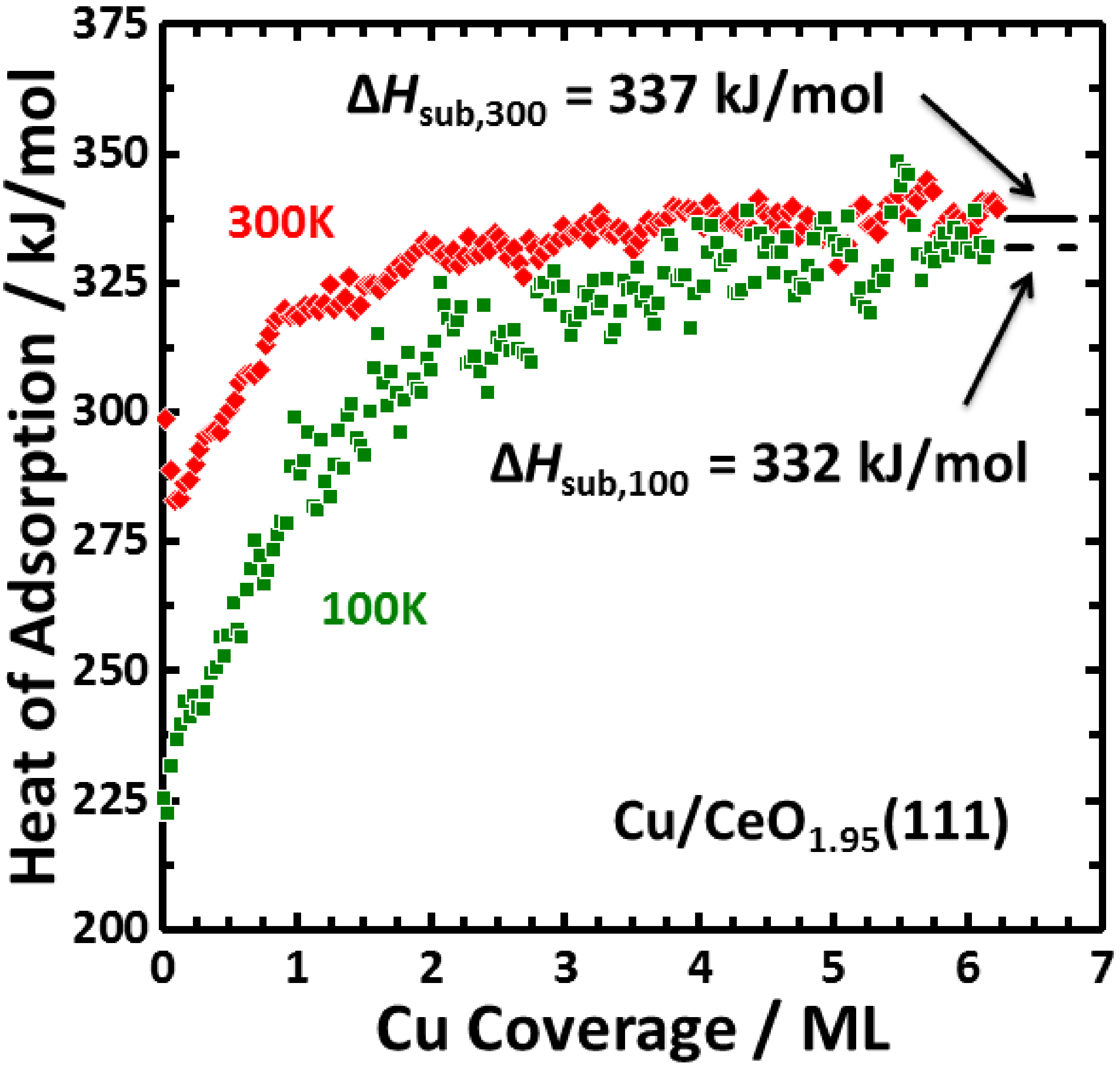

Figure 5.2: Cu atom heat of adsorption at 300K (diamonds, from [3]) and 100K (squares) on $CeO_{1.95}(111)$ as a function of Cu coverage.

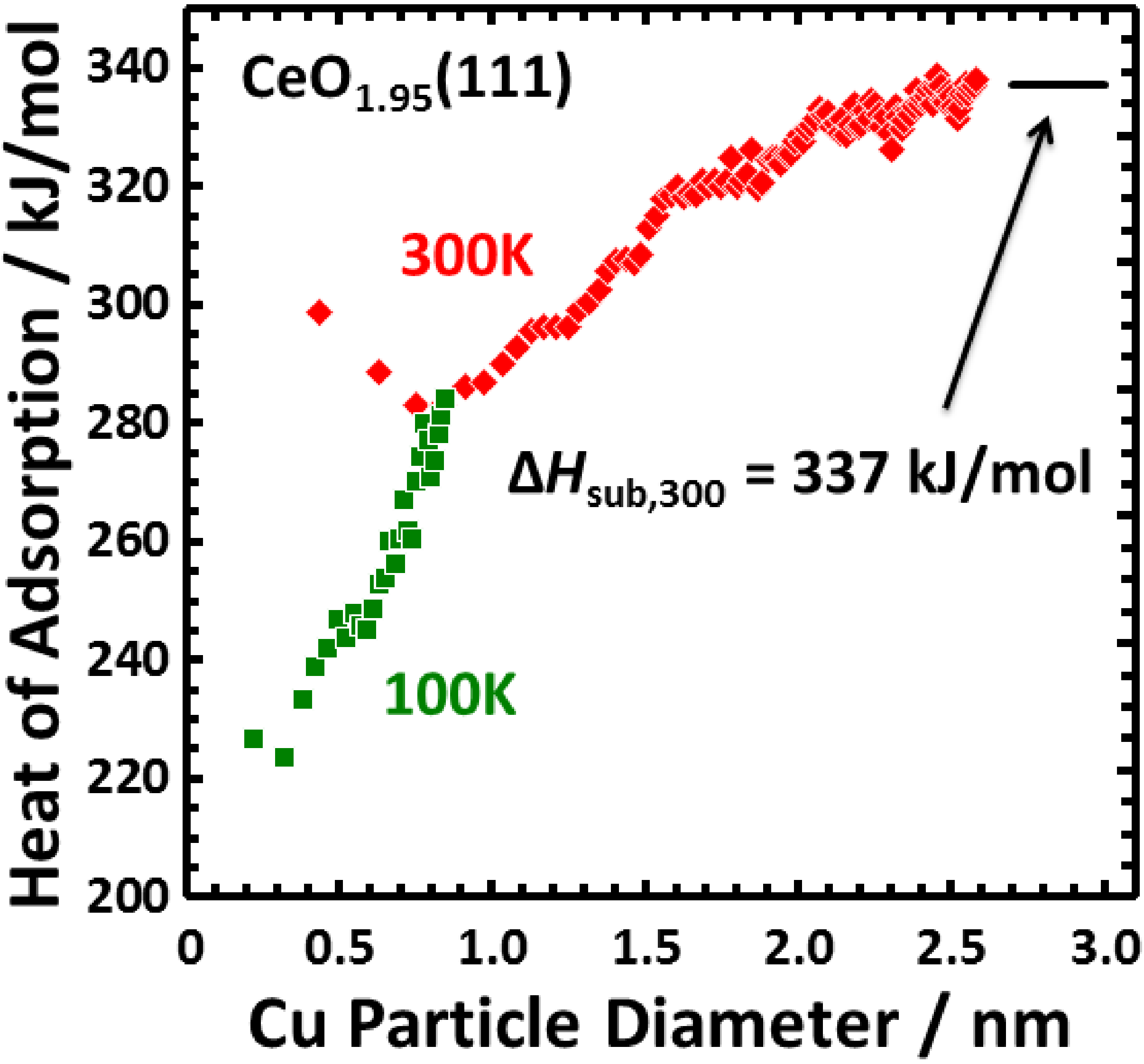

Figure 5.3: Cu atom heat of adsorption at 300 K (diamonds, from [3]) and 100 K (squares) on $CeO_{1.95}$(111) as a function of average Cu particles diameter after adsorption. The effective particle diameter was calculated using the total Cu coverage, assuming the nanoparticles grow as hemispherical caps with a constant particle density of 5.3×10^{13} particles/cm^2. The data at 300K and 100K was truncated at 35% total surface coverage to avoid heats when particles were agglomerating.

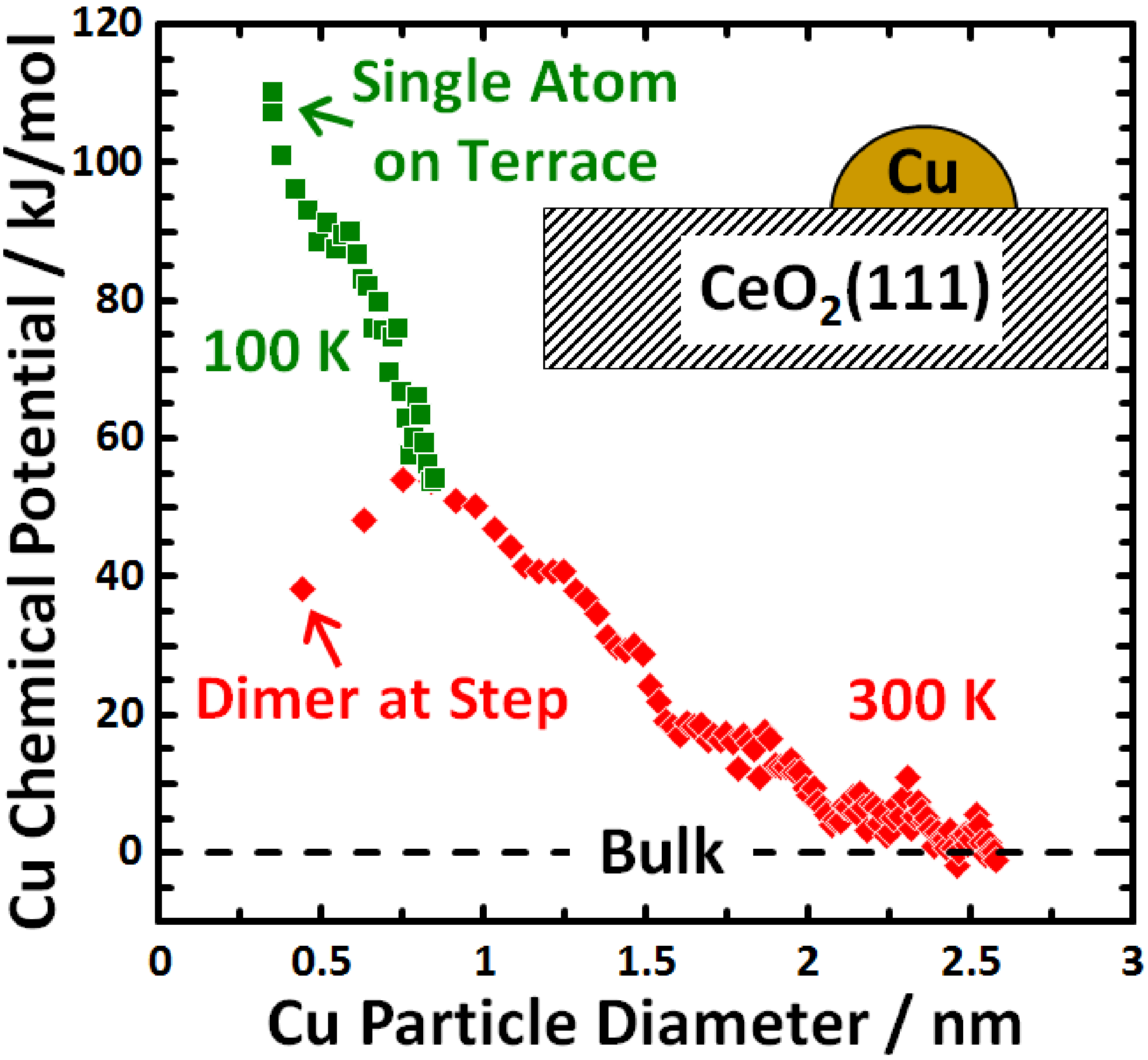

Figure 5.4: The chemical potential of Cu atoms in Cu nanoparticles on $CeO_{1.95}(111)$, relative to that in bulk Cu(solid), versus the effective diameter of the Cu particle, down to the single atom limit.

Chapter 6

Energetics of Au Adsorption and Adhesion onto Reduced CeO_2(111) Surfaces by Calorimetry

This Chapter contains unpublished results

The morphology and interfacial energetics of vapor-deposited Au on slightly-reduced CeO_2(111) surfaces at 100 and 300 K have been studied using single crystal adsorption calorimetry (SCAC), He^+ low-energy ion scattering spectroscopy (ISS), X-ray photoelectron spectroscopy (XPS), and low energy electron diffraction (LEED). Gold grows as 3-dimensional nanoparticles with a density ranging between 3 and 9×10^{12} particles/cm^2 on CeO_{2-x}(111) (where x = 0.05 and 0.2). A flat region in the LEIS growth of Au was observed which was attributed to either encapsulation by the strong-metal support interaction, or up-stepping of incoming Au atoms onto the top of existing Au nanoparticles. The initial heat of adsorption of Au increased with increasing degree of ceria reduction attributed to stronger binding to oxygen vacancies than stoichiometric sites. The initial heat of adsorption decreased with decreasing temperature on $CeO_{1.95}$(111), due to smaller, terrace bound nanoparticles being formed. The heat of adsorption under all conditions grows to the bulk Au heat of sublimation by 2 ML (2-3.6 nm diameter particles). For 3.6 nm diameter particles on $CeO_{1.95}$(111), the adhesion energy was found to be 2.53 J/m^2 and was 2.98 J/m^2 for smaller 2.6 nm diameter particles on $CeO_{1.8}$(111). The adhesion energy of metals to ceria was found to correlate well to previous trends determined for metal adhesion to MgO(100).

6.1. Introduction

Late transition metals supported on high surface area oxide supports form the basis for many important technologies such as catalysts, electrocatalysts, and chemical sensors. In catalysis, the interaction of the metal and the support has a strong influence on a variety of catalytic properties such as activity, selectivity, and long term stability. To better understand how the choice of metal and support can influence these catalytic properties, fundamental studies of common catalytic materials are needed. These studies generally involve metal atoms or particles dispersed across a well-ordered, atomically clean 2-dimensional supports where the types of interactions and nanoparticles size and number density can be precisely controlled.[6,8,20,103,145] Here we use that approach to study Au nanoparticles vapor deposited onto slightly reduced $CeO_2(111)$ where the extent of reduction and sample temperature are controlled.

We used single crystal adsorption calorimetry (SCAC) to study the energetics of Au atom adsorption. SCAC has been used for a variety of metal/oxide systems to directly measure the adsorption energy of metal atoms as they bind to the oxide surface, and to nanoparticles as they continue to grow.[3,10,12-14,104,105] Low energy ion scattering spectroscopy (LEIS) was used to monitor the growth and morphology of Au on $CeO_2(111)$. Combining adsorption energies with detailed information of particle morphology and growth, allow us to determine Au nanoparticle adhesion energies, which has been done for a variety of metal/oxide systems previously.[3,10,12-14] A thorough understanding of metal adhesion energies is important because it determines how quickly a catalyst will deactivate due to sintering. The adhesion energies here are compared to previously determined Cu and Ag adhesion energies to the same surface[3,10] and previously determined adhesion energy trends for metal adsorption to MgO(100).[105] These types of studies have also been used to determine the chemical potential of atoms in supported nanoparticles which effects their selectivity and reactivity.[10,146]

Gold supported on ceria has been extensively studied for a variety of important catalytic reactions such as the water gas shift reaction,[43] combustion of organic compounds,[147] and CO oxidation,[44] as well as many model systems used to explain the unusually high catalytic activity of nanoparticulate gold[148-150] which is surprising since bulk gold is relatively inert. Despite the extensive studies of this system, no experimental measurements about the strength of Au interfacial bonding to ceria have been reported. However, significant theoretical modelling, usually using density function based calculations, of this system has been performed which have given a variety of contradictory results.[151,152] To our knowledge, this is the third detailed structure/energetic study of metal adsorption onto $CeO_2(111)$ which were our previous reports for Ag[10,14] and Cu[3,146] adsorption.

6.2. Results

6.2.1 $CeO_{2-x}(111)$ thin film characterization.

Thin films of $CeO_{2-x}(111)$ (where x = 0.05 and 2) were grown to a thickness of 4-6 nm on a 1 μm thick Pt(111) substrate as described previously.[3,14] It has been shown for Ag adsorption on $CeO_{2-x}(111)$ that film thicknesses above 2 nm result in bulk-like ceria surface properties for Ag adsorption energies.[14] The (111) surface order was verified by LEED which gave a sharp (1x1) pattern. The $CeO_{2-x}(111)$ film thickness was calculated by the attenuation of the Pt $4p_{3/2}$ XPS peak and the oxidation state of these ceria films was determined from the relative contributions of Ce^{3+} and Ce^{4+} to the Ce 3d region in XPS. A detailed description of $CeO_2(111)$ film growth can be found in Refs.[3,14].

6.2.2 Au sticking probability on $CeO_{2-x}(111)$.

The sticking probability of Au on $CeO_{2-x}(111)$ as a function of total Au coverage was calculated by monitoring the number of non-sticking Au atoms in each pulse. This was measured by comparing the magnitude of a time-integrated transient QMS signal during each calorimetry pulse to a zero-sticking reference signal that was generated by placing a hot Ta foil flag in the sample position and resistively heating it so that all incoming atoms rapidly desorb. The sticking probability measured was >0.99 at all Au coverages on both the oxidized (x=0.05) and reduced (x=0.2) ceria films at 300 K and 100 K.

6.2.3 Au morphology on $CeO_{2-x}(111)$ at 300 K.

The Au nanoparticle morphology on $CeO_{2-x}(111)$ at 300 K was determined using He^+ LEIS as shown in Fig. 6.1(a). Discreet quantities of Au were deposited using same series of apertures as those used in calorimetry, and both the attenuation of the substrate signal and the growth of the adsorbate signal were monitored as a function of total Au coverage. The Ce data were normalized to the integrated Ce peak area from the clean film prior to Au deposition, and the Au data were normalized to a thick, bulk-like Au overlayer (>60 ML). Since LEIS is sensitive only to the topmost atomic layer, the Au and Ce signal are a direct measurement of the fraction of the ceria surface that is masked or unmasked by Au nanoparticles. Since the normalized Au signal does not decrease at any Au coverage it indicates that Au forms a surface layer, and does not diffuse into the ceria surface. The data in Fig. 6.1 are compared to both the layer-by-layer growth model and the hemispherical cap growth model described by Diebold et al.,[21] which was later modified to better describe the macroscopic shadowing by hemispherical particles.[108] This model has been used to describe the morphology of many oxide-supported late-transition metals relevant to catalysis.[9] In the case of Au (Fig. 6.1) the data deviate markedly from the layer-by-layer model, indicating that Au does not grow two-dimensionally at any coverage.

As in the case of previously studied group-13 metals supported on CeO(111),[3,14] the data are well fit using this modified hemispherical cap model. For Au growth at 300 K, a least squares analysis gave a particle density of 2.8×10^{12} particles/cm^2 on $CeO_{1.95}(111)$ and twice as large, 5.4x10^{12} particles/cm^2, on $CeO_{1.8}(111)$, which is in good agreement with STM results by Lu et al.[115] The LEIS data were fit up to ~35% total Au surface coverage, at which point the model breaks down due to particles overlap. Interestingly, the normalized LEIS signal on $CeO_{1.8}(111)$ flattens between ~2 and 5 ML indicating Au does not grow as hemispherical caps in this region.

The normalized LEIS signal shown in Fig. 1(a) directly measures the fraction of the ceria surface that is masked by Au particles at any given coverage. If we assume that the footprint of the Au particles is expanded due to macroscopic shadowing by $((1 + 1/\cos\theta_i)/2 = 1.207)$,[108] which is the case for the Au growth studied here, we can divide the normalized LEIS signal by 1.207 to estimate the actual fraction of the $CeO_{2-x}(111)$ surface that is covered by Au nanoparticles and not just shadowed. Since we know the average film thickness from the Au coverage, we can divide by this value to give the average thickness of Au nanoparticles assuming they have the same density as bulk Au(solid). Fig. 6.1(b) shows the data in Fig. 6.1(a) replotted in this way. Additionally, since the average thickness of a hemispherical cap is 1/3 its diameter, this thickness is multiplied by 3 on the right-hand axis to show the corresponding average particle diameter. The expected average particle thickness and diameter from the best fit number density of the hemispherical cap is shown for reference, the agreement is excellent except for where the data flattens on $CeO_{1.8}(111)$ which indicates the average particle thickness is growing faster than predicted by the model suggesting that these particles deviate from the hemispherical cap shape and begin to grow taller faster than they grow laterally across the surface.

To ensure no ion-beam damage in Figure 6.1(a), a growth experiment was performed with only two Cu coverages (1 and 2 ML), giving much less total ion beam exposure up to 2 ML. These data fell within error of Figure 6.1(a), indicating that no ion-beam damage occurred.

6.2.3 Au morphology on $CeO_{2-x}(111)$ at 100 K.

The growth of Au on slightly $CeO_{2-x}(111)$ at 100K was also monitored by LEIS which should reduce the Au particle mobility and the results presented in Fig. 6.2(a). The least squares best fit Au particle density on $CeO_{1.95}(111)$ was $7.8x10^{12}$ particles/cm^2, which is ~3 times higher than at 300 K and $8.9x10^{12}$ particles/cm^2 on $CeO_{1.8}(111)$ which is ~2 times greater than at 300 K. This increase in particle density from oxidized to reduced ceria surface at 100 K is much smaller than the difference observed between the two ceria surfaces at 300 K. The data also did not flatten on CeO(111) as it did at 300 K. Calorimetry data for Au on $CeO_{1.8}(111)$ is not presented here as it was qualitatively very similar to Au on $CeO_{1.95}(111)$ at 100 K, and the difference in the best fit particle density was small indicating very similar adsorption properties for these systems. The data are again replotted in Fig. 6.2(b) as a function of average particle thickness and diameter as explained above

6.2.4 Au Adsorption and Adhesion Energies on $CeO_{2-x}(111)$

Figure 6.3 shows the Au heat of adsorption onto slightly reduced $CeO_2(111)$ at 300 and 100 K. All heats have been corrected for the difference between hot atoms at the source temperature and the same collection of atoms in a Boltzmann distribution at the sample temperature (either 300 K or 100 K) as has been described previously.[17] Data presented this way correspond to the standard enthalpy of adsorption at the temperature of the sample (times negative one, as exothermic heats are presented as positive, which is the convention for calorimetry).

At 300 K, the initial heat of adsorption of Au on $CeO_{1.8}(111)$ is 296 kJ/mol, which is 37 kJ/mol larger than the initial heat on $CeO_{1.95}(111)$ (259 kJ/mol). As coverage increases, the Au heat of adsorption increases at a qualitatively similar rate on both surfaces as the average number of more favorable Au-Au bonds per incoming is formed, with the heat of adsorption higher the more reduced surface until ~2 ML, where both systems converge to the bulk heat of sublimation of Au(solid) (368 kJ/mol at 300 K[9]). Similar behavior was observed for Ag on $CeO_{2-x}(111)$, and this difference was attributed to stronger binding to oxygen vacancies, which have a higher number density on a more reduced ceria surface.[14] At 100 K, Au adsorbs on $CeO_{1.95}(111)$ with an initial heat of adsorption of 210 kJ/mol (86 kJ/mol lower than at 300 K) and increases rapidly with coverage until it approaches the standard Au(solid) bulk heat of sublimation of (363 kJ/mol at 100 K[9]), also by ~2 ML. The lower initial heat of adsorption of Au on $CeO_{1.95}(111)$ at 100 K compared to 300 K is partially due to the formation of smaller particles at lower temperatures, but it is also likely due to a higher fraction of Au atoms adsorbing to terraces compared to step sites, which are more energetically favorable than terrace sites due to the formation of more nearest neighbor bonds.

Since the average Au particle diameter can be calculated from the total Au coverage as in Fig 6.1(b) and Fig. 6.2(b), the heat of adsorption in Fig. 6.3 can be replotted as a function of average Au particle diameter as shown in Fig. 6.4. When plotted this way, the Au heat of adsorption reaches the Au bulk heat of sublimation for ~3.2 nm diameter particles on $CeO_{1.95}(111)$, and ~2.4 nm diameter particles on $CeO_{1.8}(111)$. At 100 K the lower initial heat of adsorption corresponds to smaller Au particles being formed indicating the smallest particles are the most weakly bound to the ceria surface. The heat of Au adsorption at 100 K on $CeO_{1.95}(111)$ is lower for all particles sizes below ~1.5 nm than on the same surface at 300 K, until it crosses over the heats measured at 300 K, reaching the Au heat of sublimation by ~2.0 nm particles.

The adhesion energy of nanoparticles onto a flat surfaces, E_{adhesion}, can be calculated from the following relationship:[9]

$$n\cdot\sum_n \Delta H_{\mathrm{adsorption}} = -n\cdot\Delta H_{\mathrm{sublimation}} + A\cdot[(1+f)\gamma_{\mathrm{v/m}} - E_{\mathrm{adhesion}}]$$

where $\gamma_{\mathrm{v/m}}$ is the surface free energy of the bulk nanoparticle material, f is the surface roughness factor (f =2 for a hemispherical cap), $\sum_n \Delta H_{\mathrm{adsorption}}$ is the integral (average) molar heat of adsorption up to the coverage (particle size) of interest, n is the number of moles of the adsorbate on the surface at that coverage, A is the total area covered by the metal nanoparticles, and $\Delta H_{\mathrm{sublimation}}$ is the bulk heat of sublimation of the adsorbate. Using this method requires that the adhesion energy is calculated at the point where no more than ~35% of the surface is covered by the adsorbate (as determined by LEIS) to ensure that there is no significant particles overlap. The adhesion energy of 3.6 nm Au nanoparticles on $CeO_{1.95}(111)$, is 2.53 J/m^2. On $CeO_{1.8}(111)$ surface, the adhesion energy of 2.6 nm particles is 2.98 J/m^2, which is larger than for the oxidized surface despite the smaller particle size. This shows the enhanced strength of Au bonding to the more reduced surface indicating Au prefers to bind to oxygen vacancies. The Au adhesion energy to reduced $CeO_2(111)$ is substantially higher than to MgO(100) (0.67 J/m^2), which was measured using contact-angle analysis in HRTEM.[105] Additionally, the value of adhesion energy between Au nanoparticles and $CeO_{1.95}(111)$ is higher than the value of 2.3 J/m^2 for Ag nanoparticles on this same surface,[10] but lower than the value for Cu on $CeO_{1.95}(111)$, which was 3.52 J/m^2.[3]

6.3. Discussion

Au particles have been shown to grow as hemispherical caps on $CeO_{2-x}(111)$ at both 300 an 100K by STM[115] and TEM,[153] consistent with our LEIS and XPS observations that Au grows as hemispherical caps at both 300 K and 100 K. At 300 K, Au was shown to adsorb primarily to step sites on stoichiometric $CeO_2(111)$.[115] When $CeO_2(111)$ films were reduced by growing in reduced oxygen pressure[115] and thermal annealing,[141] a larger fraction of Au particles nucleate on terraces than steps and result in an increased particle density compared to stoichiometric CeO_2(111). On the (111) ceria surface, oxygen vacancies are expected to be the primary point defects, rather than cerium vacancies since they are easier to form energeticallly.[154] We approximate the step density of our as prepared films to be ~5%, and that the steps on $CeO_{1.8}$(111) are likely missing all of their O atoms, whereas on the $CeO_{1.95}$(111) surface, about half are still present as discussed previously.[3] Since the step edge density is the same for both films, the increased particle density on the more reduced films is due to Au adsorption at surface oxygen vacancies, which is indeed what has been reported previously.[115] Therefore, the 37 kJ/mol difference in heat of adsorption on the two ceria surfaces at 300 K can be due to Au bonding more strongly to more oxygen deficient step edges and/or Au bonding more strongly to terrace oxygen vacancies than the partially oxygen deficient step edges on $CeO_{1.95}$(111). In our data, we cannot differentiate between the two sites, however, since our heat of adsorption at 100 K is lower for similarly sized particles on $CeO_{1.95}$(111), than at 300 K for the smallest sized particles, and these particles have a higher fraction nucleated on terraces,[141] we postulate that terraces, even when containing oxygen vacancies, are slightly less favorable thermodynamically, but act as a kinetic trap for incoming Au atoms.

Our calorimetry results agree qualitatively with DFT+U calculations despite the exceptional challenge in modeling Au and CeO_2(111) due to the choice of the exchange correlation functional, and has produced several contradictory results, many of which are summarized in two excellent reviews.[151,152] Zhang et al.[119] found that Au adsorption at an O-vacancy (2.75 eV) was roughly double that of the adsorption at the most stable stoichiometric O-O bridge site (1.17 eV). Similar two-fold increases in the binding energy at oxygen vacancies compared to the most stable stoichiometric site were found by Hernandez et al.[155] and Camellone and Fabris.[118] The largest difference comes from Chen et al.,[120] who found that Au binding at a surface oxygen vacancy was just slightly less than three times larger than at a stoichiometric O-top site.

Comparatively little work has been done computationally comparing the adsorption energy of Au adatoms at oxygen vacancies to the binding at step sites. Castellani et al.[156] have attempted to investigate such defects by building a model that incorporates both concave and convex step morphology. For most model sites, they found that Au adsorption energies were in the range of 0.52-0.69 eV compared to 0.51-0.66 eV at stoichiometric sites, which is a negligible difference (it is worthwhile to note that these values are lower than those produced by other models for Au on planar ceria surfaces due to the particular methodology employed). However, one of the proposed active sites that involves a concave facet intersecting the (111) gave an Au adsorption energy that was three to four times higher (~2.36 eV) than the above values.

As noted above, both the Au and the Ce signal in LEIS flatten at 1.7 ML ± 0.2 ML (average of 3 experiments) on the $CeO_{1.8}(111)$ at 300 K, with the variation likely the result of a small difference in precise number density of surface oxygen defects for each ceria film preparation. This flattening effect was *not* observed when Au was deposited on $CeO_{1.8}(111)$ at 100 K. We propose two possible explanations for this observation. First, flattening of the LEIS signal indicates a thickening of the Au particles as shown in Fig 6.1(b) without growth laterally across the ceria surface. A small increase in Au LEIS signal is expected since the taller particles would shadow ceria substrate more. This would indicate that incoming Au atoms prefer to nucleate on top of an existing Au particle rather than binding at the Au/ceria interface which is expected since Au-Au bonds are more favorable than Au-ceria bonds as demonstrated by the increase in heat of adsorption with coverage. This requires Au atoms that do not land on an existing Au particle to diffuse to the Au-ceria interface and step up the particle. This is supported by the fact that the same flattening is not observed at 100 K on $CeO_{1.8}$(111), meaning there is a kinetic barrier for up stepping which is blocked at lower temperatures.

Presumably, Au particle thickening takes place when all the available step and oxygen vacancy sites have been saturated, leaving only stoichiometric terraces. Therefore, the adsorption energy to terraces in the more reduced film are chemically different than the more oxidized film. Zhang et al.[154,157] found that the formation of an oxygen surface and subsurface oxygen vacancy was only 0.1 eV, indicating these types of defects should have nearly equivalent concentrations. This was confirmed in the elegant STM work of Esch et al.,[158] where both single surface and subsurface vacancies were present with similar concentrations on slightly reduced CeO_2(111). However, further reduction of the film caused vacancy clusters to appear, primarily as linear chains and triangular O-vacancy trimers which required subsurface vacancies to nucleate the linear chains, and are often part of the observed surface clusters. This clustering effect suggests that in our $CeO_{1.8}$(111) films, oxygen vacancies are likely clustered on the surface which may be more stable adsorption sites than single vacancies. Additionally, if our ceria surfaces contain primarily vacancy clusters, there are probably few isolated subsurface oxygen vacancies. Esch et. al.[158] found that direct diffusion of vacancies (i.e. hopping of lattice oxygen) requires temperatures higher than 400°C. Since we anneal our reduced surfaces after growth to temperatures well above 400°C, this may be facilitating the agglomeration of subsurface vacancies into large clusters with surface vacancies. These isolated subsurface vacancies, which should be present in $CeO_{1.95}$(111) may prevent Au from stepping up to the top of existing Au particles at room temperature.

Alternatively, Akita et al.[153,159] found in TEM that 3-5 nm Au particles on CeO_2 shrank one layer at a time with no significant change in the contact diameter until only a single atomic layer remained. When the sample was not irradiated by electrons, the nanoparticles recovered their original shape, nucleated at the same position, and this process occurred reversibly through multiple cycles. This was also independently observed by Majimel et al.,[160] but this effect has not seen for Au supported on any other oxide likely due to oxygen vacancies being energetically easy to generate and replenish compared to other reducible oxides. Therefore, it was proposed that Au atoms from nanoparticles spread out over the surface to the oxygen vacancies. This is reversible as oxygen is replenished by residual gas in the vacuum chamber, this is supported by monitoring the Ce-M edge in electron energy-loss spectroscopy.[153] During this shape cycling, TEM, and EELS revealed the presence of Ce on top of Au particles, suggesting that these particles have become partially encapsulated by the well-known as the SMSI effect[161] which has also been observe for Pt and Rh on CeO_2.[162] Encapsulation of Au would also cause the Au LEIS signal to flatten and may only be observed when the ceria is sufficiently reduced. Unfortunately, the oxygen signal in LEIS is too small to determine if there is a loss of oxygen during growth studies which we would expect if the surface is becoming more reduced.

The adhesion energy of Au to $CeO_{1.95}(111)$ is larger than the adhesion of Ag[10] and smaller than the adhesion of Cu[3] to the same surface which is not in agreement with DFT by Illas et al.,[38] but agrees with metal adhesion energy trends to MgO(100).[105] As discussed above, Au and $CeO_2(111)$ are difficult to model by DFT which is likely the cause of the deviation between experiment and theory. If we plot the metal adhesion energy in the same way as in Ref.,[105] which found adhesion energy correlates by $[(\Delta H_{sub,M} - \Delta H_{f,MOx})N_A]/\Omega_M^{2/3}$, where $\Delta H_{sub,M}$ the heat of sublimation of the metal, $\Delta H_{f,MOx}$ is the heat of formation of the metal's most stable oxide, N_A

is Avogadro's number, and $\Omega_M^{2/3}$ is the are per metal atom. When plotted this way, our metal adhesion energies are also correlated by this relationship with a similar slope but offset by 2.1 J/m^2, as shown in Fig. 6.5. We also tried to correlate adhesion energy to the strength of the metal-oxygen bond, which is more descriptive of bonding occurring at the surface, but found the correlation was poor in this case. The observed trends in adhesion energy should be applicable for metal adsorption to other oxides, and offer a predictive trend in determining adhesion energy. It is important to note, adhesion energies onto CeO_2(111) reported in Fig. 6.5 are all for hemispherical cap shaped particles at 35% surface coverage for consistency meaning the adhesion energy was calculated for different particle sizes.

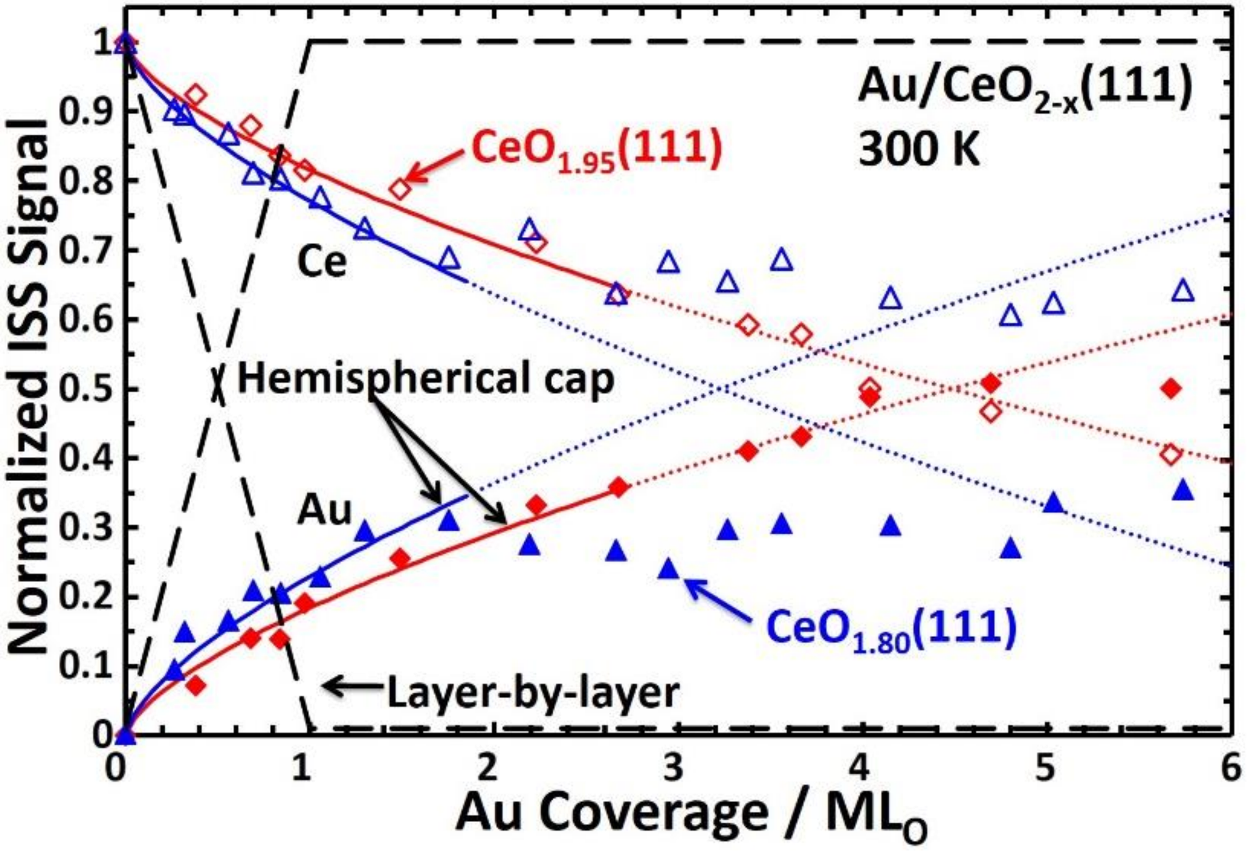

Figure 6.1(a): Integrated LEIS signal intensities for Au (closed symbols) and Ce (open symbols) as a function of total Au deposited onto $CeO_{1.95}(111)$ (red diamonds) and $CeO_{1.80}(111)$ (blue triangles) at 300 K normalized to thick multilayer Au and clean $CeO_{2-x}(111)$ respectively. The dashed line corresponds to the normalized LEIS signal expected from a layer-by-layer growth mechanism while the solid lines correspond to Au growing as hemispherical caps with a fixed particle density of 2.8x10^{12} particles/cm^2 on $CeO_{1.95}(111)$ and 5.4x10^{12} particles/cm^2 on $CeO_{1.80}(111)$. This model only holds up the point where ~35% of the surface is covered by Au particles as they may start to overlap at that point, and above that point, the data on the oxidized surface follows this curve while the data on the reduced surface "flattens" above this point. The dotted lines are shown to guide the eye.

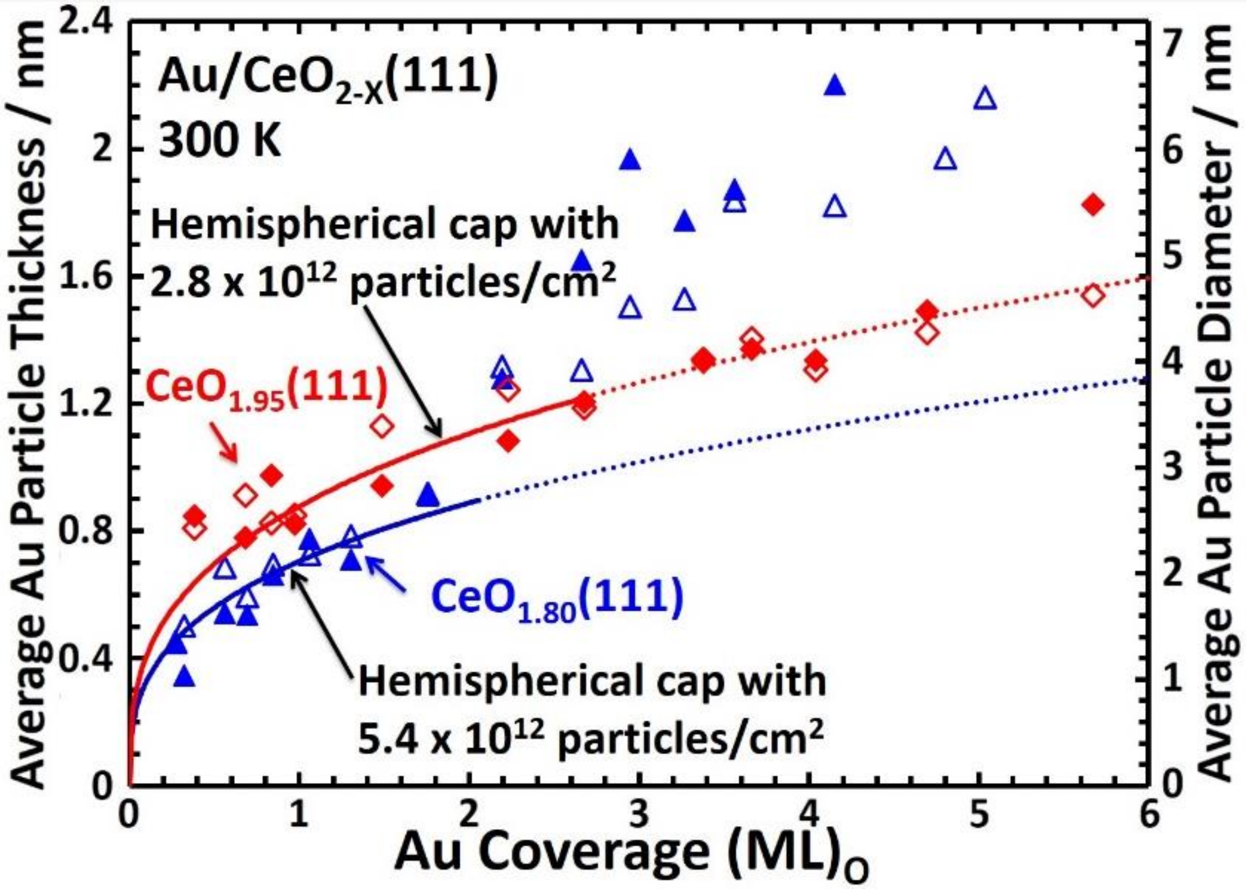

Figure 6.1(b): Average Au particle thickness (right axis) and the average Au particle diameter of hemispherical caps that corresponds to this thickness (left axis) plotted versus Au coverage for both the more oxidized $CeO_{1.95}(111)$ surface (red diamonds) and the more reduced $CeO_{1.80}(111)$ surface (blue triangles). These values are calculated using both the Au (closed) and the Ce (open) LEIS data shown in Fig. 1(a). The curves shown are the expected result from the same hemispherical-cap model and particle number density as used for the best fit to the data in part (a), and using this method the average particle thickness on the reduced surface grows much faster than predicted by the model, suggesting that these particles are growing predominantly more vertically than hemispherical caps would.

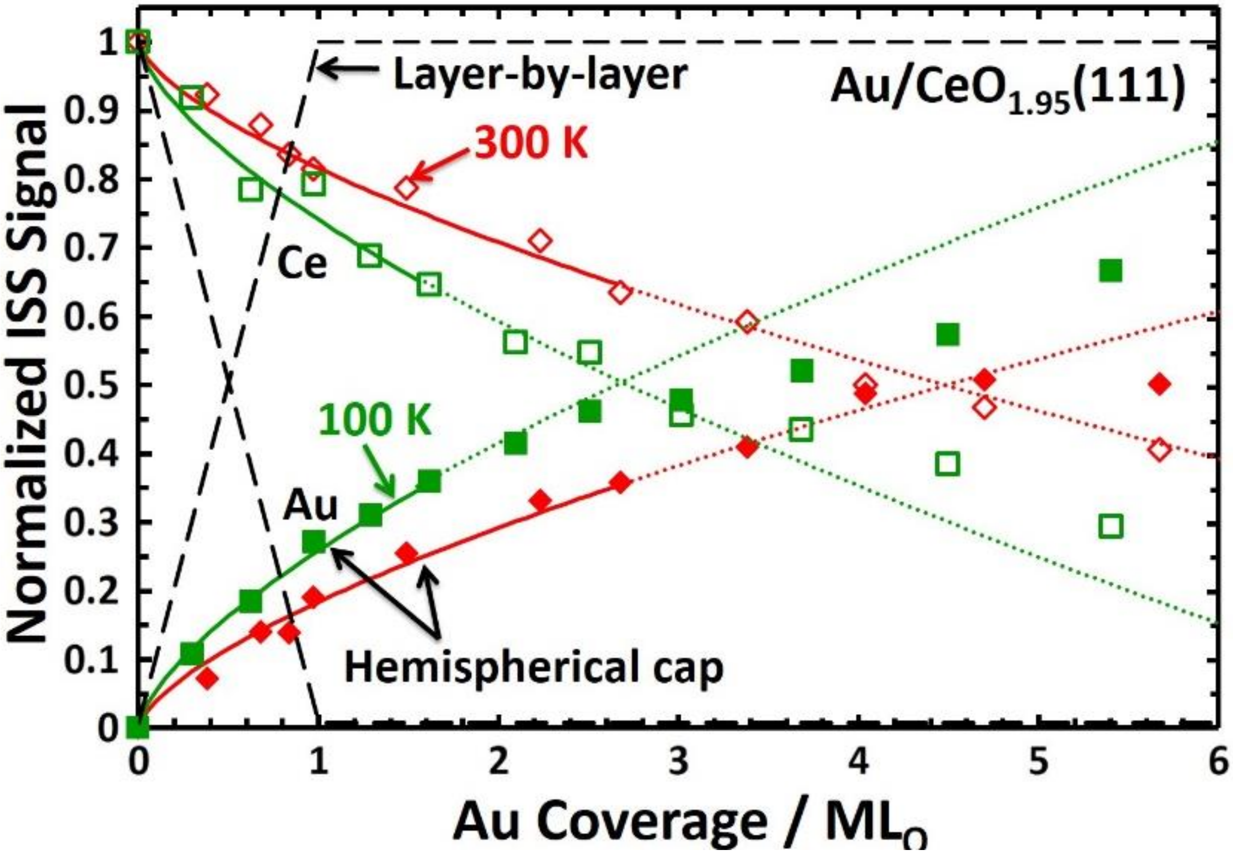

Figure 6.2(a): Integrated LEIS signal intensities for Au (closed symbols) and Ce (open symbols) as a function of total Au deposited onto $CeO_{1.95}$(111) at 300 K (red diamonds) and at 100 K (green squares) normalized to thick multilayer Au and clean CeO_{2-x}(111). The dashed line corresponds to the normalized LEIS signal expected from a layer-by-layer growth mechanism while the solid lines correspond to Au growing as hemispherical caps with a fixed particle density of 2.8×10^{12} particles/cm^2 at 300 K and 7.8×10^{12} particles/cm^2 at 100 K. The dotted lines above ~35% surface coverage are shown to guide the eye.

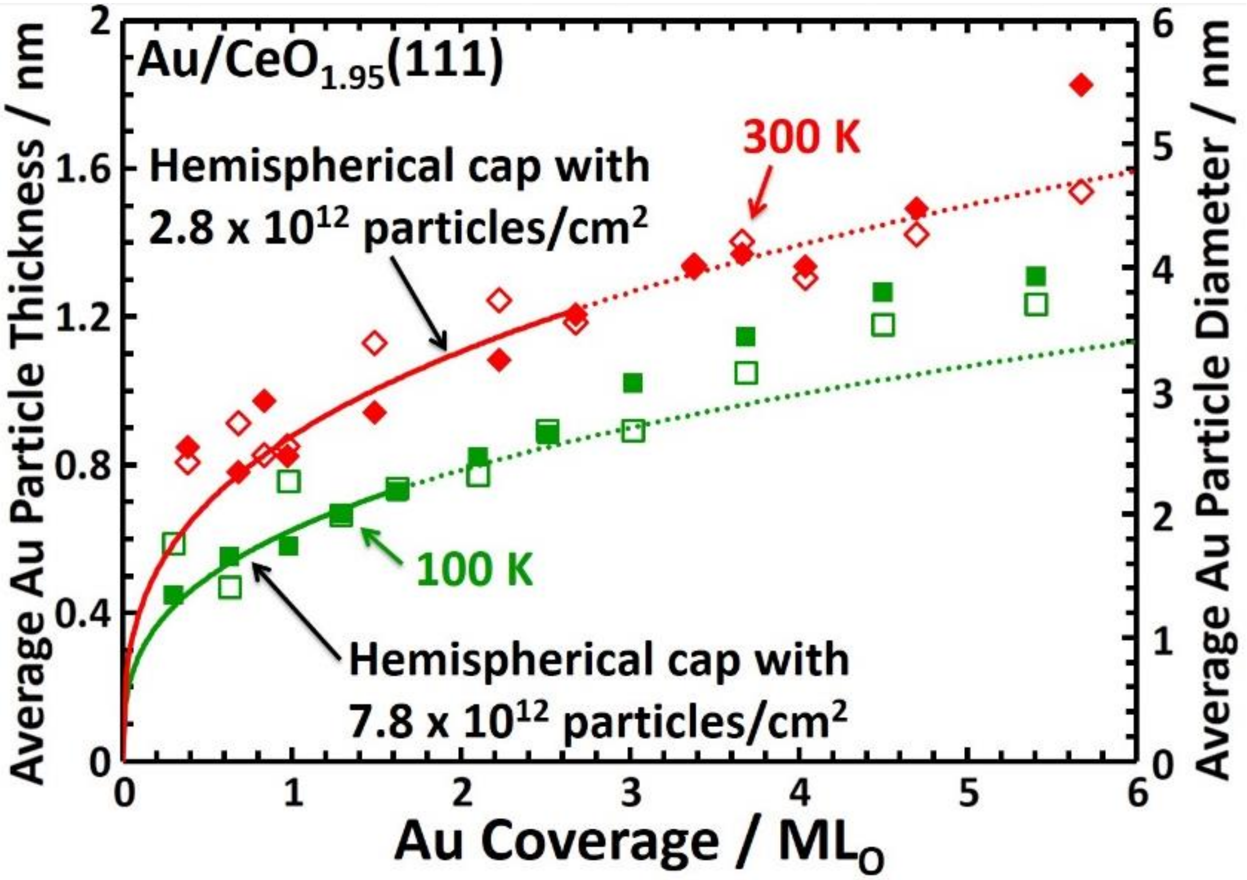

Figure 6.2(b): Average Au particle thickness (right axis) and the average Au particle diameter of hemispherical caps that corresponds to this thickness (left axis) plotted versus Au coverage on $CeO_{1.95}$(111) at 300 K (red diamonds) 100 K (green squares). These values are calculated using both the Au (closed) and the Ce (open) LEIS data shown in Fig. 2(a). The curves shown are the expected result from the same hemispherical-cap model and particle number density as used for the best fit to the data in part (a).

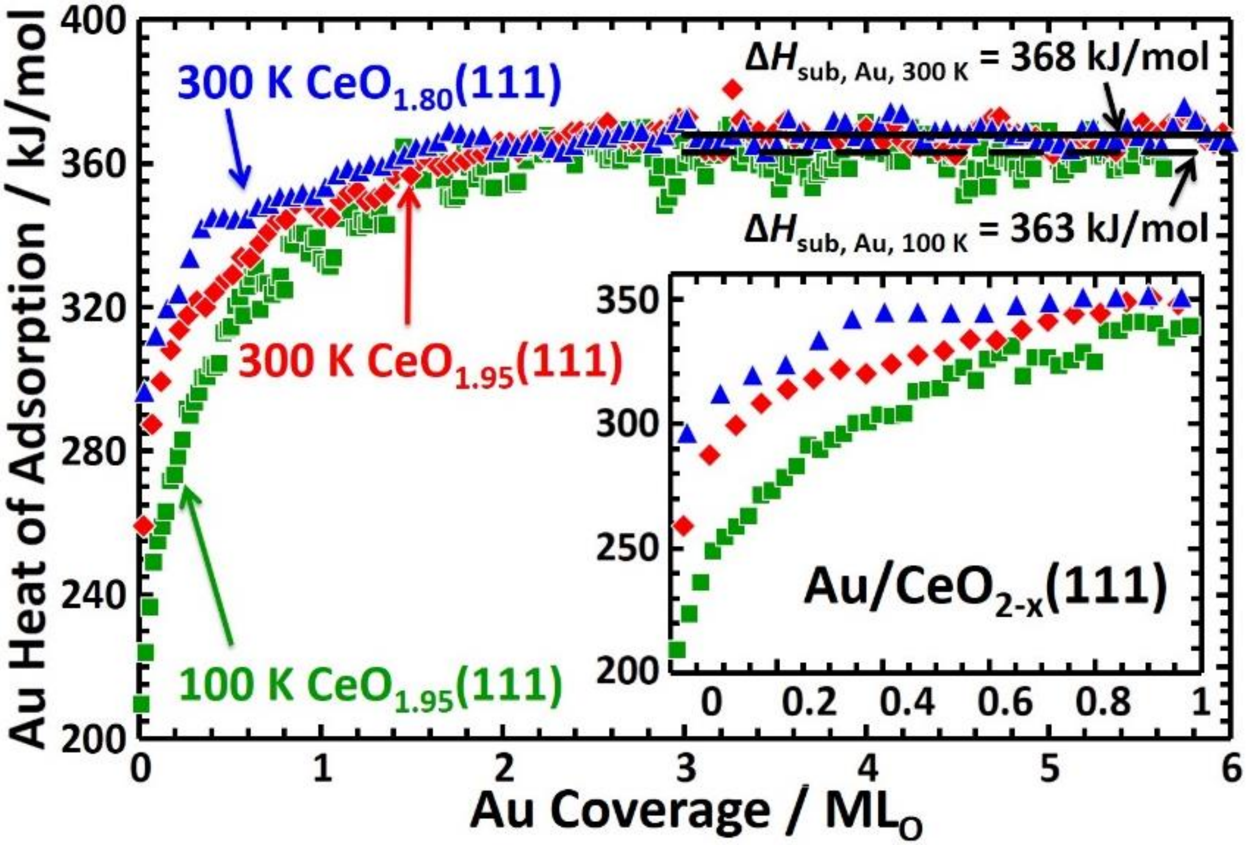

Figure 6.3: Heat of Au atom adsorption on $CeO_{1.95}(111)$ at 300 K (red diamonds) [average of 5 experiments], $CeO_{1.80}(111)$ at 300 K (blue triangles) [average of 3 experiments] and $CeO_{1.95}(111)$ at 100 K (green squares) [average of 3 experiments] as a function of total Au coverage (1 ML_O = 7.89×10^{14} atoms/cm^2). The inset shows these same data from 0-1 ML_O where they change most rapidly.

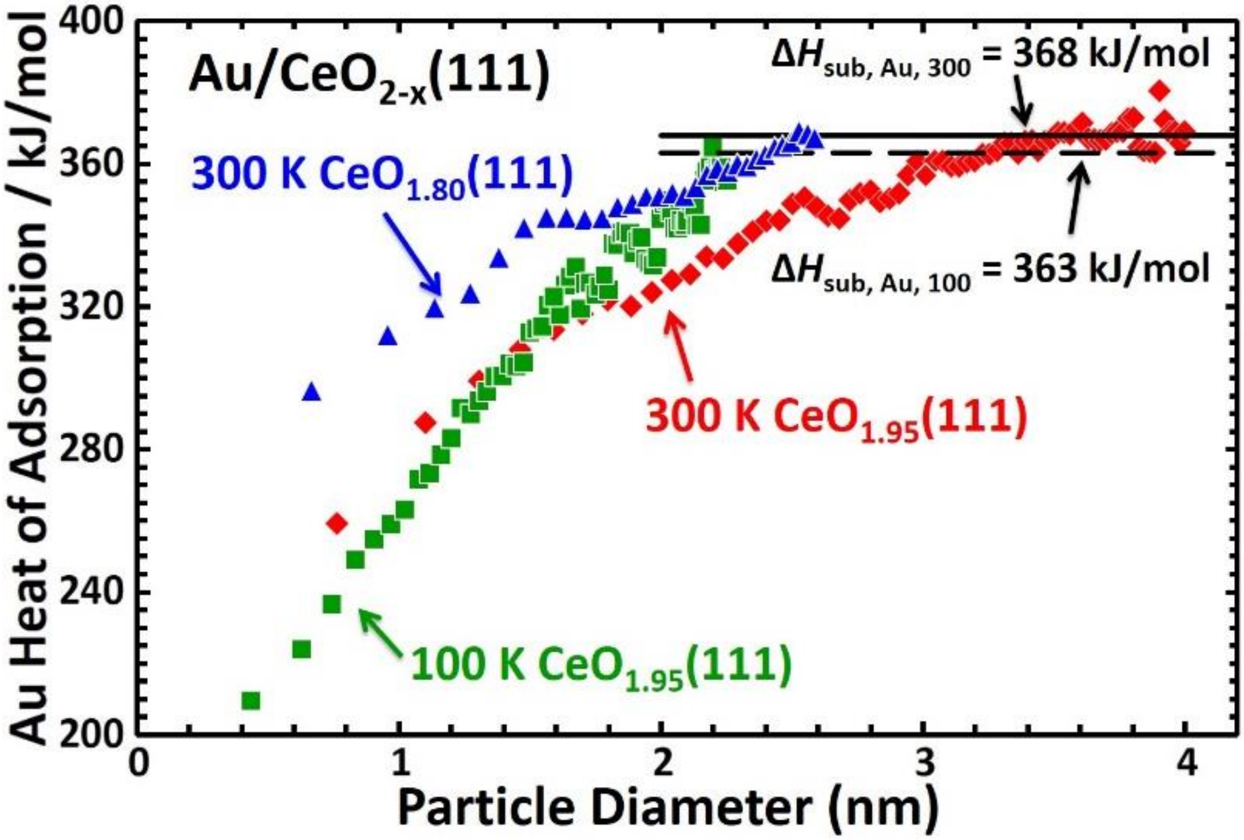

Figure 6.4: Heat of Au atom adsorption on $CeO_{1.95}(111)$ at 300 K (red diamonds) [average of 5 experiments], $CeO_{1.80}(111)$ at 300 K (blue triangles) [average of 3 experiments] and $CeO_{1.95}(111)$ at 100 K (green squares) [average of 3 experiments] as a function of the average Cu particle diameter to which Au atoms add.

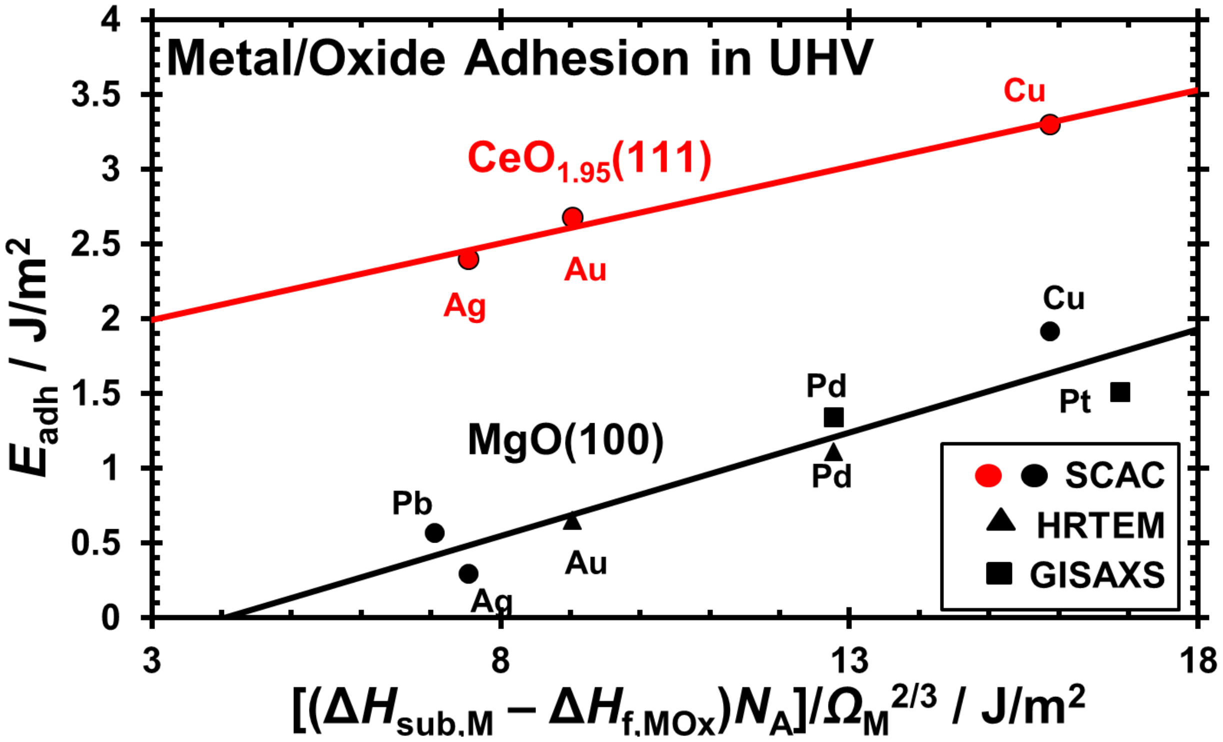

Figure 6.5: Adhesion energies of different metals on MgO(100) (black) and $CeO_2(111)$ (red) plotted verus the bulk metal's sublimation enthalpy minus the heat of formation for the metals most stable oxide divided by the are per metal atom. Data for CeO2(111) was all determined calorimetrically (circles), while on MgO(100) is was a combination of calorimetry, HRTEM (triangles) and GISAXS (squares). The lines through the data sets are best linear fits.

Chapter 7

Calorimetric Measurement of Adsorption and Adhesion Energies of Cu on Pt(111)

This Chapter contains unpublished results

The interfacial energetics of vapor deposited Cu onto Pt(111) at 300 K has been studied using single crystal adsorption calorimetry (SCAC), X-ray photoelectron spectroscopy (XPS), and low energy ion scattering spectroscopy (LEED). The heat of adsorption decreased linearly over the first monolayer showing Cu adsorbs more strongly to Pt step edges than Cu step edges. The heat of adsorption continued to decrease until 2.5 ML to 333 kJ/mol as Cu adsorbed to a strained Cu overlayer more weakly than it would to Cu(bulk) and showed that Cu-Cu bonds are less energetically favorable than Cu-Pt bonds. The heat of adsorption then increased to and remained constant at the Cu(bulk) heat of sublimation by 3 ML. The adhesion energy of Cu onto Pt(111) decreased as the Cu film became thicker between 1 and 4 ML from 3.84 to 3.76 J/m^2. The heat of adsorption was benchmarked to previous experimental and theoretical results to determine how differences in the adsorption energy arise.

7.1 Introduction

Bimetallic catalysts often have physical, chemical, electronic, and catalytic properties unique from their individual parent metals[46,47] and thus make promising materials to be used as catalysts[163] and electrocatalysts.[164] In order to understand how the choice of metal influences catalytic properties, a variety of detailed surface science studies have been performed where the system structure, the total concentration of each metal, and cleanliness of the system can be controlled.[6,45,165] Fundamental studies of this type can help lead to the production of more efficient, environmentally friendly catalysts. Studies of this type using bimetallics consisting of well-ordered Cu overlayers on Pt(111) have been studied extensively in the past for their unique adsorption and catalytic properties of small molecules such as oxygen,[51] CO,[48,166] CO_2,[49,167] and formate[50] to name a few.

To gain insight into these unique adsorption properties, we use the same model catalyst approach here to study the adsorption and adhesion energies of Cu vapor deposited onto clean, well-ordered Pt(111) at 300K by single crystal adsorption calorimetry (SCAC). We interpret these adsorption energies in light of detailed morphological studies of vapor deposited Cu onto Pt(111). This is only the second bimetallic system adsorption directly measured by SCAC.[63] Adsorption energies of Cu onto other transition metals have been previously been reported using temperature programmed desorption (TPD), but could not be measured for Cu since annealing causes Cu/Pt to alloy.[168-171]

The growth of Cu on Pt(111) at 450 K has been studied in detail by Auger electron spectroscopy (AES),[172,173] low energy electron diffraction (LEED),[172,173] thermal desorption spectroscopy (TDS) of H_2 and CO,[172,173] and scanning tunneling microcopy (STM).[174] Cu grows layer-by-layer on Pt(111) as evidenced by a linear decrease in H_2 and CO uptake from 0-1 ML Cu as well as a distinct break in the Cu and Pt AES signals at 1 ML.[172,173] STM results also show Cu growing layer-by-layer with nucleation occurring primarily at Pt step edges followed by the formation of branched Cu islands.[174] The branching was attributed to large diffusion lengths on Pt(111) terraces, but short diffusion length on Cu and Pt island edges. During the growth of the first layer, no nucleation was seen at Cu-Cu steps (steps formed due to steps edges in the Pt(111) film) indicating Cu-Pt bonds are stronger than Cu-Cu bonds.[174] LEED results show Cu growth is pseudomorphic with Pt(111) as evidenced by the appearance of no new LEED spots during the first layer of Cu growth.[172,173] After the second Cu layer, new LEED spots were observed with an ~8% smaller lattice parameter indicating Cu grew with the ideal

Cu(111) lattice spacing in the second and subsequent layers.[173] Nowicki et al.[52] found using LEED and directional elastic peak electron spectroscopy (DEPES) that Cu does not grow pseudomorphic at 330K, but forms a misfit Cu(13x13) layer on Pt(12x12) and increasing the temperature to 450 K is necessary to for pseudomorphic growth. We use the established growth models to Cu onto Pt(111) to interpret the shape of our calorimetry curve.

7.2 Results

Figure 1 shows the heat of adsorption of vapor deposited Cu onto Pt(111) as a function of Cu coverage at 300K. All heats of adsorption reported here have been corrected slightly for the hot temperature and directed nature of the Cu atomic beam, so that they correspond to Cu atoms in a Boltzmann distribution at the surface temperature, and RT has been subtracted from the measured energies, as we always do in calorimetry. This is done so that so the values on plots like Figure 1 correspond to the standard enthalpy of adsorption at the sample temperature (times -1). The heat of adsorption data in Figure 1 was divided into three distinct regions based on the growth of Cu on Pt(111) described above. In region 1 (0-1 ML), Cu adsorbs with an initial heat of adsorption of 357 kJ/mol, the heat of adsorption decreases over the first 1 ML to 339 kJ/mol. Figure 2 shows the heat of adsorption in region 1 in more detail. The decrease in heat of adsorption is well fit as a linear decrease that follows the equation $\Delta H_{ad} = (358 - 19.3\theta)$ kJ/mol where θ is the total Cu coverage in ML. In region 2 (1-3 ML), the heat of adsorption continued to decrease, but more slowly, between 1 and 2.5 ML to 333 kJ/mol. The heat then increased to the bulk heat of Cu sublimation, 337 kJ/mol,[78] by 3 ML. In region 3 (3+ ML), the heat of adsorption remained constant at the Cu heat of sublimation indicating Cu adsorbs with the same strength as it would to bulk Cu(solid).

Since the growth of Cu on Pt(111) at 330 K has been well characterized as described above, we postulate that the growth of Cu on Pt(111) at 300 K, measured calorimetrically here, also occurs layer-by-layer where the topmost Pt layer and first ML of Cu are reconstructed and form a misfit layer. From this, the adhesion energy of Cu to Pt(111) for any coverage of Cu it deposited, can be calculated using the equation from Ref.[9], which give the following energy balance:

$$n\cdot\sum_n \Delta H_{\text{adsorption}} = -n\cdot\Delta H_{\text{sublimation}} + A\cdot[(1+f)\gamma_{\text{v/m}} - E_{\text{adhesion}}],$$

where $\gamma_{\text{v/m}}$ is the surface free energy of the adsorbate, f is the surface roughness factor (for a 2D overlayer, f =1), $\sum_n \Delta H_{\text{adsorption}}$ is the integral (average) molar heat of adsorption up to the coverage of interest, n is the number of moles of the adsorbate on the surface at that coverage, A is the total area covered by the metal film, and $\Delta H_{\text{sublimation}}$ is the molar heat of sublimation of the adsorbate. Here we report the adhesion energy for four discrete Cu coverages (1, 2, 3, and 4 ML) assuming Cu forms a complete overlayer before growth in the next layer begins. The adhesion energy at 1 ML Cu is 3.86 J/m^2, it decreases to 3.84 J/m^2 by 2 ML and drops to a constant 3.78 J/m^2 for 3 and 4 ML. The decrease in adhesion energy between Cu and Pt(111) with increasing Cu coverage indicates a slight weakening of the Pt/Cu interface between 1 and 3 ML, which is consistent with the decreasing heat of adsorption up to 2.5 ML total Cu coverage. The adhesion of Cu overlayers to Pt(111) is still stronger than the adhesion of two Cu(111) planes in bulk Cu(solid) which is just two times the surface free energy (3.58 J/m^2).[9]

7.3 Discussion

In region 1, the decrease in Cu heat of adsorption with increasing Cu coverage on Pt(111) is due to the reconstructed, misfit Pt(12x12) and Cu(13x13) interface described in detail above. STM by Allison et al.[174] has shown Cu surface morphology on Pt(111) can be described by step flow growth where islands are primarily nucleated at Pt step edges and then grow outward from the step edges onto terraces in a tendril pattern. Nucleation at step sites is caused by large diffusion lengths on terraces and strong adsorption to step edges where atoms become trapped because the steps are much more energetically favorable because they from more metal-metal bonds than terraces.[175] We expect a much lower step density on our Pt(111), <5%, since they were grown and not cleaved as in Ref.[174] so it is likely some Cu islands likely nucleate on terraces in our film due to two or more Cu atoms on terraces interacting before they reach a step edge. We therefore assign the initial heat of adsorption of 357 kJ/mol to Cu adsorbing primarily at Pt step edges and a small fraction adsorbing as small islands on Pt(111) terraces. As the Cu coverage increases to 1 ML a smaller fraction of Cu bonds to Pt step edges with each subsequent pulse and a larger fraction of Cu atoms bond to Cu step edges where Pt is only below the Cu atom, forming fewer Cu-Pt bonds with each successive pulse. Based on the high initial heat of adsorption, Cu-Pt bonds are more energetically favorable that Cu-Cu bonds which is reflected by the decrease in heat of adsorption with coverage observed in region 1. It is likely all of the Pt step sites here are populated by 0.85 ML Cu coverage, STM results showed all Pt steps (which occurred in a higher density) were saturated at this coverage.[174] If only the number of Cu-Cu compared to Cu-Pt bonds formed influenced the heat of adsorption, one would expect the data in region 1 to level off after all of the Pt steps are saturated, however, there is a continuous decrease in region 1 indicating this is not the case. Therefore another mechanism is also causing the decreased heat of adsorption in region 1, which we attribute to lattice strain.

Figure 3 illustrates an idealized situation where Cu atoms in a Cu(111) island on a Pt(111) surface both have their ideal (111) lattice spacing. The central Cu atom in the island sits in its most favorable adsorption site on Pt(111), furthest down the potential well. As the island size increases the Cu atoms are further displaced out of the ideal binding site due to an 8% lattice mismatch with Pt(111) and sit higher up the potential energy curve (bottom part of Figure 3) which are energetically less favorable sites than the initial Cu atom. To overcome this energy penalty Nowicki et al.[52] showed Cu and Pt form a misfit layer where Cu has a (13x13) reconstruction and the topmost Pt layer has a (12x12) reconstruction relaxing some of the lattice strain. It is likely the misfit layer is not the most thermodynamically favorable phase because heating to 450 K causes Cu to become pseudomorphic on Pt(111), but it is kinetically limited when Cu is grown below 330 K.[52] Increasing Cu coverage in region 1 increases the fraction of the topmost Pt(111) layer that becomes strained causing the heat of adsorption of Cu do continually decrease in this region.

In region 2 the heat of adsorption of Cu continues to decrease to the Cu(bulk) heat of sublimation at 1.25 ML (337 kJ/mol). Srinivasan et al.[173] saw CO uptake up to 1.2 ML Cu indicating holes in the first Cu layer may still be present for after 1 ML. The initial decrease in this region is therefore attributed to a small fraction of Cu atoms filling in the remainder of the first Cu layer which would form more energetically favorable Cu-Pt bonds. The heat of adsorption continues to drop from 1.25 and 2.5 ML to 333 kJ/mol indicating Cu in the second layer is absorbed 1-4 kJ/mol less favorable than adsorption to Cu(bulk). The lower heat of adsorption is surprising since one would expect Pt to still interact with Cu in the second and third layers stabilizing its adsorption compared to Cu(bulk) since Cu interacts more strongly with Pt than itself. It is likely the lower than expected heat of adsorption is due to continued lattice strain in the misfit interfacial layer. The increase in heat of adsorption from 2.5-3 ML to the Cu heat of sublimation is likely due to complete relaxation of the lattice strain as the topmost Cu layers take on the ideal (111) spacing. Srinivasan et al.[173] observed new Cu (1x1) LEED spots at ~1.6 ML suggesting relaxation should occur at a much lower Cu coverage that our heats predict, but those films were grown at 450K which would kinetically favor Cu adopting a (111) spacing compared to our films grown at 300 K. In region 3, above 3 ML, the heat is constant at the Cu(bulk) heat of sublimation (337 kJ/mol). Nowicki et al.,[52] who grew their films at 330K, did not see the ideal Cu(111) spacing until 5 ML Cu so it unlikely the films are perfectly ordered here, but the lattice strain is relaxed enough to not affect the heat of adsorption.

Previous work by Bruckenstein et al.[176] and Srinivasan et al.[173] measured the difference in binding energy of the first Cu layer on polycrystalline Pt compared to all other layers using underpotential deposition. In underpotential deposition Cu is electrochemically removed from a Pt electrode, the voltage difference necessary to remove the outer Cu layers and the first Cu layer can be used to calculate the difference in binding energy of these two layers. Cu was observed to bind 39 kJ/mol more strongly to the Pt electrode than itself,[173] which would correspond to a heat of adsorption of 376 kJ/mol (heat of Cu(bulk) sublimation plus the measured electrochemical difference). This number is the average heat of adsorption of all Cu atoms in the first monolayer. To compare this value to our heat of adsorption data in figure 1, we must calculate the integral (average) heat of adsorption in region 1 which is 349 kJ/mol and is 27 kJ/mol lower than observed for electrochemical deposition. The increased heat of adsorption in underpotential deposition can be attributed to the Pt sample being polycrystalline which increases the number of favorable defect sites (steps and kinks) available compared to Pt(111) single crystals used for calorimetry. It was shown above that the defective sites are more stable adsorption sites than terraces leading to the increased heat of adsorption seen previously.[173,176] However, UPD of Cu onto Pt(111), which should have fewer defects, by Goodman et al.[177] predicted Cu bonds 83 kJ/mol more strongly in the first layer which is an average adsorption energy of 420 kJ/mol in the first Cu ML. The difference in heat of adsorption measured by UPD and SCAC is thus more likely due to solvent effects which would not be seen in the UHV calorimetry experiments here.

The measured adsorption energy here are important benchmarks to test the accuracy of theoretical calculations. To our knowledge the only DFT calculation of the adsorption energy of Cu onto Pt(111) has been done by Mentus et al.[178] using the Perdew‑Burke‑Ernzerhof (PBE) functional within the generalized gradient approximation (GGA) approximation. The adsorption energies were determined for 5 different coverages ranging from 0.25 to 1 ML and corrected here for the difference between energy and enthalpy by adding 0.8 kJ/mol (RT) to compare to our calorimetric heats of adsorption measurements in figure 1 and 2. Mentus et al.[178] determined the total heat of adsorption at 0.25 ML (single atom based on the (2x2) unit cell used in the calculations) was 338 kJ/mol and increased to 377 kJ/mol by 1 ML. Despite the overall increase in the heat of adsorption in the first monolayer, the authors predict the energy of the Cu/Pt(111) interaction decreases with increasing coverage because of a shift in the Pt d-band center to lower energy with coverage weakening the Cu-Pt bond. The increased heat of adsorption is due to the increased energy of lateral interactions in Cu islands which is calculated as a free standing layer. Results in Figures 1 and 2 suggest the heat of adsorption of Cu behaves opposite of what is predicted by DFT, and decreases with increasing Cu coverage. Since the authors correctly predict the interaction between Cu and Pt decreases with increasing coverage, differences in the heat of adsorption likely come from the Cu-Cu interaction energy being overestimated due to the Pt(111) lattice being held static during energy optimization. Nowicki et al.[52] showed the Pt(111) substrate is increasingly reconstructed as Cu coverage is increased to 1 ML which would affect the Cu-Cu interaction energy due to differences in Cu-Cu, and Cu-Pt bond lengths.

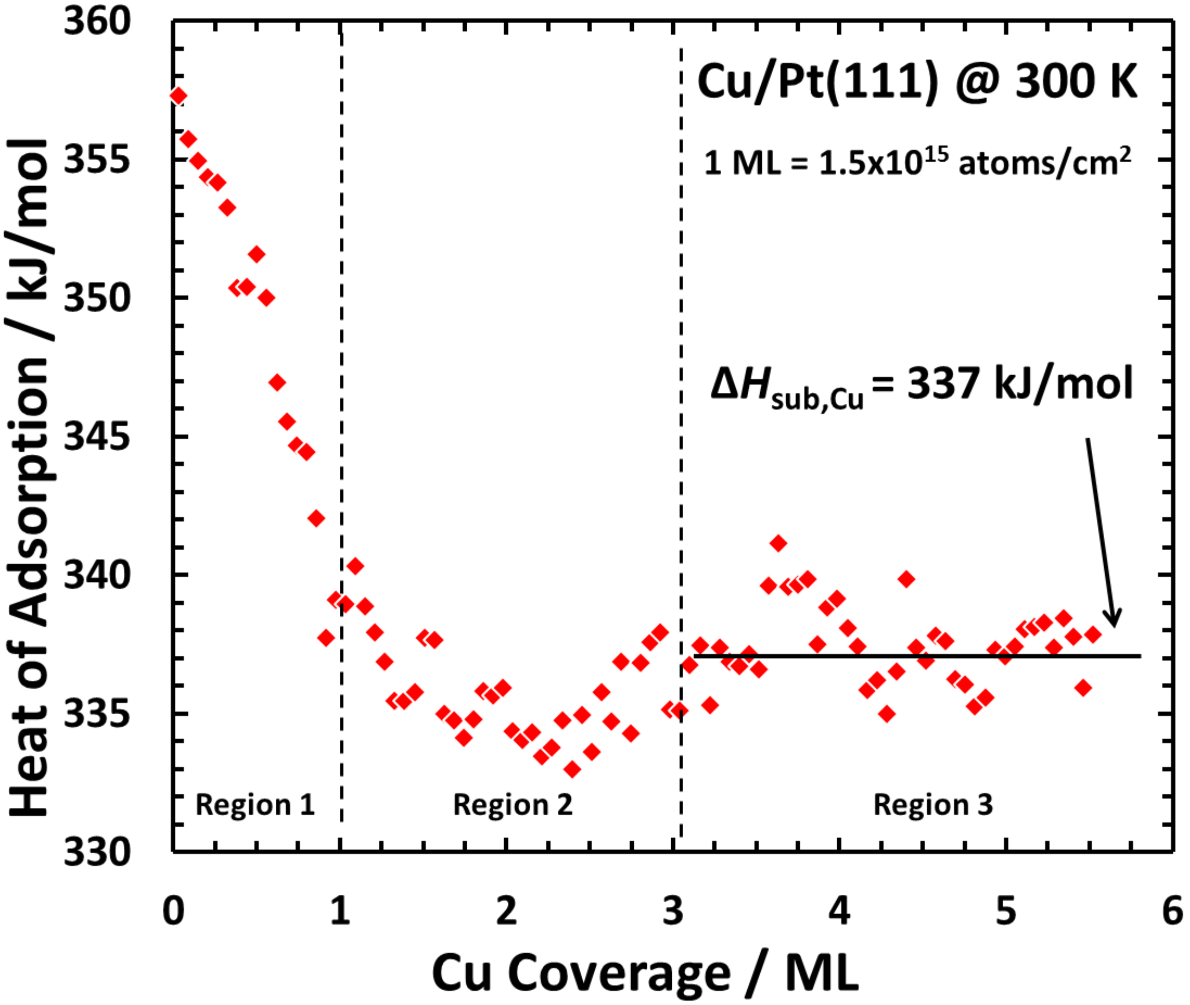

Figure 7.1: Heat of adsorption of Cu atoms onto clean Pt(111) (average of 3 experiments) at 300 K versus Cu coverage. The data will be discussed in terms of three distinct regions of coverage. Region 1 (0-1 ML) 2D Cu islands pseudomorphically on Pt(111). Region 2 (1-3 ML) where the Cu film with slightly contracted Pt(111) lattice spacing continues to grow thicker. Region 3 (>3 ML) where bulk-like Cu(111) grows in a nearly layer-by-layer mode.

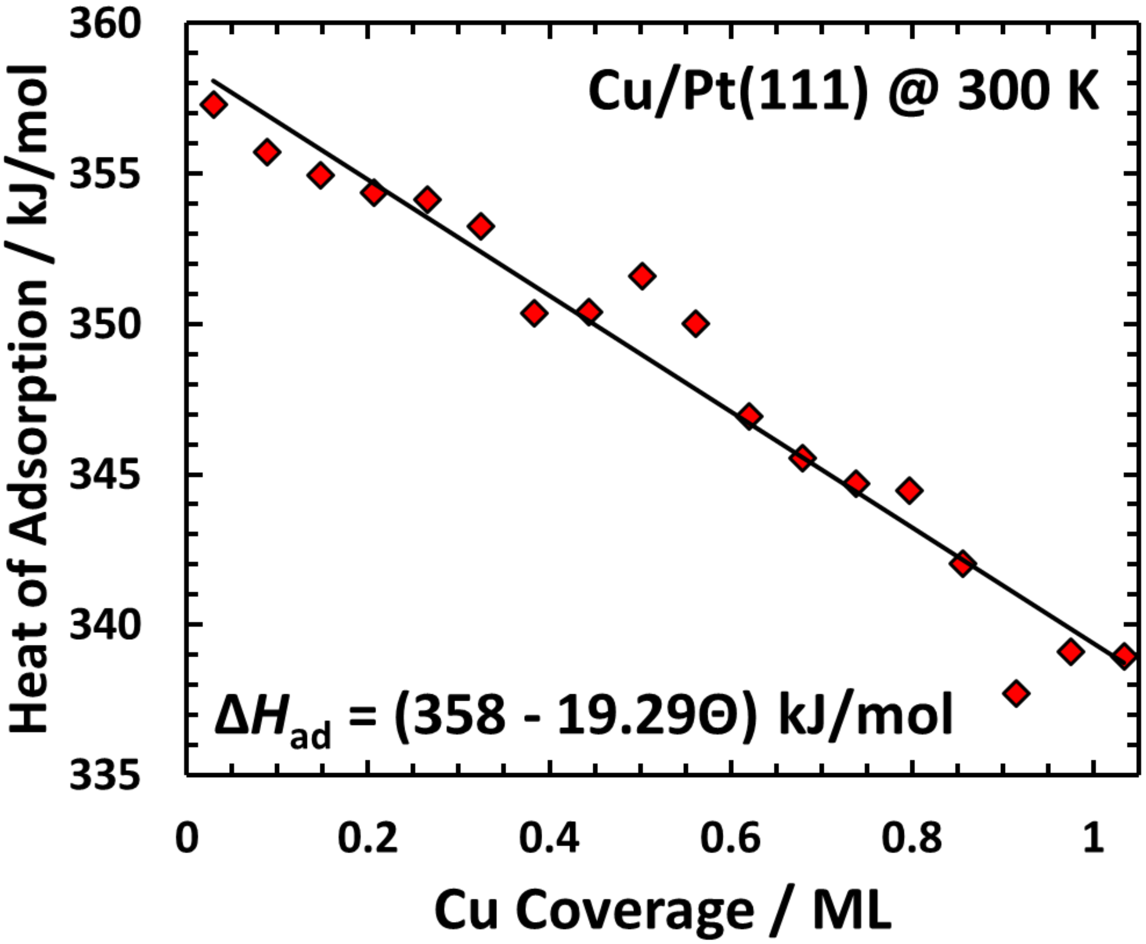

Figure 7.2: The Cu heat of adsorption in the first ML on Pt(111) from Fig. 1. Despite Cu islanding (attractive Cu-Cu interaction) a decrease in the heat of adsorption is observed due to lattice strain in the first Pt(111) layer and Cu overlayer, associated with the 8% lattice mismatch between bulk Cu(111) and Pt(111). The data from Region 1 is well fit as a linear decrease in heat of adsorption with Cu coverage as shown.

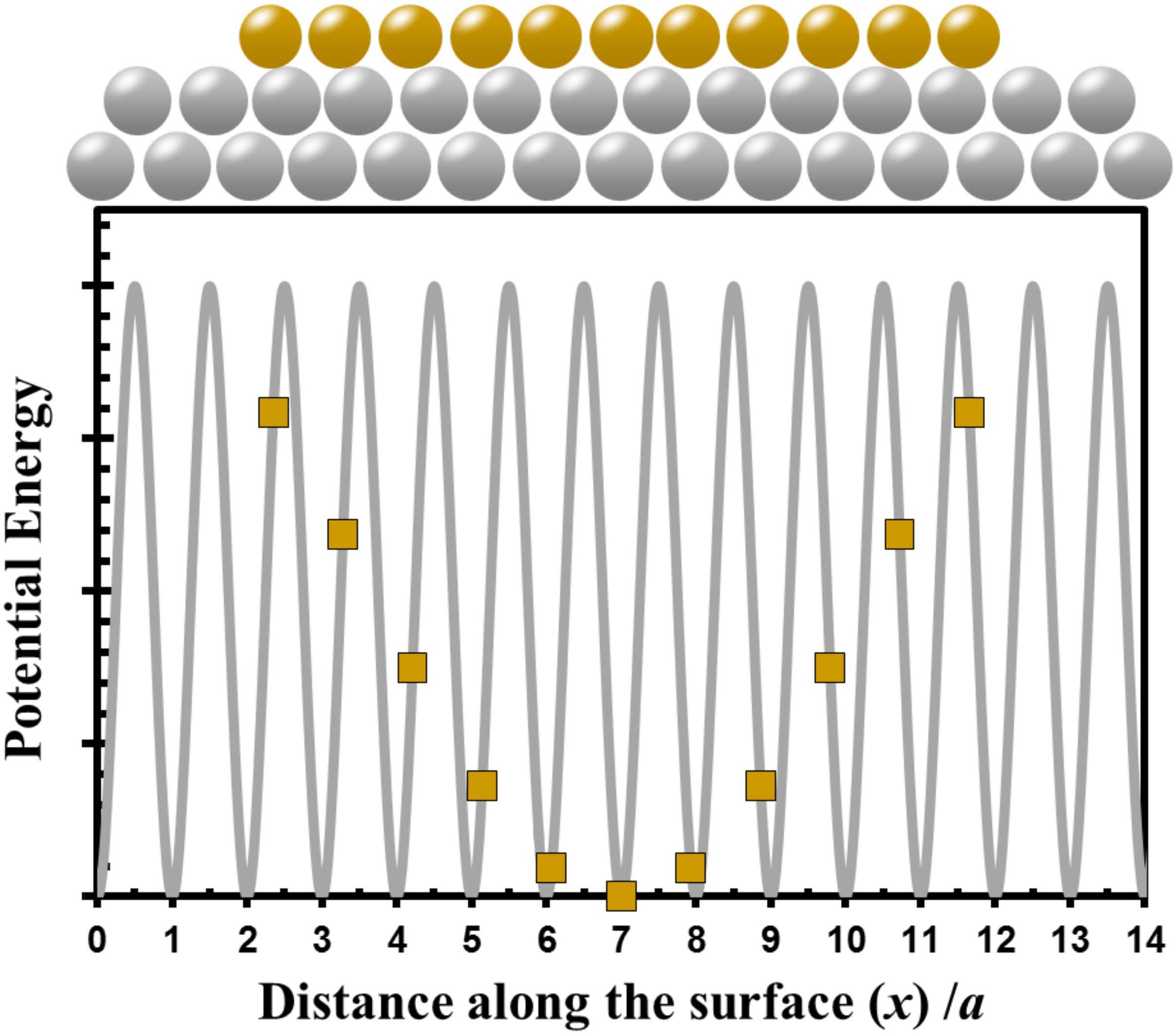

Figure 7.3: Schematic illustration of the energetics of adsorbed Cu atoms for small 2D Cu island growth on the Pt(111) surface, showing a hypothetical situation (not observed) where Cu does not adopt pseudomorphic growth but instead grows with a bulk-like Cu(111) lattice spacing. Note that this would cause Cu to sit in less and less stable adsorption sites as the Cu island size grows. Note that the energy for the Cu atoms near the edges of the island would decrease if the Pt atoms in the top layer moved slightly toward the island center and if the Cu atoms near the edges of the islands moved outward from the island center. This gives rise to forces that increase with island size (i.e., with coverage for a fixed number density of 2D islands), so the lattice stain grows with island size. The decrease in heat of adsorption with coverage in the 1st monolayer is attributed to this island-size effect.

Chapter 8

Conclusions and Future Outlook

In Chapter 2, an improved UHV single crystal adsorption calorimeter for measuring heats of adsorption of metal atoms onto single crystal surfaces is described. It utilizes an e-beam evaporator as the metal atom source. Its decreased optical radiation as compared to a Knudsen cell type evaporator allows for an 18-fold improvement in signal-to-noise ratio. Its ability to operate at higher temperatures allows for the use of metals with higher enthalpies of vaporization than that of Cu (such as Pt, Pd, Rh, Ni, and Au), for which heats of adsorption have never been determined experimentally. The calorimetric technique has also been improved by monitoring the flux of the metal atom beam in real time, which corrects for momentary instabilities in the flux of atoms reaching the surface. The system also allows for in situ relative optical reflectivity measurements on the single crystal, which improves the accuracy of the heat signal calibration and the correction for optical radiation from the hot source.

In Chapter 3, a new mathematical model for describing the growth of hemispherical cap shaped nanoparticles on a well-defined surface for non-normal incidence and detection angles in LEIS. The new model takes into account macroscopic shadowing on the integrated signal of the adsorbate and substrate which can greatly effect calculations of particle size and density of supported nanoparticles. A case study of Cu deposited onto $CeO_{1.95}(111)$ was determined to grow at a fixed particle density of $7.8x10^{12}$ particles/cm^2 showed the applicability of this model for metal/oxide systems, which is important for when microscopy images are unavailable. The results in Chapters 2 and 3 are essential for the accuracy of the results presented in this dissertation.

In Chapter 4, using ISS and XPS, Cu was found to grow as 3D particles $CeO_{2-x}(111)$ with a fixed particle density of $7.8x10^{12}$ particles/cm^2 at all extents of reduction (x = 0.05 up to 0.2). Copper atoms adsorb onto reduced $CeO_{1.95}(111)$ at 300K with an initial heat of adsorption of 300 kJ/mol. They adsorb initially more weakly to the more oxygen deficient $CeO_{1.9}(111)$ and $CeO_{1.8}(111)$ surfaces (272 and 257 kJ/mol, respectively). This is the first late transition metal studied by adsorption calorimetry on any oxide to show this stronger bonding to stoichiometric sites compared to sites with oxygen vacancies. The heat of adsorption on $CeO_{1.95}(111)$ then decreases with coverage up to 0.1 ML, due to the Cu particles spreading from stoichiometric step edges to step sites with vacancies and terrace sites as their size grows up to 0.8 diameter. Above a total Cu coverage of ~0.1 ML (>0.8 nm diameter), incoming Cu atoms adsorb with the same average heat of adsorption on all three ceria oxidation states, increasing with coverage (particle size) to the bulk Cu(solid) heat of sublimation by 3.5 ML (2.2 nm diameter). Cu adsorption causes a faster decrease in the Ce^{4+} XPS signal compared to Ce^{3+} in the Ce 3d XPS region, due to its selective binding at stoichiometric sites and the transfer of a small amount of electron density from Cu to ceria (<0.17 electrons per Cu atom). The adhesion energy of 2.2 nm Cu nanoparticles onto $CeO_{1.95}(111)$ at 300 K was determined to be 3.52 J/m^2 and decreased to 3.45 and 3.43 J/m^2 for $CeO_{1.9}(111)$ and $CeO_{1.8}(111)$, respectively.

As shown in Chapter 5, copper atoms adsorb onto $CeO_{1.95}(111)$ at 100 K with a nearly constant heat of adsorption of 224 kJ/mol at very low coverage, associated with Cu adatoms on stoichiometric terrace sites. Above 0.05 ML, Cu grows as 3D Cu nanoparticles on $CeO_{1.95}(111)$ at 100 K, with a fixed particle density of $5.3x10^{13}$ particles/cm^2, 7-fold larger than at 300 K The heat of adsorption increases slowly with coverage (and particle size) to eventually reach the heat of sublimation of bulk Cu(solid). The heat of Cu adsorption when making Cu nanoparticles with an average diameter of 0.45 to 0.8 nm is lower at 100 K than at 300K by ~50 to 30 kJ/mol on the same $CeO_{1.95}(111)$ surface, attributed to cluster nucleation on terrace sites at 100K but instead on the more stable step edge sites at 300K. Figure 4 summarizes the measured chemical potential of Cu atoms versus Cu nanoparticle size at both stoichiometric $CeO_2(111)$ terraces and step edges with ~50% oxygen vacancies. Since Cu is much less stable near oxygen vacancies on this surface[3], it will avoid bonding near oxygen vacancies upon adsorption. Thus, the results for the smallest Cu clusters in Figure 1 are not strongly influenced by the ~2.5% oxygen vacancies present on this CeO_2 surface. We therefore consider the monomer and dimer energies in Figure 4 to be representative of stoichiometric $CeO_2(111)$. Comparison to DFT+U calculations shows that calculated monomer adsorption energies differ from this experiment by -44 to +69 kJ/mol.

In Chapter 6, LEIS showed Au to grow as 3D particles on slightly reduced $CeO_2(111)$ at 300 and 100 K. The Au particle density increased with the degree of ceria reduction for both temperatures studied here. The particle density also increased for all oxidation states at 100 K, compared to 300 K, due to higher diffusion barriers for Au particles. During growth of Au nanoparticles on $CeO_{1.8}(111)$ at 300 K, the incoming Au atoms land mainly in Au-free $CeO_2(111)$ regions, but diffuse to existing Au particles and apparently prefer to move up on top of existing particles. They thus grow significantly thicker than hemispherical caps beyond a certain particle diameter, which was not observed under any other condition. Au atoms adsorb 37 kJ/mol more strongly to the more oxygen-deficient $CeO_{1.8}(111)$ than $CeO_{1.95}(111)$, similar to what was observed for Ag adsorption to the same surface. The heat of adsorption on all surfaces slowly increases to the heat of Au sublimation by 2 ML. The adhesion energy of 3.6 nm Au particles on $CeO_{1.95}(111)$ was found to be 2.53 J/m^2 and increased to 2.98 J/m^2 on $CeO_{1.8}(111)$ for smaller, 2.6 nm particles. The adhesion energy of metals onto $CeO_2(111)$ are well correlated by the difference between their heat of sublimation and heat of formation of their most stable oxide, consistent with previously observed trends of metals on MgO(100).

In Chapter 7, using single crystal adsorption calorimetry, Cu was found to adsorb onto Pt(111) with an initial heat of adsorption of 358 kJ/mol and decrease linearly with coverage in the first monolayer, which was well fit by the equation, $\Delta H_{\mathrm{ad}} = (358 - 19.3\theta)$ kJ/mol. Cu grows layer-by-layer on Pt(111), forming misfit layers at room temperature therefore the observed decrease was explained by fewer Pt-Cu bonds being formed as total Cu coverage increased which are stronger than Cu-Cu bonds, and lattice strain in the topmost Pt and Cu layers due to lattice mismatch between the (111) crystal faces of these two metals. The lattice strain caused the Cu heat of adsorption between 1 and 3 ML to be lower than the heat of sublimation of bulk Cu(metal). After 3 ML the Cu heat of adsorption reached the heat of sublimation of bulk Cu(metal). The adhesion energy of the first ML of Cu to Pt(111) at 300K was determined to be 3.84 J/m^2 and decreased to 3.76 J/m^2 by 4 ML. These results are an important benchmark for testing the energy accuracy of quantum mechanical calculations of metal/metal bonding such as in density functional theory.

While this work is not a complete picture for interfacial energetics, the studies greatly improve our understanding of the adsorption and adhesion of metals to oxide and single crystal metal surfaces which is important for the development of more efficient catalysts. The results here can be extended to a wide variety of advanced technologies such as chemical sensors, electrocatalysts, photocatalysts, and fuel cells. We have recently finished experiments measuring interfacial energies of Au/MgO(100) and Au/Pt(111), which are important catalytic model systems. The goal is to continue studying metal adsorption energetics to reduced CeO_2(111), MgO(100), and Fe_3O_4(111) and extend studies to new substrates such at TiO_2(110) to gain a better understanding how the support affects bonding. Studying the adsorption energy of platinum to oxide surfaces is also very important. Platinum nanoparticles supported on oxides are highly active catalysts for a wide variety of reactions, including some of the most economically-impactful of all catalytic reactions. Understanding the strength of Pt/oxide bonds could provide valuable insight into its unique catalytic activity. More studies of this nature should also help serve as benchmarks to improve the absolute energy accuracy of theoretical calculation using DFT which provide a high throughput method for studying metal/oxide interactions.

References

(1) *CRC Handbook of Chemistry and Physics (Internet Version)*: 93rd ed.; Haynes, W. M., Ed.; CRC Press / Taylor and Francis: Boca Raton, FL, 2012.

(2) Szabova, L.; Skala, T.; Matolinova, I.; Fabris, S.; Camellone, M. F.; Matolin, V. Copper-ceria interaction: A combined photoemission and DFT study. *Applied Surface Science* **2013**, *267*, 12-16.

(3) James, T. E.; Hemmingson, S. L.; Ito, T.; Campbell, C. T. Energetics of Cu Adsorption and Adhesion onto Reduced CeO2(111) Surfaces by Calorimetry. *Journal of Physical Chemistry C* **2015**, *119*, 17209-17217.

(4) Hagen, J.: *Industrial Catalysis: A Practical Approach*; Wiley: New York, 2005.

(5) *Annual Energy Outlook 2015,* U.S. Energy Information Administration.

(6) Goodman, D. W. Model studies in catalysis using surface science probes. *Chemical Reviews* **1995**, *95*, 523-536.

(7) Baumer, M.; Freund, H. J. Metal deposits on well-ordered oxide films. *Progress in Surface Science* **1999**, *61*, 127-198.

(8) Somorjai, G. A.; Park, J. Y. The impact of surface science on the commercialization of chemical processes. *Catalysis Letters* **2007**, *115*, 87-98.

(9) Campbell, C. T. Ultrathin metal films and particles on oxide surfaces: Structural, electronic and chemisorptive properties. *Surface Science Reports* **1997**, *27*, 1-111.

(10) Farmer, J. A.; Campbell, C. T. Ceria Maintains Smaller Metal Catalyst Particles by Strong Metal-Support Bonding. *Science* **2010**, *329*, 933-936.

(11) Campbell, C. T.; Sellers, J. R. V. Anchored metal nanoparticles: Effects of support and size on their energy, sintering resistance, and reactivity. *Faraday Discussions* **2013**, *162*, 9-30.

(12) Campbell, C. T.; Starr, D. E. Metal adsorption and adhesion energies on MgO(100). *Journal of the American Chemical Society* **2002**, *124*, 9212-9218.

(13) Sharp, J. C.; Yao, Y. X.; Campbell, C. T. Silver Nanoparticles on Fe_3O_4(111): Energetics by Ag Adsorption Calorimetry and Structure by Surface Spectroscopies. *Journal of Physical Chemistry C* **2013**, *117*, 24932-24936.

(14) Farmer, J. A.; Baricuatro, J. H.; Campbell, C. T. Ag Adsorption on Reduced CeO_2(111) Thin Films. *Journal of Physical Chemistry C* **2010**, *114*, 17166-17172.

(15) He, J. W.; Shea, W. L.; Jiang, X.; Goodman, D. W. Surface Chemistry of Monolayer Metallic Films on Re(0001) and Mo(110). *Journal of Vacuum Science & Technology a-Vacuum Surfaces and Films* **1990**, *8*, 2435-2444.

(16) Borroni-Bird, C. E.; King, D. A. An Ultrahigh-Vacuum Single-Crystal Adsorption Microcalorimeter. *Review of Scientific Instruments* **1991**, *62*, 2177-2185.

(17) Stuckless, J. T.; Frei, N. A.; Campbell, C. T. A novel single-crystal adsorption calorimeter and additions for determining metal adsorption and adhesion energies. *Review of Scientific Instruments* **1998**, *69*, 2427-2438.

(18) Stuckless, J. T.; Frei, N. A.; Campbell, C. T. Pyroelectric detector for single-crystal adsorption microcalorimetry: analysis of pulse shape and intensity. *Sensors and Actuators B-Chemical* **2000**, *62*, 13-22.

(19) Venables, J. A. Atomic Processes in Crystal Growth. *Surface Science* **1994**, *299*, 798-817.

(20) Fu, Q.; Wagner, T. Interaction of nanostructured metal overlayers with oxide surfaces. *Surface Science Reports* **2007**, *62*, 431-498.

(21) Diebold, U.; Pan, J. M.; Madey, T. E. Growth Mode of Ultrathin Copper Overlayers on TiO_2(110). *Physical Review B* **1993**, *47*, 3868-3876.

(22) Mullins, D. R. The surface chemistry of cerium oxide. *Surface Science Reports* **2015**, *70*, 42-85.

(23) Trovarelli, A.; de Leitenburg, C.; Boaro, M.; Dolcetti, G. The utilization of ceria in industrial catalysis. *Catalysis Today* **1999**, *50*, 353-367.

(24) Trovarelli, A.: *Catalysis by Ceria and Related Materials*; Imperial College Press: London, 2002.

(25) Kaspar, J.; Fornasiero, P.; Graziani, M. Use of CeO2-based oxides in the three-way catalysis. *Catalysis Today* **1999**, *50*, 285-298.

(26) Bunluesin, T.; Gorte, R. J.; Graham, G. W. Studies of the water-gas-shift reaction on ceria-supported Pt, Pd, and Rh: implications for oxygen-storage properties. *Applied Catalysis B-Environmental* **1998**, *15*, 107-114.

(27) Liu, W.; Flytzani-Stephanopoulos, M. Total Oxidation of Carbon Monoxide and Methane over Transition Metal-Fluorite Oxide Composite Catalysts 1. Catalyst Composition and Activity. *Journal of Catalysis* **1995**, *153*, 304-316.

(28) Liu, W.; Flytzani-Stephanopoulos, M. Transition metal-promoted oxidation catalysis by fluorite oxides: A study of CO oxidation over Cu-CeO_2. *Chemical Engineering Journal* **1996**, *64*, 283-294.

(29) Wang, X. Q.; Rodriguez, J. A.; Hanson, J. C.; Gamarra, D.; Martinez-Arias, A.; Fernandez-Garcia, M. In situ studies of the active sites for the water gas shift reaction over Cu-CeO_2 catalysts: Complex interaction between metallic copper and oxygen vacancies of ceria. *Journal of Physical Chemistry B* **2006**, *110*, 428-434.

(30) Rodriguez, J. A.; Liu, P.; Hrbek, J.; Evans, J.; Perez, M. Water gas shift reaction on Cu and Au nanoparticles supported on CeO_2(111) and ZnO(000(1)): Intrinsic activity and importance of support interactions. *Angewandte Chemie-International Edition* **2007**, *46*, 1329-1332.

(31) Graciani, J.; Mudiyanselage, K.; Xu, F.; Baber, A. E.; Evans, J.; Senanayake, S. D.; Stacchiola, D. J.; Liu, P.; Hrbek, J.; Fernandez Sanz, J.; Rodriguez, J. A. Highly active copper-ceria and copper-ceria-titania catalysts for methanol synthesis from CO_2. *Science* **2014**, *345*, 546-550.

(32) Graciani, J.; Vidal, A. B.; Rodriguez, J. A.; Fdez. Sanz, J. Unraveling the Nature of the Oxide-Metal Interaction in Ceria-Based Noble Metal Inverse Catalysts. *Journal of Physical Chemistry C* **2014**, *118*, 26931-26938.

(33) Hafner, J. Ab-initio simulations of materials using VASP: Density-functional theory and beyond. *Journal of Computational Chemistry* **2008**, *29*, 2044-2078.

(34) Szabova, L.; Camellone, M. F.; Huang, M.; Matolin, V.; Fabris, S. Thermodynamic, electronic and structural properties of Cu/CeO_2 surfaces and interfaces from first-principles DFT plus U calculations. *Journal of Chemical Physics* **2010**, *133*, 234705.

(35) Yang, Z. X.; He, B. L.; Lu, Z. S.; Hermansson, K. Physisorbed, Chemisorbed, and Oxidized CO on Highly Active Cu-CeO_2(111). *Journal of Physical Chemistry C* **2010**, *114*, 4486-4494.

(36) Tang, Y. H.; Zhang, H.; Cui, L. X.; Ouyang, C. Y.; Shi, S. Q.; Tang, W. H.; Li, H.; Chen, L. Q. Electronic states of metal (Cu, Ag, Au) atom on CeO_2(111) surface: The role of local structural distortion. *Journal of Power Sources* **2012**, *197*, 28-37.

(37) Yang, Z.; Xie, L.; Ma, D.; Wang, G. Origin of the High Activity of the Ceria-Supported Copper Catalyst for H_2O Dissociation. *Journal of Physical Chemistry C* **2011**, *115*, 6730-6740.

(38) Marta Branda, M.; Hernandez, N. C.; Fdez Sanz, J.; Illas, F. Density Functional Theory Study of the Interaction of Cu, Ag, and Au Atoms with the Regular CeO_2 (111) Surface. *Journal of Physical Chemistry C* **2010**, *114*, 1934-1941.

(39) Huang, M.; Fabris, S. CO adsorption and oxidation on ceria surfaces from DFT+U calculations. *Journal of Physical Chemistry C* **2008**, *112*, 8643-8648.

(40) Haruta, M.; Date, M. Advances in the catalysis of Au nanoparticles. *Applied Catalysis a-General* **2001**, *222*, 427-437.

(41) Haruta, M. Catalysis of gold nanoparticles deposited on metal oxides. *Cattech* **2002**, *6*, 102-115.

(42) Hashmi, A. S. K.; Hutchings, G. J. Gold catalysis. *Angewandte Chemie-International Edition* **2006**, *45*, 7896-7936.

(43) Fu, Q.; Weber, A.; Flytzani-Stephanopoulos, M. Nanostructured Au-CeO_2 catalysts for low-temperature water-gas shift. *Catalysis Letters* **2001**, *77*, 87-95.

(44) Schubert, M. M.; Plzak, V.; Garche, J.; Behm, R. J. Activity, selectivity, and long-term stability of different metal oxide supported gold catalysts for the preferential CO oxidation in H_2-rich gas. *Catalysis Letters* **2001**, *76*, 143-150.

(45) Campbell, C. T. Bimetallic Surface Chemistry. *Annual Review of Physical Chemistry* **1990**, *41*, 775-837.

(46) Rodriguez, J. A.; Goodman, D. W. The Nature of the Metal-Metal Bond in Bimetallic Surfaces. *Science* **1992**, *257*, 897-903.

(47) Rodriguez, J. A. Physical and chemical properties of bimetallic surfaces. *Surface Science Reports* **1996**, *24*, 225-287.

(48) Rodriguez, J. A.; Truong, C. M.; Goodman, D. W. Infrared Vibrational Studies of CO Adsorption on Cu/Pt(111) and CuPt(111) Surfaces. *Journal of Chemical Physics* **1992**, *96*, 7814-7825.

(49) Schumacher, N.; Andersson, K.; Grabow, L. C.; Mavrikakis, M.; Nerlov, J.; Chorkendorff, I. Interaction of carbon dioxide with Cu overlayers on Pt(111). *Surface Science* **2008**, *602*, 702-711.

(50) Schumacher, N.; Andersson, K. J.; Nerlov, J.; Chorkendorff, I. Formate stability and carbonate hydrogenation on strained Cu overlayers on Pt(111). *Surface Science* **2008**, *602*, 2783-2788.

(51) Tsay, J. S.; Mangen, T.; Linden, R. J.; Wandelt, K. Adsorption of oxygen on ultrathin Cu/Pt(111) films. *Journal of Vacuum Science & Technology a-Vacuum Surfaces and Films* **2001**, *19*, 2217-2221.

(52) Miszczuk, A.; Morawski, I.; Nowicki, M. Properties of Cu films on Pt(111) revealed by AES, LEED, and DEPES. *Applied Surface Science* **2013**, *284*, 386-391.

(53) Stuckless, J. T.; Starr, D. E.; Bald, D. J.; Campbell, C. T. Metal adsorption calorimetry and adhesion energies on clean single-crystal surfaces. *Journal of Chemical Physics* **1997**, *107*, 5547-5553.

(54) Campbell, C. T.; Parker, S. C.; Starr, D. E. The effect of size-dependent nanoparticle energetics on catalyst sintering. *Science* **2002**, *298*, 811-814.

(55) Starr, D. E.; Ranney, J. T.; Larsen, J. H.; Musgrove, J. E.; Campbell, C. T. Measurement of the energetics of metal film growth on a semiconductor: Ag/Si(100)-(2 x 1). *Physical Review Letters* **2001**, *87*, 106102.

(56) Howe, J. M. Bonding, Structure and Properties of Metal-Ceramic Interfaces. 1. Chemical Bonding, Chemical Reaction and Interfacial Structure. *International Materials Reviews* **1993**, *38*, 233-256.

(57) Larsen, J. H.; Ranney, J. T.; Starr, D. E.; Musgrove, J. E.; Campbell, C. T. Adsorption energetics of Ag on MgO(100). *Physical Review B* **2001**, *63*, 195410.

(58) Campbell, C. T.; Lytken, O. Experimental measurements of the energetics of surface reactions. *Surface Science* **2009**, *603*, 1365-1372.

(59) Somorjai, G. A.; Park, J. Y. Concepts, instruments, and model systems that enabled the rapid evolution of surface science. *Surface Science* **2009**, *603*, 1293-1300.

(60) Wanke, S. E.; Flynn, P. C. Sintering of supported metal catalysts. *Catalysis Reviews: Science and Engineering* **1975**, *12*, 93-135.

(61) Stuckless, J. T.; Starr, D. E.; Bald, D. J.; Campbell, C. T. Calorimetric measurements of the energetics of Pb adsorption and adhesion to Mo(100). *Physical Review B* **1997**, *56*, 13496-13502.

(62) Ranney, J. T.; Starr, D. E.; Musgrove, J. E.; Bald, D. J.; Campbell, C. T. A microcalorimetric study of the heat of adsorption of copper on well-defined oxide thin film surfaces: MgO(100), p(2 x 1) oxide on Mo(100) and disordered W oxide. *Faraday Discussions* **1999**, *114*, 195-208.

(63) Larsen, J. H.; Starr, D. E.; Campbell, C. T. Enthalpies of adsorption of metal atoms on single-crystalline surfaces by microcalorimetry. *Journal of Chemical Thermodynamics* **2001**, *33*, 333-345.

(64) Starr, D. E.; Campbell, C. T. Low-temperature adsorption microcalorimetry: Pb on MgO(100). *Journal of Physical Chemistry B* **2001**, *105*, 3776-3782.

(65) Starr, D. E.; Bald, D. J.; Musgrove, J. E.; Ranney, J. T.; Campbell, C. T. Microcalorimetric measurements of the heat of absorption of Pb on well-defined oxides: MgO(100) and p(2x1)-oxide on Mo(100). *Journal of Chemical Physics* **2001**, *114*, 3752-3764.

(66) Starr, D. E.; Diaz, S. F.; Musgrove, J. E.; Ranney, J. T.; Bald, D. J.; Nelen, L.; Ihm, H.; Campbell, C. T. Heat of absorption of Cu and Pb on hydroxyl-covered MgO(100). *Surface Science* **2002**, *515*, 13-20.

(67) Zhu, J.; Farmer, J. A.; Ruzycki, N.; Xu, L.; Campbell, C. T.; Henkelman, G. Calcium adsorption on MgO(100): Energetics, structure, and role of defects. *Journal of the American Chemical Society* **2008**, *130*, 2314-2322.

(68) Farmer, J. A.; Ruzycki, N.; Zhu, J. F.; Campbell, C. T. Lithium adsorption on MgO(100) and its defects: Charge transfer, structure, and energetics. *Physical Review B* **2009**, *80*, 035418.

(69) Farmer, J. A.; Campbell, C. T.; Xu, L.; Henkelman, G. Defect Sites and Their Distributions on MgO(100) by Li and Ca Adsorption Calorimetry. *Journal of the American Chemical Society* **2009**, *131*, 3098-3103.

(70) Borroni-Bird, C. E.; Al-Sarraf, N.; Andersson, S.; King, D. A. Single-Crystal Adsorption Microcalorimetry. *Chemical Physics Letters* **1991**, *183*, 516-520.

(71) Al-Sarraf, N.; Stuckless, J. T.; Wartnaby, C. E.; King, D. A. Adsorption microcalorimetry and sticking probabilities on metal single crystal surfaces. *Surface Science* **1993**, *283*, 427-437.

(72) Dixon-Warren, S. J.; Kovar, M.; Wartnaby, C. E.; King, D. A. Pyroelectric single crystal adsorption microcalorimetry at low temperatures: oxygen on Ni{100}. *Surface Science* **1994**, *307-309*, 16-22.

(73) Ajo, H. M.; Ihm, H.; Moilanen, D. E.; Campbell, C. T. Calorimeter for adsorption energies of larger molecules on single crystal surfaces. *Review of Scientific Instruments* **2004**, *75*, 4471-4480.

(74) Lew, W.; Lytken, O.; Farmer, J. A.; Crowe, M. C.; Campbell, C. T. Improved pyroelectric detectors for single crystal adsorption calorimetry from 100 to 350 K. *Review of Scientific Instruments* **2010**, *81*, 024102.

(75) Crowe, M. C.; Campbell, C. T. Adsorption Microcalorimetry: Recent Advances in Instrumentation and Application. *Annual Review of Analytical Chemistry* **2011**, *4*, 41-58.

(76) Silbaugh, T. L.; Karp, E. M.; Campbell, C. T. Surface kinetics and energetics from single crystal adsorption calorimetry lineshape analysis: Methyl from methyl iodide on Pt(111). *Journal of Catalysis* **2013**, 308, 114-121.

(77) King, D. A.; Wells, M. G. Reaction mechanism in chemisorption kinetics: nitrogen on the {100} plane of tungsten. *Proceedings of the Royal Society of London Series A: Mathematical and Physical Sciences* **1974**, *339*, 245-269.

(78) *CRC Handbook of Chemistry and Physics*; 95 ed.; CRC Press: Boston, 2014.

(79) Barium Fluoride (BaF2) Specifications. In *Barium Fluoride (BaF2) Specifications*; ISP Optics: http://store.ispoptics.com/pdfs/pdfCatalog/page08.pdf, accessed June 25, 2013.

(80) Jones, T.; Sawler, J.; Venus, D. Simple, Calibrated Deposition Monitor Incorporated into an Electron Beam Evaporator. *Review of Scientific Instruments* **1993**, *64*, 2008-2012.

(81) Band, A.; Stroscio, J. A. A closed loop controller for electron-beam evaporators. *Review of Scientific Instruments* **1996**, *67*, 2366-2369.

(82) Lu, C.; Guan, Y. Improved method of nonintrusive deposition rate monitoring by atomic absorption spectroscopy for physical vapor deposition processes. *Journal of Vacuum Science & Technology A* **1995**, *13*, 1797-1801.

(83) Behrndt, K. H.; Love, R. W. Automatic control of film-deposition rate with the crystal oscillator for preparation of alloy films. *Vacuum* **1962**, *12*, 1-9.

(84) Schiller, S.; Jaesch, G.; Neumann, M. High Rate Electron Beam Evaporation. *Thin Solid Films* **1983**, *110*, 149-164.

(85) Weaver, J. H.; Lynch, D. W.; Olson, C. G. Optical properties of V, Ta, and Mo from 0.1 to 35 eV. *Physical Review B* **1974**, *10*, 501-516.

(86) Karp, E. M.; Campbell, C. T.; Studt, F.; Abild-Pedersen, F.; Norskov, J. K. Energetics of Oxygen Adatoms, Hydroxyl Species and Water Dissociation on Pt(111). *Journal of Physical Chemistry C* **2012**, *116*, 25772-25776.

(87) McIntyre, J. D.; Aspnes, D. E. Differential Reflection Spectroscopy of Very Thin Surface Films. *Surface Science* **1971**, *24*, 417-434.

(88) Lin, K. C.; Tobin, R. G.; Dumas, P. Adsorbate Induced Changes in the Broad-Band Infrared Reflectance of a Metal - Oxygen on Cu(100). *Physical Review B* **1994**, *49*, 17273-17278.

(89) Dvorak, J.; Dai, H. L. Optical reflectivity changes induced by adsorption on metal surfaces: The origin and applications to monitoring adsorption kinetics. *Journal of Chemical Physics* **2000**, *112*, 923-934.

(90) Bennett, H. E. Specular Reflectance of Aluminized Ground Glass and Height Distribution of Surface Irregularities. *Journal of the Optical Society of America* **1963**, *53*, 1389-1393.

(91) Fischer-Wolfarth, J.-H.; Hartmann, J.; Farmer, J. A.; Flores-Camacho, J. M.; Campbell, C. T.; Schauermann, S.; Freund, H.-J. An improved single crystal adsorption calorimeter for determining gas adsorption and reaction energies on complex model catalysts. *Review of Scientific Instruments* **2011**, *82*, 024102.

(92) Mandelis, A.; Zver, M. M. Theory of Photopyroelectric Spectroscopy of Solids. *Journal of Applied Physics* **1985**, *57*, 4421-4430.

(93) Batt, R. J.; Calcutt, D. M.; Hackett, J. M. The determination of Reflectivity of a Metal Film at Submillimeter Wavelengths Using and Electrical Substituation Technique and a Dedicated Mircoprocessor System. *Journal of Physics-Condensed Matter* **1989**, *1*, SB249-SB250.

(94) Paffett, M. T.; Campbell, C. T.; Taylor, T. N.; Srinivasan, S. Cu Adsorption on Pt(111) and its Effects on Chemisorption - A Comparistion with Electrochemistry. *Surface Science* **1985**, *154*, 284-302.

(95) Shek, M. L.; Stefan, P. M.; Lindau, I.; Spicer, W. E. Photoemmission study of the Adsorption of Cu on Pt(111). *Physical Review B* **1983**, *27*, 7277-7287.

(96) Yeates, R. C.; Somorjai, G. A. The Growth and Alloy Formation of Copper on the Platinum(111) and Stepped(553) Crystal Surfaces - Characterization by LEED, AES, and CO Thermal Desporption. *Surface Science* **1983**, *134*, 729-744.

(97) Leung, L.-W. H.; Gregg, T. W.; Goodman, D. W. Electrochemical and Ultrahigh Vacuum Characterization of Ultrathin Cu Films on Pt(111). *Langmuir* **1991**, *7*, 3205-3210.

(98) Karp, E. M.; Silbaugh, T. L.; Crowe, M. C.; Campbell, C. T. Energetics of Adsorbed Methanol and Methoxy on Pt(111) by Microcalorimetry. *Journal of the American Chemical Society* **2012**, *134*, 20388-20395.

(99) Argile, C.; Rhead, G. E. Adsorbed Layer and Thin-Film Growth Modes Monitored by Auger-Electron Spectroscopy. *Surface Science Reports* **1989**, *10*, 277-356.

(100) Tong, W. M.; Williams, R. S. Kinetics of surface growth - phenomenology, scaling, and mechanisms of smoothening and roughening. *Annual Review of Physical Chemistry* **1994**, *45*, 401-438.

(101) Brongersma, H. H.; Draxler, M.; de Ridder, M.; Bauer, P. Surface composition analysis by low-energy ion scattering. *Surface Science Reports* **2007**, *62*, 63-109.

(102) Sharp, J. C.; Campbell, C. T. Quantitative modeling of electron spectroscopy intensities for supported nanoparticles: The hemispherical cap model for non-normal detection. *Surface Science* **2015**, *632*, L5-L8.

(103) Gunter, P. L. J.; Niemantsverdriet, J. W.; Ribeiro, F. H.; Somorjai, G. A. Surface science approach to modeling supported catalysts. *Catalysis Reviews-Science and Engineering* **1997**, *39*, 77-168.

(104) Campbell, C. T. The Energetics of Supported Metal Nanoparticles: Relationships to Sintering Rates and Catalytic Activity. *Accounts of Chemical Research* **2013**, *46*, 1712-1719.

(105) Campbell, C. T.; Sellers, J. R. V. Anchored metal nanoparticles: Effects of support and size on their energy, sintering resistance and reactivity. *Faraday Discussions* **2013**, *162*, 9-30.

(106) Romeo, M.; Bak, K.; Elfallah, J.; Lenormand, F.; Hilaire, L. XPS Study of the Reduction of Cerium Dioxide. *Surface and Interface Analysis* **1993**, *20*, 508-512.

(107) Luches, P.; Pagliuca, F.; Valeri, S. Structural and morphological modifications of thermally reduced cerium oxide ultrathin epitaxial films on Pt(111). *Physical Chemistry Chemical Physics* **2014**, *16*, 18848-18857.

(108) Campbell, C. T.; James, T. E. Ion Scattering Spectroscopy Intensities for Supported Nanoparticles: The Hemispherical Cap Model. *Surface Science* **2015**, *641*, 166-169.

(109) Tanuma, S.; Powell, C. J.; Penn, D. R. Calculations of electron inelastic mean free paths for 31 materials. *Surface and Interface Analysis* **1988**, *11*, 577-589.

(110) Briggs, D.; Seah, M. P.: *Practical Surface Analysis*; 2nd ed.; Wiley: New York, 1990; Vol. 2.

(111) Wu, Y. T.; Garfunkel, E.; Madey, T. E. Initial stages of Cu growth on ordered Al_2O_3 ultrathin films. *Journal of Vacuum Science & Technology a-Vacuum Surfaces and Films* **1996**, *14*, 1662-1667.

(112) Chen, D. A.; Bartelt, M. C.; Hwang, R. Q.; McCarty, K. F. Self-limiting growth of copper islands on TiO_2(110)-(1 x 1). *Surface Science* **2000**, *450*, 78-97.

(113) Worren, T.; Hansen, K. H.; Laegsgaard, E.; Besenbacher, F.; Stensgaard, I. Copper clusters on Al_2O_3/NiAl(110) studied with STM. *Surface Science* **2001**, *477*, 8-16.

(114) Hu, S.; Wang, Y.; Wang, W.; Han, Y.; Fan, Q.; Feng, X.; Xu, Q.; Zhu, J. Ag Nanoparticles on Reducible CeO_2(111) Thin Films: Effect of Thickness and Stoichiometry of Ceria. *Journal of Physical Chemistry C* **2015**, *119*, 3579-3588.

(115) Lu, J. L.; Gao, H. J.; Shaikhutdinov, S.; Freund, H. J. Gold supported on well-ordered ceria films: nucleation, growth and morphology in CO oxidation reaction. *Catalysis Letters* **2007**, *114*, 8-16.

(116) Szabova, L.; Camellone, M. F.; Huang, M.; Matolin, V.; Fabris, S. Thermodynamic, electronic and structural properties of Cu/CeO_2 surfaces and interfaces from first-principles DFT plus U calculations. *Journal of Chemical Physics* **2010**, *133*.

(117) Luches, P.; Pagliuca, F.; Valeri, S.; Illas, F.; Preda, G.; Pacchioni, G. Nature of Ag Islands and Nanoparticles on the CeO2(111) Surface. *Journal of Physical Chemistry C* **2012**, *116*, 1122-1132.

(118) Camellone, M. F.; Fabris, S. Reaction Mechanisms for the CO Oxidation on Au/CeO_2 Catalysts: Activity of Substitutional Au^{3+}/Au^+ Cations and Deactivation of Supported Au^+ Adatoms. *Journal of the American Chemical Society* **2009**, *131*, 10473-10483.

(119) Zhang, C.; Michaelides, A.; King, D. A.; Jenkins, S. J. Structure of gold atoms on stoichiometric and defective ceria surfaces. *Journal of Chemical Physics* **2008**, *129*.

(120) Chen, Y.; Hu, P.; Lee, M. H.; Wang, H. F. Au on (111) and (110) surfaces of CeO_2: A density-functional theory study. *Surface Science* **2008**, *602*, 1736-1741.

(121) Yang, Z.; Lu, Z.; Luo, G. First-principles study of the Pt/CeO_2(111) interface. *Physical Review B* **2007**, *76*, 075421.

(122) Yang, Z.; Lu, Z.; Luo, G.; Hermansson, K. Oxygen vacancy formation energy at the Pd/CeO_2(111) interface. *Physics Letters A* **2007**, *369*, 132-139.

(123) Kong, D.; Wang, G.; Pan, Y.; Hu, S.; Hou, J.; Pan, H.; Campbell, C. T.; Zhu, J. Growth, Structure, and Stability of Ag on CeO_2(111): Synchrotron Radiation Photoemission Studies. *Journal of Physical Chemistry C* **2011**, *115*, 6715-6725.

(124) Bevan, D. J. M.; Kordis, J. Mixed Oxides of the Type MO_2 (Fluorite)-M_2O_3 1. Oxygen Dissociation Pressures and Phase Relationships in the System CeO_2-Ce_2O_3 at High Temperatures. *Journal of Inorganic & Nuclear Chemistry* **1964**, *26*, 1509-1523.

(125) Freund, H. J. Clusters and islands on oxides: from catalysis via electronics and magnetism to optics. *Surface Science* **2002**, *500*, 271-299.

(126) Chen, M. S.; Goodman, D. W. The structure of catalytically active gold on titania. *Science* **2004**, *306*, 252-255.

(127) Herzing, A. A.; Kiely, C. J.; Carley, A. F.; Landon, P.; Hutchings, G. J. Identification of active gold nanoclusters on iron oxide supports for CO oxidation. *Science* **2008**, *321*, 1331-1335.

(128) Vajda, S.; Pellin, M. J.; Greeley, J. P.; Marshall, C. L.; Curtiss, L. A.; Ballentine, G. A.; Elam, J. W.; Catillon-Mucherie, S.; Redfern, P. C.; Mehmood, F.; Zapol, P. Subnanometre platinum clusters as highly active and selective catalysts for the oxidative dehydrogenation of propane. *Nature Materials* **2009**, *8*, 213-216.

(129) Lee, I.; Delbecq, F.; Morales, R.; Albiter, M. A.; Zaera, F. Tuning selectivity in catalysis by controlling particle shape. *Nature Materials* **2009**, *8*, 132-138.

(130) Behrens, M.; Studt, F.; Kasatkin, I.; Kuehl, S.; Haevecker, M.; Abild-Pedersen, F.; Zander, S.; Girgsdies, F.; Kurr, P.; Kniep, B.-L.; Tovar, M.; Fischer, R. W.; Norskov, J. K.; Schloegl, R. The Active Site of Methanol Synthesis over Cu/ZnO/Al_2O_3 Industrial Catalysts. *Science* **2012**, *336*, 893-897.

(131) Hansen, P. L.; Wagner, J. B.; Helveg, S.; Rostrup-Nielsen, J. R.; Clausen, B. S.; Topsoe, H. Atom-resolved imaging of dynamic shape changes in supported copper nanocrystals. *Science* **2002**, *295*, 2053-2055.

(132) Pacchioni, G. Electronic interactions and charge transfers of metal atoms and clusters on oxide surfaces. *Physical Chemistry Chemical Physics* **2013**, *15*, 1737-1757.

(133) Matthey, D.; Wang, J. G.; Wendt, S.; Matthiesen, J.; Schaub, R.; Laegsgaard, E.; Hammer, B.; Besenbacher, F. Enhanced bonding of gold nanoparticles on oxidized TiO_2(110). *Science* **2007**, *315*, 1692-1696.

(134) Campbell, C. T. The active site in nanopaticle gold catalysis. *Science* **2004**, *306*, 234-235.

(135) Campbell, C. T.; Peden, C. H. F. Chemistry - Oxygen vacancies and catalysis on ceria surfaces. *Science* **2005**, *309*, 713-714.

(136) Migani, A.; Vayssilov, G. N.; Bromley, S. T.; Illas, F.; Neyman, K. M. Greatly facilitated oxygen vacancy formation in ceria nanocrystallites. *Chemical Communications* **2010**, *46*, 5936-5938.

(137) Fabris, S.; Vicario, G.; Balducci, G.; de Gironcoli, S.; Baroni, S. Electronic and atomistic structures of clean and reduced ceria surfaces. *Journal of Physical Chemistry B* **2005**, *109*, 22860-22867.

(138) Castleton, C. W. M.; Kullgren, J.; Hermansson, K. Tuning LDA+U for electron localization and structure at oxygen vacancies in ceria. *Journal of Chemical Physics* **2007**, *127*, 244704.

(139) Andersson, D. A.; Simak, S. I.; Johansson, B.; Abrikosov, I. A.; Skorodumova, N. V. Modeling of CeO_2, Ce_2O_3, and CeO_{2-x} in the LDA plus U formalism. *Physical Review B* **2007**, *75*, 035109.

(140) Sellers, J. R. V.; James, T. E.; Hemmingson, S. L.; Farmer, J. A.; Campbell, C. T. Adsorption calorimetry during metal vapor deposition on single crystal surfaces: Increased flux, reduced optical radiation, and real-time flux and reflectivity measurements. *Review of Scientific Instruments* **2013**, *84*, 123901.

(141) Baron, M.; Bondarchuk, O.; Stacchiola, D.; Shaikhutdinov, S.; Freund, H. J. Interaction of Gold with Cerium Oxide Supports: CeO2(111) Thin Films vs CeOx Nanoparticles. *Journal of Physical Chemistry C* **2009**, *113*, 6042-6049.

(142) Barth, J. V.; Costantini, G.; Kern, K. Engineering atomic and molecular nanostructures at surfaces. *Nature* **2005**, *437*, 671-679.

(143) Vosko, S. H.; Wilk, L.; Nusair, M. Accurate Spin-Dependent Electron Liquid Correlation Energies for Local Spin-Density Calculations - A Critical Analysis. *Canadian Journal of Physics* **1980**, *58*, 1200-1211.

(144) Perdew, J. P.; Chevary, J. A.; Vosko, S. H.; Jackson, K. A.; Pederson, M. R.; Singh, D. J.; Fiolhais, C. Atoms, Molecules, Solids, and Surfaces - Applications of the Generalized Gradient Approximation fo Exchange and Correlation. *Physical Review B* **1992**, *46*, 6671-6687.

(145) Bell, A. T. The impact of nanoscience on heterogeneous catalysis. *Science* **2003**, *299*, 1688-1691.

(146) James, T. E.; Hemmingson, S. L.; Campbell, C. T. Energy of Supported Metal Catalysts: From Single Atoms to Large Metal Nanoparticles. *Acs Catalysis* **2015**, *5*, 5673-5678.

(147) Scire, S.; Minico, S.; Crisafulli, C.; Satriano, C.; Pistone, A. Catalytic combustion of volatile organic compounds on gold/cerium oxide catalysts. *Applied Catalysis B-Environmental* **2003**, *40*, 43-49.

(148) Rodriguez, J. A.; Ma, S.; Liu, P.; Hrbek, J.; Evans, J.; Perez, M. Activity of CeOx and TiOx nanoparticles grown on Au(111) in the water-gas shift reaction. *Science* **2007**, *318*, 1757-1760.

(149) Liu, Z. P.; Jenkins, S. J.; King, D. A. Origin and activity of oxidized gold in water-gas-shift catalysis. *Physical Review Letters* **2005**, *94*.

(150) Venezia, A. M.; Pantaleo, G.; Longo, A.; Di Carlo, G.; Casaletto, M. P.; Liotta, F. L.; Deganello, G. Relationship between structure and CO oxidation activity of ceria-supported gold catalysts. *Journal of Physical Chemistry B* **2005**, *109*, 2821-2827.

(151) Marta Branda, M.; Castellani, N. J.; Grau-Crespo, R.; de Leeuw, N. H.; Hernandez, N. C.; Sanz, J. F.; Neyman, K. M.; Illas, F. On the difficulties of present theoretical models to predict the oxidation state of atomic Au adsorbed on regular sites of CeO_2(111). *Journal of Chemical Physics* **2009**, *131*.

(152) Zhang, C.; Michaelides, A.; Jenkins, S. J. Theory of gold on ceria. *Physical Chemistry Chemical Physics* **2011**, *13*, 22-33.

(153) Akita, T.; Okumura, M.; Tanaka, K.; Kohyama, M.; Haruta, M. Analytical TEM observation of Au nano-particles on cerium oxide. *Catalysis Today* **2006**, *117*, 62-68.

(154) Zhang, C.; Michaelides, A.; King, D. A.; Jenkins, S. J. Anchoring Sites for Initial Au Nucleation on CeO_2(111): O Vacancy versus Ce Vacancy. *Journal of Physical Chemistry C* **2009**, *113*, 6411-6417.

(155) Hernandez, N. C.; Grau-Crespo, R.; de Leeuw, N. H.; Sanz, J. F. Electronic charge transfer between ceria surfaces and gold adatoms: a GGA plus U investigation. *Physical Chemistry Chemical Physics* **2009**, *11*, 5246-5252.

(156) Castellani, N. J.; Branda, M. A.; Neyman, K. M.; Illas, F. Density Functional Theory Study of the Adsorption of Au Atom on Cerium Oxide: Effect of Low-Coordinated Surface Sites. *Journal of Physical Chemistry C* **2009**, *113*, 4948-4954.

(157) Zhang, C.; Michaelides, A.; King, D. A.; Jenkins, S. J. Oxygen vacancy clusters on ceria: Decisive role of cerium f electrons. *Physical Review B* **2009**, *79*, 075433.

(158) Esch, F.; Fabris, S.; Zhou, L.; Montini, T.; Africh, C.; Fornasiero, P.; Comelli, G.; Rosei, R. Electron localization determines defect formation on ceria substrates. *Science* **2005**, *309*, 752-755.

(159) Akita, T.; Kohyama, M.; Haruta, M. Electron Microscopy Study of Gold Nanoparticles Deposited on Transition Metal Oxides. *Accounts of Chemical Research* **2013**, *46*, 1773-1782.

(160) Majimel, J.; Lamirand-Majimel, M.; Moog, I.; Feral-Martin, C.; Treguer-Delapierre, M. Size-Dependent Stability of Supported Gold Nanostructures onto Ceria: an HRTEM Study. *Journal of Physical Chemistry C* **2009**, *113*, 9275-9283.

(161) Tauster, S. J. Strong Metal-Support Interactions. *Accounts of Chemical Research* **1987**, *20*, 389-394.

(162) Bernal, S.; Calvino, J. J.; Cauqui, M. A.; Gatica, J. M.; Larese, C.; Omil, J. A. P.; Pintado, J. M. Some recent results on metal/support interaction effects in NM/CeO_2 (NM : noble metal) catalysts. *Catalysis Today* **1999**, *50*, 175-206.

(163) Alayoglu, S.; Nilekar, A. U.; Mavrikakis, M.; Eichhorn, B. Ru-Pt core-shell nanoparticles for preferential oxidation of carbon monoxide in hydrogen. *Nature Materials* **2008**, *7*, 333-338.

(164) Stamenkovic, V. R.; Fowler, B.; Mun, B. S.; Wang, G.; Ross, P. N.; Lucas, C. A.; Markovic, N. M. Improved oxygen reduction activity on $Pt_3Ni(111)$ via increased surface site availability. *Science* **2007**, *315*, 493-497.

(165) Yu, W.; Porosoff, M. D.; Chen, J. G. Review of Pt-Based Bimetallic Catalysis: From Model Surfaces to Supported Catalysts. *Chemical Reviews* **2012**, *112*, 5780-5817.

(166) Colen, R. E. R.; Kolodziejczyk, M.; Delmon, B.; Block, J. H. Kinetic study of CO oxidation on copper modified Pt(111). *Surface Science* **1998**, *412-13*, 447-457.

(167) Varela, A. S.; Schlaup, C.; Jovanov, Z. P.; Malacrida, P.; Horch, S.; Stephens, I. E. L.; Chorkendorff, I. CO_2 Electroreduction on Well-Defined Bimetallic Surfaces: Cu Over layers on Pt(111) and Pt(211). *Journal of Physical Chemistry C* **2013**, *117*, 20500-20508.

(168) Kuhn, W. K.; Campbell, R. A.; Goodman, D. W. Structural, Chemical, and Electronic Properties of Cu/Ta(110). *Journal of Physical Chemistry* **1993**, *97*, 446-453.

(169) Yates, J. T.; Peden, C. H. F.; Goodman, D. W. Copper Site Blocking of Hydrogen Chemisorption on Ruthenium. *Journal of Catalysis* **1985**, *94*, 576-580.

(170) Jiang, X. D.; Goodman, D. W. An AES, LEED, and CO Chemisorption Study of Copper Overlayers on Rh(100). *Surface Science* **1991**, *255*, 1-11.

(171) Rodriguez, J. A.; Campbell, R. A.; Goodman, D. W. Electron Donor Electron Acceptor Interactions in Surface Metal-Metal Bonds - the Cu/Re(0001) Systems. *Journal of Vacuum Science & Technology a-Vacuum Surfaces and Films* **1992**, *10*, 2540-2545.

(172) Yeates, R. C.; Somorjai, G. A. The growth and alloy formation of copper on the platinum(111) and stepped(553) crystal surfaces; characterization by LEED, AES, and CO thermal desorption. *Surface Science* **1983**, *134*, 729-744.

(173) Paffett, M. T.; Campbell, C. T.; Taylor, T. N.; Srinivasan, S. Cu adsorption on Pt(111) and its effects on chemisorption: a comparison with electrochemistry. *Surface Science* **1985**, *154*, 284-302.

(174) Holst, B.; Nohlen, M.; Wandelt, K.; Allison, W. The growth of ultra thin Cu-films on Pt(111), probed by helium atom scattering and scanning tunnelling microscopy. *Surface Science* **1997**, *377*, 891-894.

(175) Bales, G. S.; Zangwill, A. Morphological Instability of a Terrace Edge During Step Flow Growth. *Physical Review B* **1990**, *41*, 5500-5508.

(176) Cadle, S. H.; Bruckenstein.S. Inhibition of Hydrogen Adsorption by Submonolayer Deposition of Metals on Platinum. *Analytical Chemistry* **1971**, *43*, 1858-1862.

(177) Leung, L. W. H.; Gregg, T. W.; Goodman, D. W. Electrochemical and Ultrahigh Vacuum Characterization of Ultrathin Cu Films on Pt(111). *Langmuir* **1991**, *7*, 3205-3210.

(178) Pasti, I.; Mentus, S. First principles study of adsorption of metals on Pt(111) surface. *Journal of Alloys and Compounds* **2010**, *497*, 38-45.